

MICROCANONICAL INFLECTION-POINT ANALYSIS OF PHASES FOR SEMIFLEXIBLE POLYMERS

by

DILIMULATI AIERKEN

(Under the Direction of Michael Bachmann)

ABSTRACT

We study a generic model of semiflexible polymer with self-interactions, which exhibits a multitude of structural phases. Previous studies employing canonical statistical analysis methods for the identification and characterization of these phases have been inconclusive as these approaches lead to inconsistent results for systems of finite size. In contrast, the recently introduced microcanonical inflection-point analysis method not only enables the systematic identification and classification of transitions but is also able to distinguish close transitions that standard canonical analysis cannot resolve. Extensive one- and two-dimensional replica-exchange Monte Carlo simulations were employed to obtain accurate estimates of the Boltzmann entropies for the microcanonical inflection-point analysis. Our study reveals a mixed structural phase dominated by hairpin and loop conformations that originates from a bifurcation of the collapse transition line known from flexible polymers. Canonical quantities such as specific heat or fluctuations of square radius of gyration do not signal any transition into this intermediate phase embraced by the well-known random-coil and toroidal phases. In addition, the formation of distinct versatile ground-state conformations including compact globules, rod-like bundles and toroids are observed from replica-exchange simulations, and validated by global optimization methods. By utilizing contact and distance maps, we systematically investigate the effect of the bending stiffness on ground-state conformations.

INDEX WORDS: Semiflexible Polymers, Microcanonical Inflection-Point Analysis, Canonical Analysis, Phase Transitions, Bifurcation, Generalized Ensemble Monte Carlo, Bézier Smoothing

MICROCANONICAL INFLECTION-POINT ANALYSIS OF PHASES FOR SEMIFLEXIBLE POLYMERS

by

DILIMULATI AIERKEN

B.Sc., University of Science and Technology of China, China, 2018

A Dissertation Submitted to the Graduate Faculty of the
University of Georgia in Partial Fulfillment of the Requirements for the Degree.

DOCTOR OF PHILOSOPHY

ATHENS, GEORGIA

2023

©2023

Dilimulati Aierken

All Rights Reserved

MICROCANONICAL INFLECTION-POINT ANALYSIS OF PHASES FOR SEMIFLEXIBLE POLYMERS

by

DILIMULATI AIERKEN

Major Professor: Michael Bachmann

Committee: David P. Landau
Steven P. Lewis

Electronic Version hasn't been Approved:

Ron Walcott

Dean of the Graduate School

The University of Georgia

May 2023

ACKNOWLEDGMENTS

I would like first to express my heartfelt gratitude to my major advisor Dr. Michael Bachmann for sparing valuable time, patience, understanding, and imparting valuable knowledge and guidance throughout the years. I enjoyed all those numerous scientific discussions, which helped my academic and personal development. I would not be where I am without his mentorship.

I am grateful for the support, constructive feedback, and insightful inputs provided by my advisory committee members, Dr. David P. Landau and Dr. Steven P. Lewis. I have learned a lot about simulation studies from Dr. Landau's courses and benefited a lot from conversations with Dr. Lewis.

I also want to thank Dr. Shengming Zhang, Dr. Yifan Dai, and Dr. Kedkanok Sitarachu for helping me with valuable suggestions and discussions. Besides, I would like to thank our CSP graduate student members, especially Garrett Floyd, Steven Hancock, Zewen Zhang, Dr. Jiahao Xu, Dr. Matthew Wilson, Dr. Alfred Farris, Dr. Nima Karimitari, and Dr. Kai Qi. In addition, I would like to thank Dr. Kanzo Nakayama, Dr. Phillip Stancil, Dr. Daphne Norton, Dr. Shan-Ho Tsai, Dr. Zhuofei Hou, Mike Caplinger, Jeff Deroshia, and Robin Taylor for their professional and technical support in my graduate study.

I would like to extend gratitude to all my greatly supportive friends, who made this journey more enjoyable. Thank you from the bottom of my heart.

Finally, I am extremely grateful for my family's love and encouragement. The unwavering support and belief in me from my parents and my sister have been a constant source of motivation. Moreover, I would like to explicitly thank my aunt, Dr. Rukiya Matsidik, for her support.

CONTENTS

Acknowledgments	iv
List of Figures	vi
List of Tables	xviii
1 Introduction	1
2 Statistical Analysis of Phase Transitions	5
2.1 Phase Transitions in Thermodynamics	5
2.2 Conventional Study of Phase Transitions in Finite Systems	16
2.3 Generalized Microcanonical Inflection-Point Analysis	21
3 Model and Methods	27
3.1 Model	27
3.2 Monte Carlo Simulations	34
3.3 Multiple-histogram Reweighting and Smoothing	58
4 Simulation and Analysis of a Polymer System	65
4.1 Parallel Tempering Temperature Set	65
4.2 Combination of Advanced Updates	70
4.3 Canonical Analysis	74

4.4	Microcanonical Inflection-Point Analysis	77
5	Analysis of Semiflexible Polymers	84
5.1	Collapse Transition in Semiflexible Polymers	84
5.2	Analysis of Putative Ground-State Conformations	109
6	summary	125
	Bibliography	129

LIST OF FIGURES

2.1	A schematic representation of entropy S and heat capacity C_V functions of temperature T for first-order (a, b) and second-order phase transitions (c, d).	8
2.2	(a) Normalized canonical energy distribution function at the first-order transition temperature, and (b) specific heat as a function of temperature for a 40×40 , $q = 7$ Potts model. (c) Normalized canonical energy distribution function at the first-order freezing transition temperature, and (d) specific heat as a function of temperature for a flexible polymer model with 55 monomers. Results are obtained from Monte Carlo simulations.	17
2.3	(a) Specific heat C_V/N (normalized heat capacity) along with typical spin configurations at different temperatures, (b) normalized magnetic susceptibility χ/N , and (c) normalized magnetization M/N for various sizes of 2D Ising models without external field, obtained from Monte Carlo simulations. The dotted line indicates the peak location of the heat capacity and the dashed line indicates the peak location of the susceptibility for the system size of 60×60	18
2.4	(a) Specific heat C_V along with typical polymer conformations from two phases, (b) fluctuations of square radius of gyration $d\langle R_{\text{gyr}}^2 \rangle/dT$, and (c) squared radius of gyration $\langle R_{\text{gyr}}^2 \rangle$ as an order parameter for a 55-mer flexible polymer model, obtained from Monte Carlo Simulations. The dotted line indicates the shoulder location in the heat capacity C_V , and the dashed line indicates the peak location in the fluctuations of the square radius of gyration $d\langle R_{\text{gyr}}^2 \rangle/dT$	19

2.5	(a) Specific heat $C_V/N = (1/N)d\langle E \rangle/dT$ as a function of temperature T , and normalized energy variance $s^2(E) = (-1/N)d\langle E \rangle/d\beta$ as a function of inverse temperature β for 1D-Ising model with periodic boundary conditions in the thermodynamic limit.	20
2.6	Typical monotonic behavior of microcanonical entropy (a) $S(E)$ and first- to fourth-order derivatives (b) $\beta = dS/dE$; (c) $\gamma = d^2S/dE^2$; (d) $\delta = d^3S/dE^3$; (e) $\epsilon = d^4S/dE^4$, if no transition occurs.	21
2.7	Typical sketch plot of (a) energy E versus temperature T around transition point for finite systems, and (b) temperature T versus energy E . Transition points are indicated by dotted lines.	22
2.8	Sketch of <i>independent transitions</i> up to fourth order as defined in the microcanonical inflection point analysis method. (a) A first-order independent transition is defined by the inflection point in $S(E)$ and identified from the backbending of $\beta = dS/dE$ that possesses a positive minimum. (b) A second-order independent transition is defined by the inflection point in $\beta = dS/dE$ and identified from the backbending of $\gamma = d^2S/dE^2$ with a negative maximum. (c) A third-order independent transition is defined by the inflection point in $\gamma = d^2S/dE^2$ and identified from the backbending of $\delta = d^3S/dE^3$ that possesses a positive minimum. (d) A fourth-order independent transition is defined by the inflection point in $\delta = d^3S/dE^3$ and identified from the backbending of $\epsilon = d^4S/dE^4$ with a negative maximum.	24

2.9	Sketch of <i>dependent transitions</i> up to fourth order as defined in the microcanonical inflection point analysis method. The inflection points are located in the entropy derivatives' backbending region that are resulted by lower order independent transitions. (a) A dependent second-order transition is defined by the inflection point within backbending region of $\beta = dS/dE$ and identified from a positive minimum in $\gamma = d^2S/dE^2$. (b) A dependent third-order transition is defined by the inflection point within backbending region of $\gamma = d^2S/dE^2$ and identified from a negative maximum in $\delta = d^3S/dE^3$. (c) A dependent fourth-order transition is defined by the inflection point within backbending region of $\delta = d^3S/dE^3$ and identified from a positive minimum in $\epsilon = d^4S/dE^4$	26
3.1	A coarse-graining procedure of a protein. Each monomer i represents an amino acid with side groups R_i that are connected by peptide bonds, which are shown as orange dotted rectangles. Some key atoms in the polypeptide chain are also labeled.	28
3.2	(a) Sketch (transparent gray) of two common secondary structures, α -helix and β -sheet, abstracted from the local spatial conformation of the polypeptide backbones. Carbon atoms are colored gray, nitrogen atoms are colored blue, and oxygen atoms are colored red. Side chains are not shown for clarity. (b) Structure of bovine mitochondrial F1-ATPase, PDB ID: 1BFM (http://doi.org/10.2210/pdb1BMF/pdb), using secondary structure representation. α -helix parts are colored in red and β -sheet parts are colored in blue.	29
3.3	Schematic representation of interactions for a chain of $N = 55$ monomers. The bonded potential (green) V_B is highlighted for a pair of bonded monomers, the non-bonded potential (blue) V_{NB} for a pair of non-bonded monomers, and bending penalty V_{bend} (red) for two consecutive bonds that are characterized by bending angle θ	31

3.4	(a) Plot of the Lennard-Jones potential $V_{\text{LJ}}(r)/\epsilon_{\text{LJ}}$ versus monomer distance r/r_0 . Van der Waals distance σ and cutoff r_c are also labeled. (b) FENE potential $V_{\text{FENE}}(r)/\epsilon_{\text{LJ}}$ (solid) and harmonic potential (dashed) with the same elasticity as the FENE potential plotted as functions of bond length r/r_0	32
3.5	Plot of normalized bending potential $V_{\text{bend}}(\theta - \theta_0)/\kappa$ versus deviated bond angle $\theta - \theta_0$. The schematic representation of bond angles formed by two consecutive bonds is shown in the right figure. θ is actual bond angle and θ_0 is the actual reference angle.	33
3.6	Illustration of the displacement update used in the polymer simulations. A randomly chosen monomer (blue) is moved to the new location (red) by a random vector $\Delta \mathbf{r} = (\Delta x, \Delta y, \Delta z)$. The available space for the monomer to update its position is shown as the cube that is centered around the originally chosen monomer (blue) with edge length d	37
3.7	Illustration of the crankshaft update used in simulations. A randomly chosen monomer (red) is rotated by a random angle. The rotation axis formed by the two monomers bonded to the chosen monomer is shown as a red line.	39
3.8	Illustration of the pivot update used in simulations. Randomly chosen monomer (red), and a random rotation axis generated. Then the rest of the chain (blue) is rotated by a random angle.	40
3.9	Illustration of the bond-exchange update based on indices. The monomer indexes are labeled and satisfy $j > i + 1$. (Upper part) Incorrect way of creating new two bonds, $(i + 1 \rightarrow j)$ and $(i \rightarrow j + 1)$, which breaks the chain into two parts. The broken bonds are marked by dashed lines. (Bottom part) The correct way of creating new two bonds, $(i \rightarrow j)$ and $(i + 1 \rightarrow j + 1)$	41

3.10	An example of the bond-exchange update used in simulations. From upper conformation to lower conformation, two nearby bonds (red) are chosen, and they are broken. Then two new bonds (blue) are formed without creating a discontinued loop, which is illustrated in Fig.3.9.	43
3.11	Sketch of the end-bond-exchange update based on monomer indices. The monomer indexes are labeled and satisfy $j > i + 1$. If the other end's monomer is chosen, reversing the full indices will recover this order due to symmetry. (Upper part) The correct way of creating a new bond between the end monomer (red) and a chosen nearby monomer (blue), where the bond between the blue monomer j and $j - 1$ are broken (red cross). (Bottom part) Breaking the bond ($j \rightarrow j + 1$) creates a closed loop and thus breaks the continuity of the chain.	44
3.12	An example of the bond-exchange update used in simulations. From upper conformation to lower conformation, an end monomer is randomly chosen (blue), and then a nearby monomer (red) is selected. A bond between these two monomers is created, and the bond between the selected monomer (red) and the neighboring monomer (green) is broken. Consequently, the neighboring monomer (green) becomes the new end monomer. It can also be seen from these conformations that the end monomer (blue) of the upper conformation has only one possible monomer (red) to connect. However, for the lower conformation, the end monomer (green) has more than one available monomer to connect.	45
3.13	Schematic representation of parallel tempering swaps between adjacent replicas for an example with 6 different inverse temperatures β . In between the swaps, Metropolis Monte Carlo sweeps are performed. The swaps are proposed between either higher temperature threads or lower temperature threads periodically	50

3.14	Energy histograms of the same system with different temperature sets. The first-order transition region is colored as gray. (a) Geometric setup of temperatures with $R = 1.1$. (b) Geometric setup of temperatures with $R = 1.3$. There is almost no overlap of histograms in the transition region. (c) Energy histogram if temperature sets are further adjusted.	52
3.15	Illustration of an extended replica exchange Monte Carlo simulation in a combined parameter space of inverse temperature β and bending stiffness κ with the size of 6×6 . Each node (i, j) represents a simulation thread with a parameter combination of (β_i, κ_j) . In total, 4 different types of exchange directions are colored differently. The exchange directions are determined randomly with equal probabilities. The overlapping of exchange directions for corner nodes is conservation of flows. . . .	55
3.16	A fourth-order Bézier curve $\mathbf{B}(t)$ constructed with five control points $\mathbf{P}_0, \mathbf{P}_1, \dots, \mathbf{P}_4$ at $t = 0.25$. Intermediate points are defined as $\mathbf{Q}_i(t) = \mathbf{P}_i + t(\mathbf{P}_{i+1} - \mathbf{P}_i)$, $\mathbf{R}_i(t) = \mathbf{Q}_i + t(\mathbf{Q}_{i+1} - \mathbf{Q}_i)$, and $\mathbf{S}_i(t) = \mathbf{R}_i + t(\mathbf{R}_{i+1} - \mathbf{R}_i)$. Finally, the curve is constructed from $\mathbf{B}_i(t) = \mathbf{S}_i + t(\mathbf{S}_{i+1} - \mathbf{S}_i)$	60
3.17	Comparison of two different smoothing methods on a noisy data set of a function. (a) The original function (solid redline) and noisy data points are generated by adding random noise to the original function. The blue dashed line is the smoothed line of the data points by our Bézier method. The green dotted line is the results of the Savitzky-Golay method [124], where the window size is set to 51 data points and the order of the polynomial is set to 3. (b) The first-order derivatives of the original function and the estimated first-order derivatives from the two smoothing methods.	64

4.1	(a) Average energy $\langle E \rangle$ obtained from a parallel tempering Monte Carlo simulation with a geometric temperature setup for a flexible polymer with $N = 55$ monomers. Data points from even and odd temperature threads are colored differently. (b) Actual exchange acceptance rate \mathcal{R} between neighboring temperature threads from the same simulation. Both quantities are plotted as functions of the inverse heat bath temperature β_{can} . Structural phase transition points are indicated by dashed lines and corresponding dominant structures in each phase are shown.	67
4.2	(a) Iteration process of adjusting temperatures for parallel tempering using the expected exchange rate given in Eq. (4.2) and (b) corresponding estimated exchange rates for each iteration for a flexible polymer with $N = 55$ monomers. The total number of simulation threads is 48, and the threads colored from deep green to yellow-green color in increasing order.	68
4.3	Comparison of the actual exchange rate for parallel tempering with the same number of simulation threads for a flexible polymer with $N = 55$ monomers. The known transition points are indicated by the dotted lines, and typical structures of the corresponding phases are shown.	70
4.4	Tracking of two replicas in a parallel tempering simulation with 48 temperature threads within 10^8 Monte Carlo sweeps for a flexible polymer with $N = 55$ monomers.	71
4.5	Actual adjustment of the displacement box edge length d_i in the temperature thread i for a flexible polymer with $N = 55$ monomers. The initial values are all set to $d_i = 0.5r_0$. The length is adjusted every 100 Monte Carlo sweeps (MCS). Larger index i indicates larger β_i^{can} (lower temperatures).	72

4.6	Actual acceptance rate of different updates in the simulation thread for a flexible polymer with $N = 55$ monomers. The brown is the acceptance rate of the displacement updates from a different simulation with the same temperature setups, where the box edge length is set to $d_i = 0.3r_0$ in all simulation threads i . The known transition points are indicated by the dotted lines, and typical structures of the corresponding phases are shown.	73
4.7	(a) Measured thermal fluctuations of the system energy, $C_V = d\langle E \rangle / dT_{\text{can}}$, (b) system energy variance $\text{var}(E)$, and (c) the thermal fluctuations of the square radius of gyration $\Gamma_g = d\langle R_{\text{gyr}}^2 \rangle / dT_{\text{can}}$ as a function of the inverse heat bath temperature $\beta_{\text{can}} = 1/T_{\text{can}}$ for a flexible polymer with $N = 55$ monomers. The known transition points are indicated by the dotted lines, and typical structures of the corresponding phases are shown. Error bars are about the size of data points. .	76
4.8	Interaction of logarithmic partition functions $\ln Z(\beta_i^{\text{can}})$ in the multi-histogram reweighting process for a flexible polymer model with 55 monomers. Larger index i indicates larger β_i^{can} (lower temperatures).	78
4.9	Comparison of recalculated values from reweighting (red lines) for (a) average energy, (b) heat capacity, and (c) energy variance between measured values from the parallel tempering simulations overflow a flexible polymer model with 55 monomers. Error bars are about the size of data points.	79
4.10	(a) Microcanonical entropy $S(E)$ and its derivatives (b) $\beta(E) = dS/dE$, and (c) $\gamma(E) = d\beta/dE$ as functions of the energy for a flexible model with 55 monomers. In this figure, we focus on the high-energy (or high-temperature) regime. Least-sensitive inflection points are marked by a dot, and the corresponding transition energy is indicated by a dashed line.	81

4.11	(a) Microcanonical entropy $S(E)$ and its derivatives (b) $\beta(E) = dS/dE$, (c) $\gamma(E) = d\beta/dE$, and (inset) $\delta(E) = d\gamma/dE$ as functions of the energy for a flexible model with 55 monomers. In this figure, we focus on the low-energy (or low-temperature) regime. Least-sensitive inflection points are marked by dots, and the corresponding transition energies are indicated by dashed lines.	82
5.1	Iteration process of adjusting temperatures in parallel tempering using expected exchange rates for a semiflexible polymer with $N = 55$ monomers with bending stiffness (a) $\kappa = 5$, and (b) $\kappa = 14$. The total number of simulation threads is 60, and the index of the i th thread's heat-bath temperature is indicated by the color bar.	86
5.2	Running average of the energy when simulated with (a) parallel tempering, and with (b) extended (EX) replica-exchange method for a semiflexible polymer with bending stiffness $\kappa = 10$ at temperature T_{can} . The bin widths for the average calculation are 10^6 Monte Carlo Sweeps (MCS) for the PT and 2.5×10^6 for the extended replica exchange simulation.	87
5.3	Measured exchange rates \mathcal{R} of extended replica-exchange simulations in the combined space of the inverse temperature and bending stiffness for $\kappa = 3$, $\kappa = 4$, $\kappa = 5$ and $\kappa = 6$ at relatively high temperatures. The square points mark the simulation threads in the parameter space. The shades of lines between neighboring threads corresponds to the exchange rate.	89
5.4	Measured acceptance rates of different updates in the extended replica-exchange Monte Carlo simulations for a semiflexible polymer model with 55 monomers with various bending stiffness κ	91
5.5	Thermal fluctuations of (a) energy (heat capacity $C_V = d\langle E \rangle / dT_{\text{can}}$), (b) energy variance $\text{Var}(E) = -d\langle E \rangle / d\beta_{\text{can}}$ and (b) thermal fluctuations of the square radius of gyration ($\Gamma_g = d\langle R_{\text{gyr}}^2 \rangle / dT_{\text{can}}$) for the semiflexible 55mer, plotted as functions of β_{can} for $\kappa = 3$, $\kappa = 4$, $\kappa = 5$ and $\kappa = 6$	92

5.6	(a) Microcanonical entropy S and its derivatives (b) $\beta = dS/dE$, (c) $\gamma = d\beta/dE$, (d) $\delta = d\gamma/dE$ plotted as functions of the energy difference from the κ -dependent global energy minimum estimate for the semiflexible polymer with $\kappa \in [0, 6]$. Least-sensitive inflections in β are marked by a dot.	94
5.7	Measured exchange rates of separate extended replica-exchange simulations in the combined space of the inverse temperature and bending stiffness at relatively high temperatures for (a) for $\kappa = 7, 8, 9, 10$ and (b) for $\kappa = 11, 12, 13, 14$. Square symbols mark the location of simulation threads in the parameter space. The line colors represent exchange rates between neighboring threads. (c) Measured exchange acceptance rates at relatively high temperatures for $\kappa = 7.5, 8.5, 15, 16$	96
5.8	Thermal fluctuations of (a), (d) energy (heat capacity $C_V = d\langle E \rangle / dT_{\text{can}}$), (b), (e) energy variance $\text{Var}(E) = -d\langle E \rangle / d\beta_{\text{can}}$ and (c), (d) square radius of gyration ($\Gamma_g = d\langle R_{\text{gyr}}^2 \rangle / dT_{\text{can}}$), plotted as functions of β_{can} at selected values of the bending stiffness, $7 \leq \kappa \leq 16$	98
5.9	(a) Microcanonical entropy S and its derivatives (b) $\beta = dS/dE$, (c) $\gamma = d\beta/dE$ for the different models with $\kappa = 7.0, \dots, 10.0$ plotted as functions of the $\Delta E^{(\kappa)}$. Least-sensitive inflection points are marked by dots and transition energies are indicated by dotted lines.	100
5.10	(a) Microcanonical entropy S and its derivatives (b) $\beta = dS/dE$ for the different models with $\kappa = 11, \dots, 16$ plotted as functions of $\Delta E^{(\kappa)}$. Least-sensitive inflection points are marked by a dot and transition energies are indicated by dotted lines.	103

5.11	Hyperphase diagram for semiflexible polymers with 55 monomers, parametrized by bending stiffness κ and inverse microcanonical temperature β . Red diamonds mark first-order, blue dots second-order, and purple triangles third-order transitions. Solid transition lines are guides to the eye. Representative structures, characterizing the dominant types in the respective phases (C : wormlike random coils, H : hairpins, L : loops, T : toroids), and their distance maps (lower triangles in the insets) are also shown. Monomer labels are ordered from the black (first monomer) to the white end (last monomer).	105
5.12	(a) Microcanonical temperature. (b) System energy dependence of frequencies for the different structure types at $\kappa = 16$. (c) Canonical energy probability distributions P_{can} at various inverse thermal energies $\beta_{\text{can}} = 1/k_{\text{B}}T_{\text{can}}$	107
5.13	Comparison between canonical and microcanonical quantities for $N = 55, \kappa = 16$. The shaded area is the standard deviation of the system energy $\sigma(E)$, which represents the thermal fluctuations of the system energy E at the corresponding heat-bath temperature β_{can}	108
5.14	Same as Fig. 5.12, but for $N = 70$ and $N = 100$	110
5.15	Exemplified global optimization simulations of selected κ values for a generic semiflexible polymer model.	112
5.16	(a) Total energy E and Lennard-Jones contribution E_{LJ} of ground-state conformations. (b) Total bending energy E_{bend} and renormalized bending contributions $\epsilon_{\text{bend}} = E_{\text{bend}}/\kappa$ for the entire array of κ parameter values simulated.	114
5.17	(a) Square principal moments $\lambda_x^2, \lambda_y^2, \lambda_z^2$ from the diagonalized gyration tensor S , (b) square radius of gyration R_{gyr}^2 , (c) and relative shape anisotropy A for ground-state conformations on a large array of κ values.	116
5.18	Pair distribution functions of the lowest-energy states for $\kappa = 0, 1, 2, 3$	118

5.19	Representations of ground-state conformations (left panel) and their contact maps (right) for $\kappa \leq 5$. The upper triangle contains the monomer distance map, where the distance $r_{i,j}$ of monomers i and j is colored. The contact map is shown in the lower triangle. Monomers i and j are in contact if $r_{i,j} < 1.2$	120
5.20	Same as Fig. 5.19, but for $6 \leq \kappa \leq 11$	122
5.21	Same as Fig. 5.19, but for $\kappa \geq 11$	124

LIST OF TABLES

4.1	A parallel tempering temperature set obtained from the energy method iterations illustrated in Fig. 4.2 for a 55-mer flexible polymer model i is the index of the simulation thread.	69
5.1	Second-order transitions found from microcanonical analysis for the flexible ($\kappa = 0$) and semiflexible ($\kappa \in [1, 6]$) polymers. Transition energy E_{tr} , distance from putative ground-state energy $\Delta E^{(\kappa)}$, inverse microcanonical transition temperature β_{tr} are listed.	95
5.2	Lowest-energy conformations and corresponding energy values obtained from simulations for the selected values of the bending stiffness ranging from $\kappa = 0$ (fully flexible) to $\kappa = 19$	113

CHAPTER 1

INTRODUCTION

Statistical analysis methods have long been used for the identification, characterization, and classification of phase transitions in complex systems. Advanced computer simulation techniques, mostly based on Markov chain Monte Carlo algorithms, helped advance the field beyond the deadlocks mathematical approaches had run into. Nonetheless, the general idea remained the same. Phase transitions were generally only considered in the thermodynamic limit, which was historically introduced to make studies of macroscopic systems mathematically tractable. Therefore, phase transitions have been identified and classified by means of discontinuities or divergences in thermodynamic state variables or response functions [1]. In computational statistical physics, finite-size scaling analysis [2–8] provided the tool for extrapolating the results obtained in simulations of systems of finite size toward this hypothetical limit. These methods proved to be extremely successful, and for decades the scientific community did not see any reason to change paradigms and consider a more general perspective despite the fact that all systems in nature are finite and systems on nanoscales moved into the focus of substantial interest in microbiology and technology. Ignoring surface effects was also convenient.

However, systems of finite size do not exhibit such obvious signals, as these only occur in the thermodynamic limit. Consequently, conventional canonical statistical analysis of phase transitions rests on the search for catastrophic behavior of thermodynamic state variables and response

functions in thermodynamic parameter spaces. Hence, significant effort has been dedicated to the evaluation of critical exponents in continuous phase transitions and the grouping of systems in universality classes.

In recent years, however, the growing interest in systems on microscopic and mesoscopic scales, which do not satisfy the criteria for the thermodynamic limit, has shifted the perspective. Alternative approaches that enable studies of phase transitions in systems of any size have turned out to be promising. Modern interdisciplinary research of systems on nanometer scales cannot ignore the fact that the surface of the system is at least as important for the structural behavior of the system as the bulk effects. For example, the functionality of biomacromolecules like proteins depends on the folding process into stable geometric conformations. These processes, which occur in a thermal environment, resemble transitions between disordered and ordered phases known from macroscopic systems. In fact, for very long polymers, these structure formation processes *are* phase transitions, even in the strict conventional sense. However, many types of heterogeneous polymers like proteins cannot be scaled up, but still show clear transition features. This makes the extension of the established theory of phase transitions a necessity.

Moreover, canonical statistical methods create ambiguities, which render the unique characterization of phase transitions problematic. A prominent example is the peak in the specific heat curve of the one-dimensional Ising model [9]. As it is also finite in the thermodynamic limit, one does not associate a phase transition with it. But how to interpret a peak in response quantities, if the thermodynamic limit for this system does not exist? In recent years, it has nonetheless become common to consider peaks or “shoulders” transition signals in curves of response quantities for finite systems, along with huge effort to find appropriate order parameters, which are mostly system-specific and hardly generalizable. In addition, temperatures suggested by transition signals in different response quantities are usually not identical for the same transition, making it hard to uniquely locate the transition points. This appears to be an inconsistent approach and renders, in fact, the choice of the temperature as the basic thermodynamic state variable questionable.

Combining results of previous studies of the microcanonical Boltzmann entropy [10] and the principle of minimal sensitivity [11, 12], a systematic approach to phase transitions in systems of any size has been introduced recently by identifying the least-sensitive inflection points in the entropy and its derivatives [13]. This analysis method even allows for the classification of phase transitions in analogy to Ehrenfest’s classification scheme in thermodynamics, which is based on derivatives of thermodynamic potentials [1].

Many variants of RNA, DNA, even proteins can be considered semiflexible polymers, where bending stiffness, as a type of energetic penalty, competes with attractive van der Waals forces in structure formation processes. Therefore, semiflexible polymer models play an important role as they allow for studies of these various classes of biopolymers. One particularly intriguing problem is the characterization of phases for entire classes of semiflexible polymers. This has been a long-standing problem. Simple early approaches such as the well-known wormlike-chain or Kratky-Porod model [14] has frequently been used to describe aspects of basic structural and dynamic properties of semiflexible polymers. However, the lack of self-interactions in this model prevents structural transitions. Significant advances in the development of Monte Carlo algorithms and vastly improved technologies enabled the computer simulation of more complex coarse-grained models in recent years [15–21], Focusing on few main features, while other less relevant degrees of freedom are considered averaged out, provides a more general view of generic structure properties. Yet, most of these studies still employed conventional canonical statistical analysis techniques that are often not sufficiently sensitive enough to allow for the systematic construction of phase diagram for finite systems. Besides, these relative biomolecules form distinct structures that allow them to perform specific functions in the physiological environment and understanding the effects of the bending stiffness on ground-state conformations is also crucial in many fields.

In this study, we perform Monte Carlo computer simulation studies of a generic coarse-grained model for semiflexible polymers to analyze the structural transitions by means of the generalized microcanonical least-sensitive inflection point method. This model possesses multiple transition

barriers. Therefore, we employ advanced generalized ensemble Monte Carlo algorithms, most notably an extended version of the replica-exchange (parallel tempering) method in the combined space of simulation temperature and bending stiffness. Advanced sets of conformational updates were employed to sample the phase space. The multihistogram reweighting procedure was used to obtain high-accuracy estimates of the microcanonical entropy and its derivatives required for this study. This allows us to thoroughly investigate the changes in phase behavior at the most interesting part of the hyperphase diagram of this generic model for semiflexible polymers in the space of bending stiffness and temperature, where the structurally most relevant toroidal, loop, and hairpin phases separate from the wormlike chain regime of random coils. As we will show, microcanonical inflection-point analysis reveals two transitions that standard canonical analysis cannot resolve. Moreover, the formation of distinct versatile ground-state conformations including compact globules, rod-like bundles and toroids strongly depends on the strength of the bending restraint. Therefore we also performed a detailed analysis of contact and distance maps on the lowest-energy states obtained from the two-dimensional replica-exchange simulations. In addition, global optimization methods such as Wang-Landau, simulated annealing and Energy Landscape Paving were also used to verify and consolidate our putative ground states obtained from the replica exchange simulations.

The dissertation is organized as follows. In Chapter 2, we introduce the theory of phase transitions in thermodynamics and statistical ensembles, the conventional study of phase transitions in finite systems, and the novel generalized microcanonical inflection-point analysis method. The coast-grained model as well as the Monte Carlo methods are described in Chapter 3. The advanced Monte Carlo techniques and canonical and microcanonical analysis methods are demonstrated in Chapter 4 by a well-studied generic coarse-grained flexible polymer model. This is followed by a full analysis of semiflexible polymers in Chapter 5. Finally, the dissertation is concluded by a summary in Chapter 6.

CHAPTER 2

STATISTICAL ANALYSIS OF PHASE TRANSITIONS

2.1 Phase Transitions in Thermodynamics

A phase of matter in thermodynamics is represented by a set of macrostates that share the same or similar macroscopic physical properties within a range of external conditions. However, a phase transition into another happens at a transition point, where an abrupt change in the macroscopic properties occurs upon a small variation of external parameters.

Conventionally, phase transitions are grouped into either discontinuous (first-order) or continuous (second-order) transitions. More specifically, Ehrenfest's classification scheme [1] is widely used to identify and classify the phase transitions. This method is mainly based on the idea that discontinuities or divergences occur in thermodynamic potentials or response quantities. Moreover, the order of the transition is defined as the lowest derivative of the thermodynamic potential showing a discontinuity upon a change of one of the thermodynamic state variables at the transition point. For studies of phase transitions, the most commonly used thermodynamic potential is the Helmholtz free energy

$$F(T, V, N) = U(S, V, N) - TS, \quad dF = -SdT - PdV + \mu dN, \quad (2.1)$$

which is obtained by making use of Legendre transformation from the internal energy $U(S, V, N)$,

$$dU(S, V, N) = TdS - pdV + \mu dN. \quad (2.2)$$

For the free energy $F(T, V, N)$, temperature T , volume V , and number of particles N are natural variables that can be relatively easily controlled experimentally, in contrast to the internal energy $U(S, V, N)$, which includes the entropy S as a natural variable. According to Ehrenfest's classification scheme, explicitly for the free energy $F(T, V, N)$ at the transition point, a phase transition between phases a and b is of order n if

$$\left(\frac{\partial^m F_a}{\partial T^m} \right)_{V,N} = \left(\frac{\partial^m F_b}{\partial T^m} \right)_{V,N}, \quad (2.3a)$$

$$\left(\frac{\partial^m F_a}{\partial V^m} \right)_{T,N} = \left(\frac{\partial^m F_b}{\partial V^m} \right)_{T,N}, \quad (2.3b)$$

$$\left(\frac{\partial^m F_a}{\partial N^m} \right)_{T,V} = \left(\frac{\partial^m F_b}{\partial N^m} \right)_{T,V}, \quad (2.3c)$$

for $m = 1, 2, 3, \dots, n-1$ and

$$\left(\frac{\partial^n F_a}{\partial T^n} \right)_{V,N} \neq \left(\frac{\partial^n F_b}{\partial T^n} \right)_{V,N}, \quad (2.4a)$$

or

$$\left(\frac{\partial^n F_a}{\partial V^n} \right)_{T,N} \neq \left(\frac{\partial^n F_b}{\partial V^n} \right)_{T,N}, \quad (2.4b)$$

or

$$\left(\frac{\partial^n F_a}{\partial N^n} \right)_{T,V} \neq \left(\frac{\partial^n F_b}{\partial N^n} \right)_{T,V}. \quad (2.4c)$$

Typically, a first-order transition is characterized by a discontinuity in the first-order derivative of the free energy $F(T, V, N)$ with respect to temperature T , i.e., the entropy

$$S(T, V, N) = - \left(\frac{\partial F}{\partial T} \right)_{V, N}. \quad (2.5)$$

Thus, for a first-order transition between phase a and b at the transition temperature T_{tr} with fixed V and N ,

$$F_a(T_{\text{tr}}, V, N) = F_b(T_{\text{tr}}, V, N), \quad S_a(T_{\text{tr}}, V, N) \neq S_b(T_{\text{tr}}, V, N). \quad (2.6)$$

The discontinuity of S as a function of temperature T is shown schematically in Fig 2.1 (a). As a result, there is a coexistence of two phases, represented by S_a and S_b , as well as energy exchange between the system and the environment at this constant transition temperature T_{tr} ,

$$Q_{\text{lat}} = T_{\text{tr}} |S_a - S_b| = T_{\text{tr}} |\Delta S|, \quad (2.7)$$

which is called latent heat. One of the most prominent examples of a first-order transition is the freezing of water. Under normal conditions, liquid water coexists with solid water, i.e., ice, at $273.15K$ and $101.325kPa$.

Similarly, a second-order phase transition is usually represented by continuous entropy $S(T, V, N)$ and a discontinuity in one of the second-order derivatives of $F(T, V, N)$. A prominent example is the discontinuity of the heat capacity

$$C_V = T \left(\frac{\partial S}{\partial T} \right)_{N, V} = -T \left(\frac{\partial^2 F}{\partial T^2} \right)_{N, V} \quad (2.8)$$

at the transition temperature T_c (also known as critical temperature),

$$S_a(T_c, V, N) = S_b(T_c, V, N), \quad C_a(T_c, V, N) \neq C_b(T_c, V, N), \quad (2.9)$$

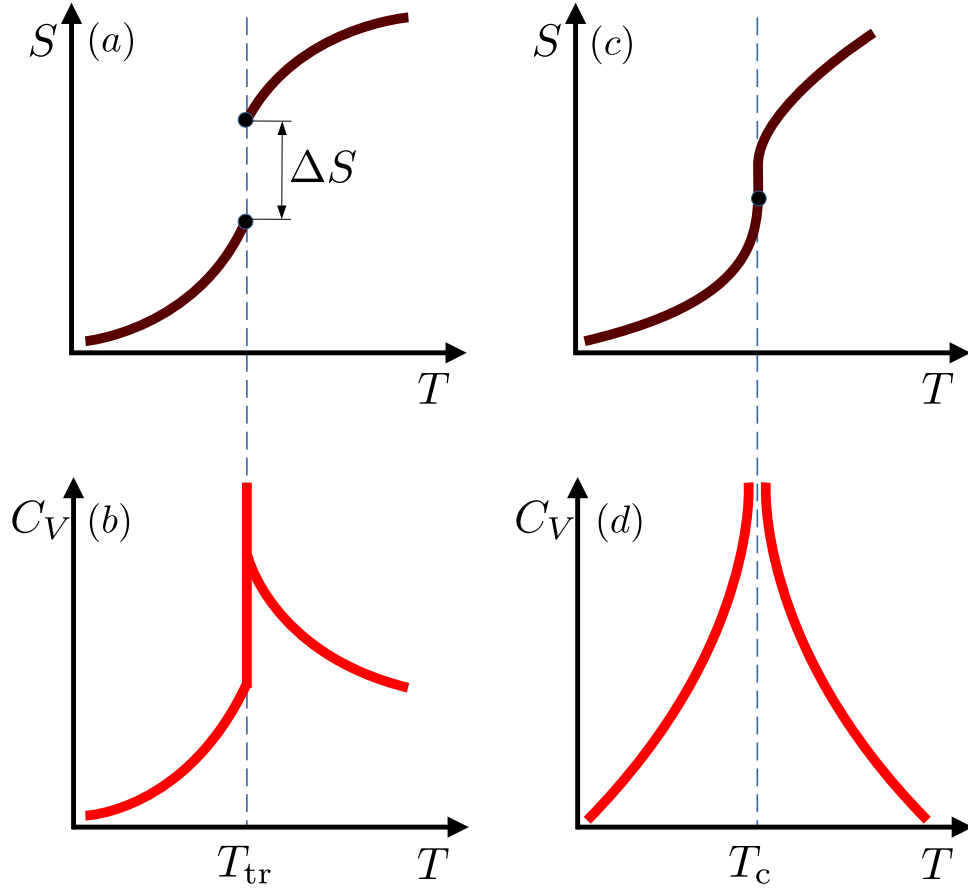


Figure 2.1: A schematic representation of entropy S and heat capacity C_V functions of temperature T for first-order (a, b) and second-order phase transitions (c, d).

as shown in Fig. 2.1(c) and Fig. 2.1(d). Compared to a first-order transition, ΔS is zero at the transition point, which means the latent heat $Q_{lat} = 0$ for second-order phase transitions. For this reason, there is no coexistence of two phases. Alternatively, second-order transitions can also be characterized by a simple order parameter O , which ideally exhibits step function behavior near the critical temperature T_c ,

$$O(T) \begin{cases} = 0, & T \geq 0, \\ \neq 0, & T < 0. \end{cases} \quad (2.10)$$

A prominent example is the magnetization M in the 2D Ising model [22]. Another interesting part that has been extensively studied for second-order transitions is the power-law behavior of response quantities such as the heat capacity near the critical temperature T_c . The heat capacity obeys the power-law behavior $C_V \approx |t|^{-\alpha}$, where $t = (T_c - T)/T$ is the reduced temperature. The critical exponents are used to identify universality classes that different systems with the same critical exponents belong to.

2.1.1 Statistical Ensembles

Classical equilibrium statistical mechanics was developed to connect the microscopic theory of system degrees of freedom with macroscopic thermodynamic properties. If a system consists of a few particles only, one can obtain the system behavior by solving the coupled equations of motion mathematically or numerically. However, the number of constituent particles in a macroscopic system is of the order of the Avogadro constant $N_A \approx 6 \times 10^{23} \text{mol}^{-1}$. Therefore, it is virtually impossible to solve equations of motion analytically or numerically for such a system. Instead, statistical mechanics approaches this problem by focusing on the microstate probability distribution. In the phase space of three-dimensional classical systems, a microstate of a system with N particles is given by

$$\mathbf{q} = (q_1, q_2, \dots, q_{3N}), \quad \mathbf{p} = (p_1, p_2, \dots, p_{3N}), \quad (2.11)$$

where (\mathbf{q}, \mathbf{p}) describes the generalized position vector of the system in the phase space of coordinates \mathbf{q} and momenta \mathbf{p} . In a statistical ensemble, each microstate state (\mathbf{q}, \mathbf{p}) is associated with its time-independent normalized phase space density $\rho(\mathbf{q}, \mathbf{p})$ that satisfies

$$\int \int d^{3N}q d^{3N}p \rho(\mathbf{q}, \mathbf{p}) = 1, \quad \rho(\mathbf{q}, \mathbf{p}) \geq 0, \quad (2.12)$$

which is a continuous probability distribution function (PDF). The ensemble average of an observable physical quantity $O(\mathbf{q}, \mathbf{p})$ is then defined as

$$\langle O \rangle \equiv \int d^{3N}q \int d^{3N}p O(\mathbf{q}, \mathbf{p}) \rho(\mathbf{q}, \mathbf{p}). \quad (2.13)$$

According to *Liouville's theorem* on the trajectories of degrees of freedom in phase space, the following relationship between phase density $\rho(\mathbf{q}, \mathbf{p})$ and system Hamiltonian $H(\mathbf{q}, \mathbf{p})$ holds:

$$\{\rho, H\} = \sum_{i=1}^{3N} \left(\frac{\partial \rho}{\partial q_i} \frac{\partial H}{\partial p_i} + \frac{\partial \rho}{\partial p_i} \frac{\partial H}{\partial q_i} \right) = \sum_{i=1}^{3N} \left(\frac{\partial \rho}{\partial q_i} \dot{q}_i + \frac{\partial \rho}{\partial p_i} \dot{p}_i \right) = 0. \quad (2.14)$$

A general way of satisfying the condition (2.14) is to assume that $\rho(\mathbf{q}, \mathbf{p})$ explicitly depends on the Hamiltonian $H(\mathbf{q}, \mathbf{p})$,

$$\rho(\mathbf{q}, \mathbf{p}) = \rho(H(\mathbf{q}, \mathbf{p})). \quad (2.15)$$

2.1.2 Microcanonical Ensemble

In a microcanonical ensemble, a macrostate of a system is typically defined by the number of particles N and energy E in a volume V . To avoid restricting degrees of freedom of the system in a state with energy E , we consider a thin hypershell of microstates that satisfies

$$\left(E - \frac{1}{2}\Delta \right) \leq H(\mathbf{q}, \mathbf{p}) \leq \left(E + \frac{1}{2}\Delta \right), \quad 0 < \frac{\Delta}{|E|} \ll 1. \quad (2.16)$$

As a result, the phase space density $\rho(\mathbf{q}, \mathbf{p})$ in this hypershell is constant:

$$\rho(\mathbf{q}, \mathbf{p}) = \rho(H(\mathbf{q}, \mathbf{p})) = \text{const.} \quad (2.17)$$

The enclosed phase space volume $\Gamma(E, V, N)$ is then given by

$$\Gamma(E, V, N) = \int \int_{(E - \frac{1}{2}\Delta) \leq H(\mathbf{q}, \mathbf{p}) \leq (E + \frac{1}{2}\Delta)} d^{3N}q d^{3N}p. \quad (2.18)$$

Consequently, according to the normalization condition (2.12), this leads to the uniform distribution of the phase space density $\rho(\mathbf{q}, \mathbf{p})$ in the microcanonical ensemble

$$\rho(\mathbf{q}, \mathbf{p}) = \begin{cases} \frac{1}{\Gamma(N, E, V)}, & (E - \frac{1}{2}\Delta) \leq H(\mathbf{q}, \mathbf{p}) \leq (E + \frac{1}{2}\Delta), \\ 0, & \text{otherwise.} \end{cases} \quad (2.19)$$

The phase space density $\rho(\mathbf{q}, \mathbf{p})$ can then also be written as

$$\rho(\mathbf{q}, \mathbf{p}) = \frac{\Theta\left(E + \frac{1}{2}\Delta - H(\mathbf{q}, \mathbf{p})\right) \Theta\left(H(\mathbf{q}, \mathbf{p}) - \left(E - \frac{1}{2}\Delta\right)\right)}{\int d^{3N}q \int d^{3N}p \Theta\left(E + \frac{1}{2}\Delta - H(\mathbf{q}, \mathbf{p})\right) \Theta\left(H(\mathbf{q}, \mathbf{p}) - \left(E - \frac{1}{2}\Delta\right)\right)}, \quad (2.20)$$

where the step function Θ is defined as $\Theta(x) = 1, \forall x \geq 0$ and $\Theta(x) = 0, \forall x < 0$. If the system volume V and the number of particles N are fixed, the phase space volume (2.18) is only a function of energy E and can be written as

$$\begin{aligned} \Gamma(E) &= \int d^{3N}q \int d^{3N}p \Theta\left(E + \frac{1}{2}\Delta - H(\mathbf{q}, \mathbf{p})\right) \Theta\left(H(\mathbf{q}, \mathbf{p}) - \left(E - \frac{1}{2}\Delta\right)\right) \\ &\equiv \int_{E - \frac{1}{2}\Delta}^{E + \frac{1}{2}\Delta} dE' g(E') \\ &\approx g(E) \int_{E - \frac{1}{2}\Delta}^{E + \frac{1}{2}\Delta} dE' = g(E)\Delta, \end{aligned} \quad (2.21)$$

where $g(E)$ is the density of states (number of microstates per energy available to the system).

Boltzmann remarkably connected thermodynamics with statistical mechanics by defining the entropy S as the logarithm of the phase space volume (or the number of available states in discrete

systems), $S = k_B \ln \Gamma$. For $E \approx \text{const}$, this can be written as

$$S(E) = k_B \ln \Gamma(E) = k_B \ln(g(E)\Delta) = k_B \ln g(E) + k_B \ln \Delta. \quad (2.22)$$

In computer simulations, the continuous energy space is usually discretized by energy bins with width Δ , and the number of states $g(E)$ is accumulated in this bin. Hence, the latter constant part of the entropy (2.22) is commonly ignored, especially when we study the change of the entropy S with respect to energy E . Therefore, the microcanonical Boltzmann entropy (2.22) is usually simplified to

$$S(E) = k_B \ln g(E). \quad (2.23)$$

When two closed systems with entropies $S_1(E_1, V_1, N_1)$ and $S_2(E_2, V_2, N_2)$ are in thermal contact, the total entropy S reaches its maximum in equilibrium

$$\begin{aligned} dS = 0 &= \frac{\partial(S_1(E_1, V_1, N_1) + S_2(E_2, V_2, N_2))}{\partial E_1} dE_1 + \frac{\partial(S_1(E_1, V_1, N_1) + S_2(E_2, V_2, N_2))}{\partial E_2} dE_2 \\ &= \frac{\partial S_1}{\partial E_1} dE_1 + \frac{\partial S_2}{\partial E_2} dE_2. \end{aligned} \quad (2.24)$$

Here we used the extensive nature of the entropy S . Since the combined system's total energy $E = E_1 + E_2$ is constant, $dE_1 = -dE_2$. The equilibrium condition $\partial S_1/\partial E_1 = \partial S_2/\partial E_2$ can be used to define the microcanonical temperature

$$T_{\text{micro}}(E) \equiv \left(\frac{\partial S}{\partial E} \right)^{-1}. \quad (2.25)$$

Therefore, it is noteworthy that the microcanonical temperature $T_{\text{micro}}(E)$ is a **system property**, which describes the change of the (logarithmic) density of states (or number of states for discrete systems) with respect to system energy E . The relationship between S and E as given by Eq. (2.25) suggests that the inverse temperature $\beta = 1/T_{\text{micro}}(E)$ is actually the more appropriate macrostate variable.

2.1.3 Canonical Ensemble

Unlike the microcanonical ensemble, where the energy of the system is fixed, the standard variables in the canonical ensemble are (N_1, V_1, T_1) . This means that there is energy exchange between the system A_1 with energy E_1 and the heat bath A_2 with energy E_2 , while the number of particles N and the volume V are kept constant for both. Moreover, the total energy of the combined system is constant, and the heat bath energy E_2 is assumed to be much larger than the system energy E_1 ,

$$E_1 + E_2 = E = \text{const}, \quad E_2 \gg E_1. \quad (2.26)$$

Under the assumption of asymptotically small interactions, the Hamiltonian of the combined system can then be written as

$$H(\mathbf{q}_1, \mathbf{p}_1; \mathbf{q}_2, \mathbf{p}_2) \approx H_1(\mathbf{q}_1, \mathbf{p}_1) + H_2(\mathbf{q}_2, \mathbf{p}_2). \quad (2.27)$$

Since the combined system is an isolated system with constant energy E , the overall phase space density $\rho(\mathbf{q}, \mathbf{p})$ of the combined system is given in the microcanonical ensemble by Eq. (2.20):

$$\rho(\mathbf{q}, \mathbf{p}) = \frac{\Theta\left(E + \frac{1}{2}\Delta - (H_1 + H_2)\right) \Theta\left(H_1 + H_2 - \left(E - \frac{1}{2}\Delta\right)\right)}{\int d^{3N}q \int d^{3N}p \Theta\left(E + \frac{1}{2}\Delta - (H_1 + H_2)\right) \Theta\left(H_1 + H_2 - \left(E - \frac{1}{2}\Delta\right)\right)}, \quad (2.28)$$

where $N = N_1 + N_2$ is the total number of particles and (\mathbf{q}, \mathbf{p}) is the formal phase space vector of the combined system. Hence, we can obtain the system phase space density $\rho_1(\mathbf{q}_1, \mathbf{p}_1)$ by

integrating out the heat bath degrees of freedom

$$\begin{aligned}
\rho_1(\mathbf{q}_1, \mathbf{p}_1) &= \int d^{3N_2} q_2 d^{3N_2} p_2 \rho(\mathbf{q}, \mathbf{p}) \\
&= \frac{\int d^{3N_2} q_2 d^{3N_2} p_2 \Theta\left(E - H_1 + \frac{1}{2}\Delta - H_2\right) \Theta\left(H_2 - \left(E - H_1 - \frac{1}{2}\Delta\right)\right)}{\int d^{3N} q \int d^{3N} p \Theta\left(E + \frac{1}{2}\Delta - (H_1 + H_2)\right) \Theta\left(H_1 + H_2 - \left(E - \frac{1}{2}\Delta\right)\right)} \\
&\propto \frac{\Gamma_2(E - H_1)}{\Gamma(E)}, \tag{2.29}
\end{aligned}$$

where $\Gamma_2(E - H_1)$ is the phase space volume of the heat bath A_2 . Since the phase space volume $\Gamma(E)$ of the combined system is constant, we obtain

$$\rho_1(\mathbf{q}_1, \mathbf{p}_1) \propto \Gamma_2(E - H_1). \tag{2.30}$$

Under the condition that the energy of the heat bath is much larger than the system energy, $(E_1/E) \ll 1$, we can carry out a Taylor expansion of $\ln \Gamma_2(E - H_1)$ around $E_2 = E - H_1 \approx E$,

$$\begin{aligned}
\ln \Gamma_2(E - H_1) &= \ln \Gamma_2(E_2) = \ln \Gamma_2(E) + \left(\frac{\partial \ln \Gamma_2(E_2)}{\partial E_2} \right)_{E_2=E} (E_2 - E) + \dots \\
&\approx \text{const} + \left(\frac{\partial (S_2(E_2)/k_B)}{\partial E_2} \right)_{E_2=E} (-H_1) = \text{const} - \frac{1}{k_B T_2} H_1 = \text{const} - \beta_2 H_1, \tag{2.31}
\end{aligned}$$

where $\beta_2 = 1/k_B T_2$. In equilibrium, the system and the heat bath shares the same temperature, so we replace β_2 by β . Moreover, according to the proportional relationship with phase space density and the phase space volume (2.31) and the result for the phase space volume (2.30), the system's phase space density $\rho_1(\mathbf{q}_1, \mathbf{p}_1)$ is

$$\rho_1(\mathbf{q}, \mathbf{p}) \propto \Gamma_2(E - H_1) \propto \exp[-\beta H_1(\mathbf{q}, \mathbf{p})]. \tag{2.32}$$

However, more of the interest is focused on the system's canonical energy distribution $\rho_1(E_1)$, which can be obtained by using the form of the phase space volume (2.21),

$$\begin{aligned}\rho_1(E_1) &= \int d^{3N_1}q_1 d^{3N_1}p_1 \rho_1(\mathbf{q}_1, \mathbf{p}_1) \delta(E_1 - H_1(\mathbf{q}_1, \mathbf{p}_1)) \\ &\propto \exp(-\beta E_1) \int d^{3N_1}q_1 d^{3N_1}p_1 \delta(E_1 - H_1(\mathbf{q}_1, \mathbf{p}_1)) \\ &\propto g_1(E_1) \exp(-\beta E_1),\end{aligned}\tag{2.33}$$

where we have introduced the density of system states $g_1(E_1)$. Proper normalization yields

$$\rho_1(E_1) = \frac{g_1(E_1) \exp(-\beta E_1)}{\int g_1(E_1) \exp(-\beta E_1) dE_1} = \frac{g_1(E_1) \exp(-\beta E_1)}{Z_{\text{can}}},\tag{2.34}$$

where $Z_{\text{can}} \equiv \int g_1(E_1) \exp(-\beta E_1) dE_1$ is the canonical partition function of the system. For simplicity, we use E for the system energy, ρ for the system phase space density, and $g(E)$ for the system density of states in the following. Therefore, the ensemble average (2.13) of a physical quantity $O(E)$ in the canonical ensemble can be measured in the energy space by

$$\langle O(E) \rangle = \int O(E) \rho(E) dE = \frac{\int O(E) g(E) \exp(-\beta E) dE}{Z_{\text{can}}},$$

from which we can get the generalized formula for the thermal fluctuations of the quantity

$$\begin{aligned}\frac{d\langle O \rangle}{dT} &= \frac{d}{dT} \int O \rho(E) dE \\ &= \frac{d\beta}{dT} \frac{d}{d\beta} \int O \rho(E) dE \\ &= \frac{1}{k_B T^2} \left[\int O E \rho(E) dE - \left(\int O \rho(E) dE \right) \left(\int E \rho(E) dE \right) \right] \\ &= \frac{1}{k_B T^2} (\langle O E \rangle - \langle O \rangle \langle E \rangle).\end{aligned}\tag{2.35}$$

The discrete form of this fluctuation formula is commonly used to estimate fluctuations in computer simulations.

In addition, it is noteworthy to mention the difference between the heat bath temperature T and the microcanonical temperature (2.25). In the canonical ensemble, the heat bath temperature T is expressed as

$$T = \left(\frac{\partial S}{\partial U} \right)_{N,V}^{-1}, \quad (2.36)$$

where the internal energy $U = \langle E \rangle$ is constant and the system energy E fluctuates. Only in the thermodynamic limit ($N \rightarrow \infty$), these two temperatures are equal to each other, where the fluctuation scales as $1/\sqrt{N}$ and then $U \approx E$.

2.2 Conventional Study of Phase Transitions in Finite Systems

There are only a few infinitely large systems, for which phase transitions can be studied analytically, such as the 2D square lattice Ising model for studying interacting magnetic spins without external magnetic field [23] and the Van der Waals equation of state for describing gas-liquid phase transitions [24]. For more complex systems, it is virtually impossible to find analytical solutions. Examples include the 3D Ising model or the 2D Ising model with an external magnetic field $H \neq 0$. Thus, numerical studies of complex systems by computer simulations have become one of the most powerful tools to study phase transitions. However, only finite systems can be simulated, and thermodynamic potentials or response quantities don't experience discontinuities or divergences. Therefore, peaks or shoulders of response quantities are extensively studied for phase transitions in finite systems.

In finite-size systems, a first-order transition is usually indicated by bimodal distribution function $P(E)$. The normalized canonical energy distribution functions and the normalized heat capacities (specific heat) are shown in Fig. 2.2 for a 40×40 , $q = 7$ Potts model and a flexible polymer model with 55 monomers. Both systems undergo a first-order transition. The characteristic double-peak

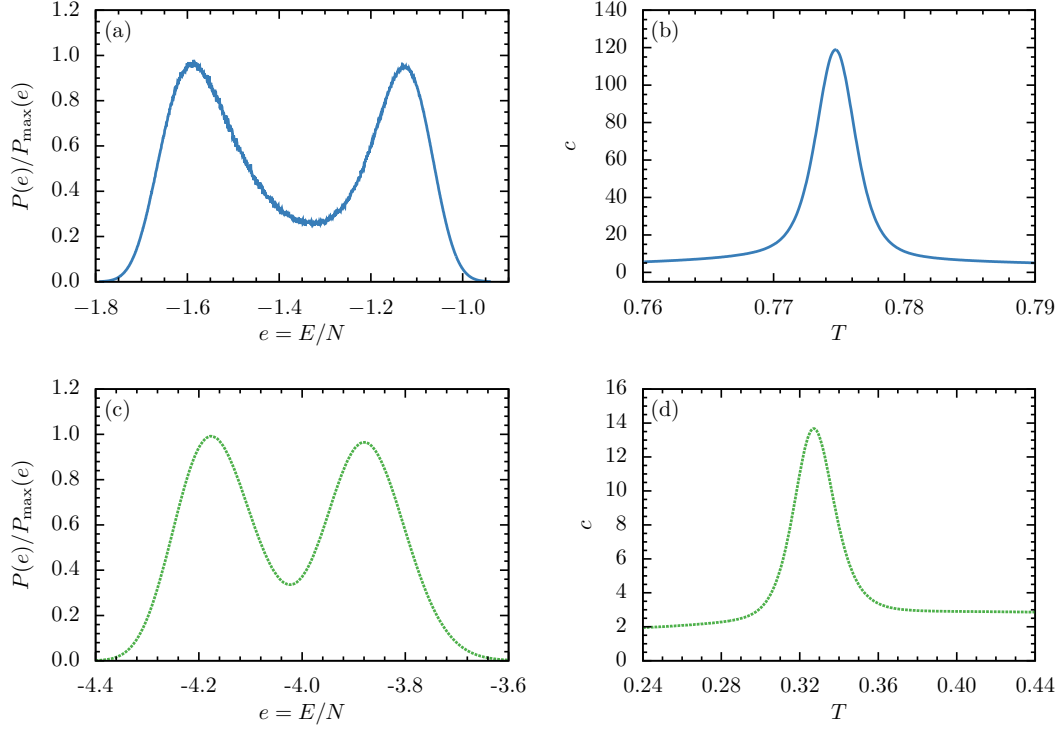


Figure 2.2: (a) Normalized canonical energy distribution function at the first-order transition temperature, and (b) specific heat as a function of temperature for a 40×40 , $q = 7$ Potts model. (c) Normalized canonical energy distribution function at the first-order freezing transition temperature, and (d) specific heat as a function of temperature for a flexible polymer model with 55 monomers. Results are obtained from Monte Carlo simulations.

behavior of the canonical energy distribution is caused by the coexistence of two phases. Moreover, corresponding heat capacities only show finite peaks. It is expected that, if there is a thermodynamic limit for the system, the bimodal distribution will be more sharply distributed, and the heat capacity will show similar features as sketched in Fig. 2.1.

For the second-order transitions in finite systems, it is usually necessary to look at more than one quantity. In the example of the 2D square lattice Ising model, the system is known to possess a second-order transition between the ferromagnetic phase and the paramagnetic phase at a finite temperature [25]. Monte Carlo simulation results of various sizes of the 2D Ising model are shown in Fig. 2.3. For all simulated system sizes, the heat capacity curves exhibit finite peaks indicating the transition instead of discontinuities as described in Section 2.1 due to finite-size effects. The peak location of the magnetic susceptibility χ for the same transition is not identical to the specific

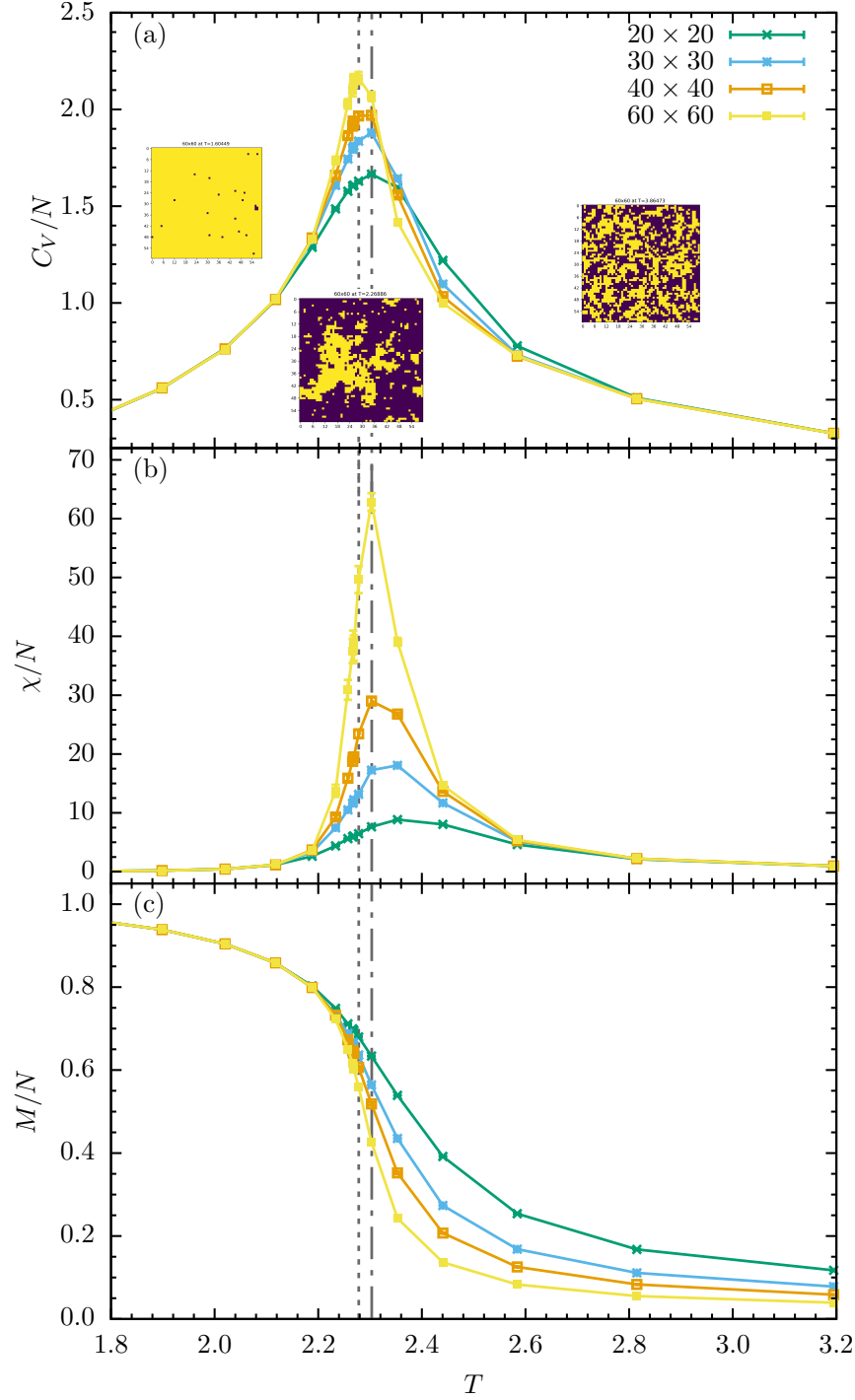


Figure 2.3: (a) Specific heat C_V/N (normalized heat capacity) along with typical spin configurations at different temperatures, (b) normalized magnetic susceptibility χ/N , and (c) normalized magnetization M/N for various sizes of 2D Ising models without external field, obtained from Monte Carlo simulations. The dotted line indicates the peak location of the heat capacity and the dashed line indicates the peak location of the susceptibility for the system size of 60×60 .

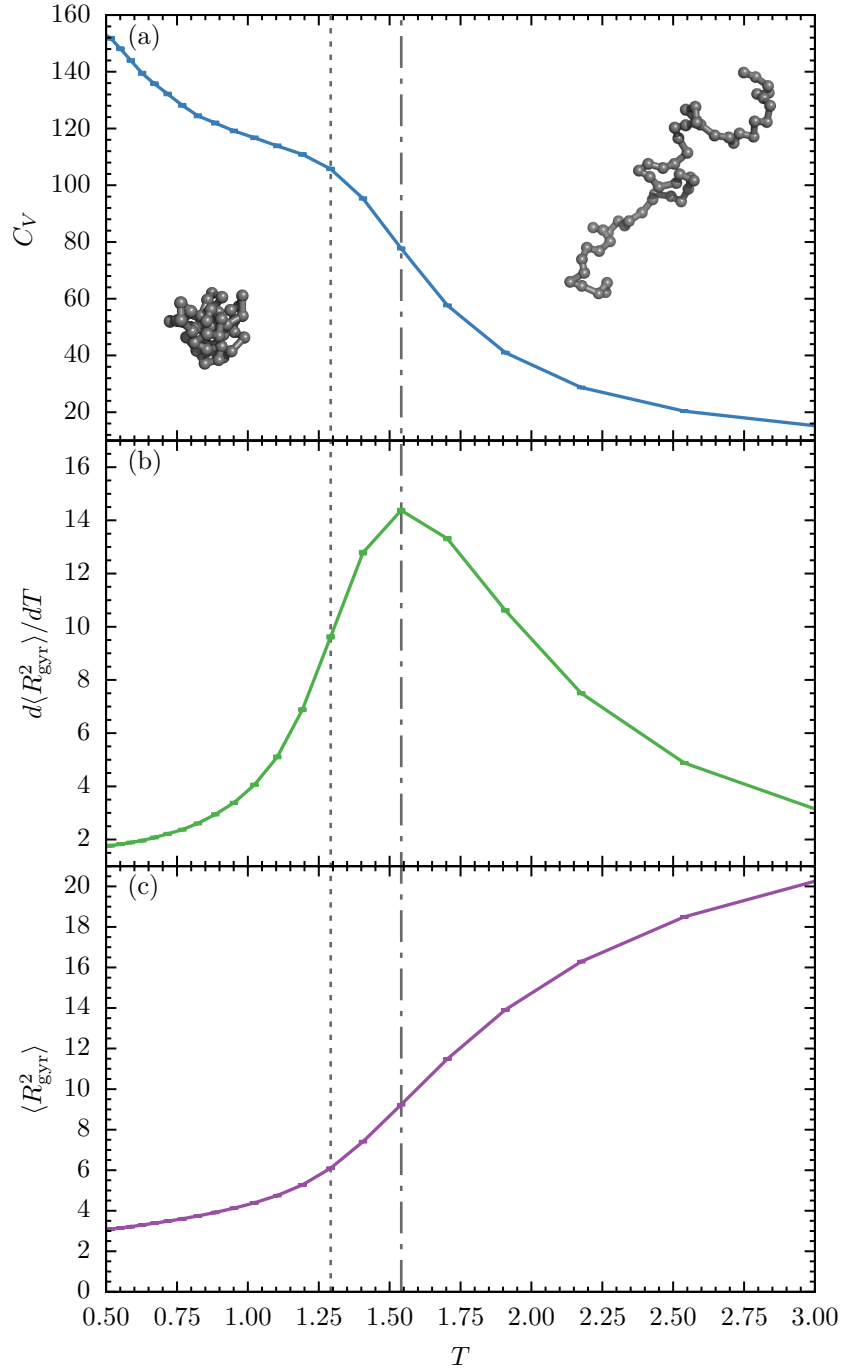


Figure 2.4: (a) Specific heat C_V along with typical polymer conformations from two phases, (b) fluctuations of square radius of gyration $d\langle R_{\text{gyr}}^2 \rangle / dT$, and (c) squared radius of gyration $\langle R_{\text{gyr}}^2 \rangle$ as an order parameter for a 55-mer flexible polymer model, obtained from Monte Carlo Simulations. The dotted line indicates the shoulder location in the heat capacity C_V , and the dashed line indicates the peak location in the fluctuations of the square radius of gyration $d\langle R_{\text{gyr}}^2 \rangle / dT$.

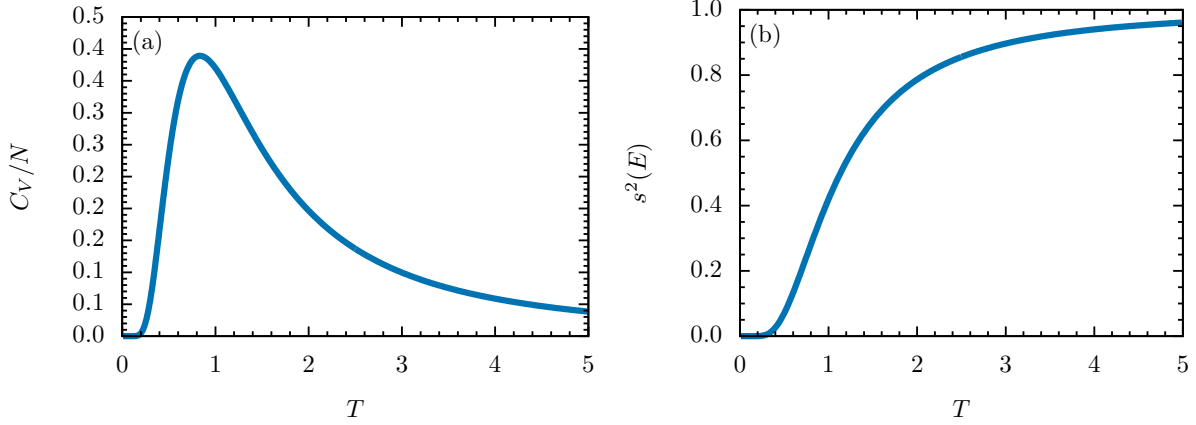


Figure 2.5: (a) Specific heat $C_V/N = (1/N)d\langle E \rangle/dT$ as a function of temperature T , and normalized energy variance $s^2(E) = (-1/N)d\langle E \rangle/d\beta$ as a function of inverse temperature β for 1D-Ising model with periodic boundary conditions in the thermodynamic limit.

heat. This peak location difference is also known as the transition band for finite-size systems, making it difficult to uniquely identify the transition points. Moreover, as shown in Fig. 2.3(c), the magnetization M is a proper order parameter for this system. Furthermore, we can easily observe from Fig. 2.3 that the larger the system size, the closer the results are to the expected behavior in the thermodynamic limit. Therefore, finite-size scaling can be performed to extrapolate finite-size results to the thermodynamic limit. Then the transition temperature of the infinitely large system is identified from the convergence of transition temperatures by the scaling. Similar second-order behavior can also be observed in polymer models for the collapse transition (also known as Θ transition). The results of a flexible polymer model are shown in Fig. 2.4 for a chain with 55 monomers. However, the heat capacity C_V only shows a shoulder for this transition. Thermal fluctuations of the square radius of gyration $\langle R_{\text{gyr}}^2 \rangle$ show a peak for the transition at a different temperature. Again, as illustrated, the transition bandwidth problem persists.

Nonetheless, peaks or shoulders in response quantities have been widely used as indicators of phase transitions in finite systems and large efforts have been dedicated to finding appropriate system-specific order parameters. However, peaks of them are not safe indicators and typically suffer from ambiguity. Although a finite-temperature peak in the specific heat curve for the 1D Ising model with periodic boundary condition survives in the thermodynamic limit, it is not associated

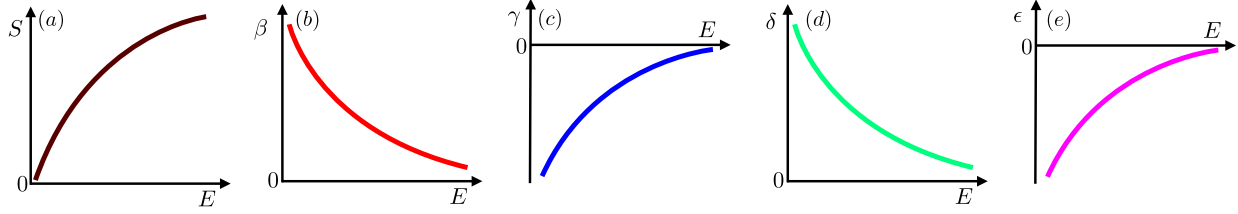


Figure 2.6: Typical monotonic behavior of microcanonical entropy (a) $S(E)$ and first- to fourth-order derivatives (b) $\beta = dS/dE$; (c) $\gamma = d^2S/dE^2$; (d) $\delta = d^3S/dE^3$; (e) $\epsilon = d^4S/dE^4$, if no transition occurs.

with any transition. Interestingly, if we define a normalized fluctuation term $s^2(E)$ as the derivative of the average energy with respect to the inverse temperature β , which corresponds to the variance of the energy,

$$s^2(E) = - \left(\frac{1}{N} \right) \frac{d\langle E \rangle}{d\beta} = \left(\frac{1}{N} \right) (\langle E^2 \rangle - \langle E \rangle^2), \quad (2.37)$$

the peak actually disappears, as shown in Fig. 2.5. The $1/T^2$ term in the specific heat function may cause artificial peaks. This disappearance suggests again that inverse temperature might be a better natural variable than temperature. It is important to note that biological systems are finite in nature and finite-size scaling is not usually applicable to these systems. Since canonical statistical analysis is inconsistent and ambiguous for finite systems, it is necessary to explore the other types of statistical analysis. One candidate is the generalized microcanonical inflection-point analysis that extends the theory of phase transition. It provides a systematic and consistent approach to phase transitions in systems of any size. It will be introduced in detail in the next section.

2.3 Generalized Microcanonical Inflection-Point Analysis

The generalized inflection-point analysis method [13] for the systematic identification and classification of transitions in systems of any size has been introduced recently. This method, which combines microcanonical thermodynamics [10] and the principle of minimal sensitivity [11, 12], has already led to novel insights into the nature of phase transitions. Even the Ising model, which has been excessively studied for almost a century, possesses a more complex phase structure than

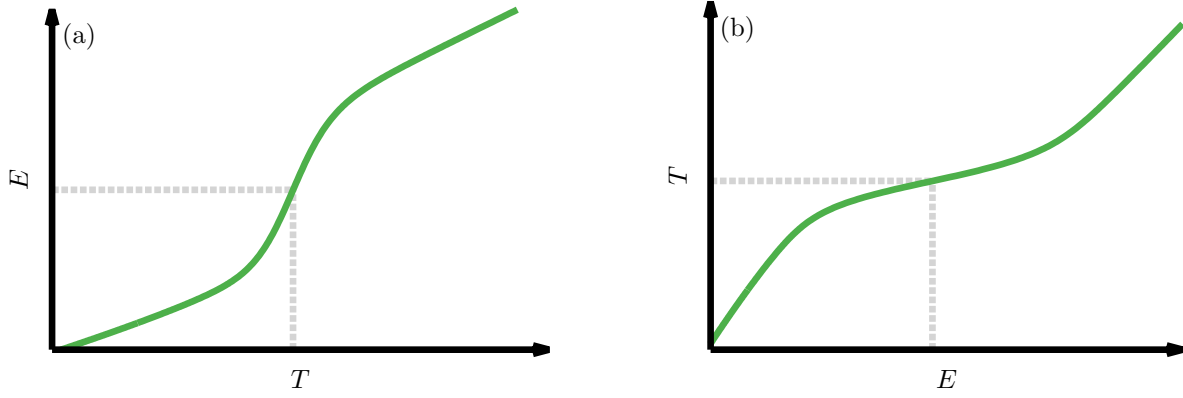


Figure 2.7: Typical sketch plot of (a) energy E versus temperature T around transition point for finite systems, and (b) temperature T versus energy E . Transition points are indicated by dotted lines.

previously known, as recent studies showed [26–28]. Besides, this method has been helpful for studies in characterization of aggregation with a generalized model [29], self-assembly kinetics in macromolecular systems [30], as well as in studies of the general geometric and topological foundation of transitions in phase space [31–34]. In addition, this method motivated further investigation of higher order derivatives of Boltzmann microcanonical entropy with an additional conserved quantity [35]. Interestingly, this method has also been used as justification for pattern recognition criteria in computer science [36].

Boltzmann’s formula of the microcanonical entropy can be written as $S(E) = k_B \ln g(E)$, where $g(E)$ is the density of states with energy E . As shown in Fig. 2.6, when not experiencing phase transitions, the curves of entropy $S(E)$ and its derivatives exhibit well-defined concave or convex monotony. However, phase space changes caused by phase transitions in the system will be reflected in the entropy. From the canonical statistical analysis of first- and second-order transitions, it is known that entropy and/or internal energy rapidly change (or are most sensitive), if the temperature is varied near the transition point, as sketched in Fig. 2.7 (a). It can also be interpreted as shown in Fig. 2.7(b), where the temperature change is the least sensitive to the change of the energy near the transition point. This behavior corresponds to the least-sensitive dependencies of microcanonical quantities in the space of system energies. Thus, a phase transition

causes a least-sensitive inflection point in the entropy or its higher derivatives and impacts their monotonic behavior. As a result, the derivatives of inflection points will be either minimum or maximum at their locations in the energy space. By systematically analyzing these alterations, different types of transitions can be identified and classified.

In this scheme, a first-order transition in $S(E)$ is signaled by a least-sensitive inflection point with energy E_{tr} . Therefore, the originally monotonically decreasing first derivative, which is the inverse microcanonical temperature $\beta(E) \equiv dS/dE$, forms a backbending region as shown in Fig. 2.8 (a) that leads to a positive valued minimum in $\beta(E)$ at E_{tr} ,

$$\beta(E_{\text{tr}}) = \left. \frac{dS(E)}{dE} \right|_{E=E_{\text{tr}}} > 0. \quad (2.38)$$

Similarly, if there is a least-sensitive inflection point in $\beta(E)$, the phase transition is classified as a second-order transition. As shown in Fig. 2.8 (b), the derivative of $\beta(E)$ has a negative-valued peak at the transition energy E_{tr} ,

$$\gamma(E_{\text{tr}}) = \left. \frac{d^2S(E)}{dE^2} \right|_{E=E_{\text{tr}}} < 0. \quad (2.39)$$

More specifically, we call this an *independent* second-order transition. This implies that there is another transition type: *dependent* transitions. As the name suggests, dependent transitions are associated with an independent transition of lower-order rank. It is important to note that not all independent transitions have a dependent companion. However, if it exists - and it can only exist at a higher transition energy than its independent partner — it serves as a precursor of the independent transition in the disordered phase. The inflection points of *dependent* transitions are located within the backbending region of the entropy derivatives. For example, if this inflection point is located within the backbending region of the inverse temperature $\beta(E)$, which is associated with the first-order transition, the transition is a dependent second-order transition, as sketched in Fig. 2.9 (a). Consequently, there is a positive-valued minimum in the derivative of $\beta(E)$ at the

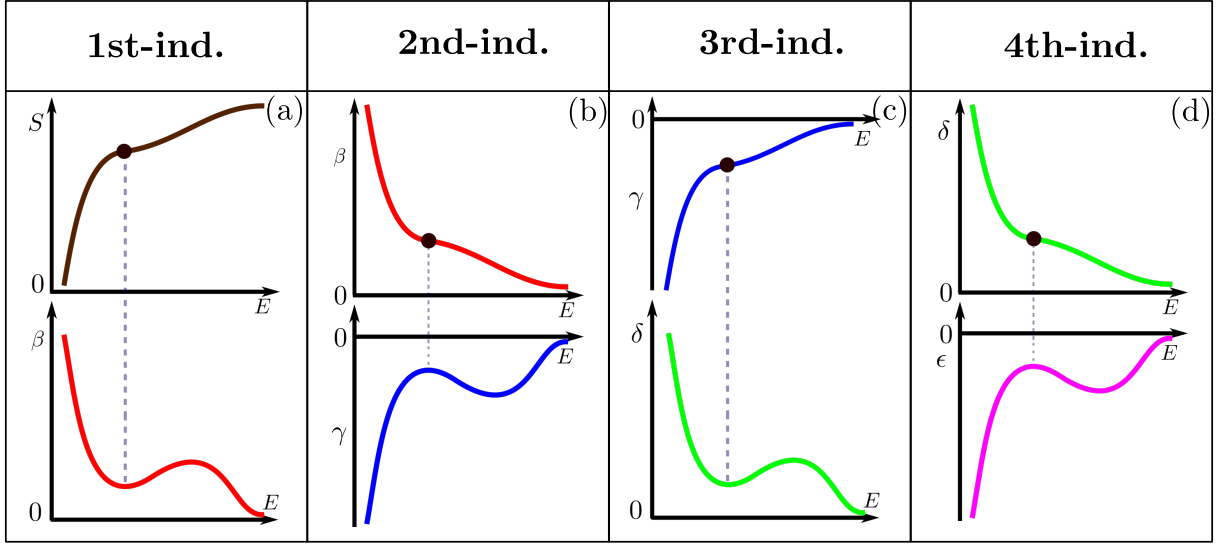


Figure 2.8: Sketch of *independent transitions* up to fourth order as defined in the microcanonical inflection point analysis method. (a) A first-order independent transition is defined by the inflection point in $S(E)$ and identified from the backbending of $\beta = dS/dE$ that possesses a positive minimum. (b) A second-order independent transition is defined by the inflection point in $\beta = dS/dE$ and identified from the backbending of $\gamma = d^2S/dE^2$ with a negative maximum. (c) A third-order independent transition is defined by the inflection point in $\gamma = d^2S/dE^2$ and identified from the backbending of $\delta = d^3S/dE^3$ that possesses a positive minimum. (d) A fourth-order independent transition is defined by the inflection point in $\delta = d^3S/dE^3$ and identified from the backbending of $\epsilon = d^4S/dE^4$ with a negative maximum.

transition energy $E_{\text{tr}}^{\text{dep}}$,

$$\gamma(E_{\text{tr}}^{\text{dep}}) = \left. \frac{d^2 S(E)}{dE^2} \right|_{E=E_{\text{tr}}^{\text{dep}}} > 0. \quad (2.40)$$

The identification can then be generalized by systematically analyzing these signals. For an independent transition of odd order $(2k - 1)$ (k is a positive integer), the $(2k - 1)$ th derivative of $S(E)$ possesses a positive-valued minimum,

$$\left. \frac{d^{(2k-1)} S(E)}{dE^{(2k-1)}} \right|_{E=E_{\text{tr}}} > 0, \quad (2.41)$$

and an independent transition of even order $2k$ is characterized by a negative-valued peak in the $2k$ th derivative,

$$\left. \frac{d^{2k} S(E)}{dE^{2k}} \right|_{E=E_{\text{tr}}} < 0. \quad (2.42)$$

A dependent transition of even order $2k$ is identified by a positive-valued minimum in the $2k$ th derivative,

$$\left. \frac{d^{2k} S(E)}{dE^{2k}} \right|_{E=E_{\text{tr}}^{\text{dep}}} > 0, \quad (2.43)$$

while for odd order $2k + 1$:

$$\left. \frac{d^{(2k+1)} S(E)}{dE^{(2k+1)}} \right|_{E=E_{\text{tr}}^{\text{dep}}} < 0. \quad (2.44)$$

Although dependent transitions are less common than independent transitions, they still provide valuable insights into the nature of transitions. In the microcanonical inflection point study of the 2D Ising model, a third-order dependent transition is identified [28], which involves a collective preordering of spins in the higher temperature region than the critical temperature. However, in this polymer study, dependent transitions were not found.

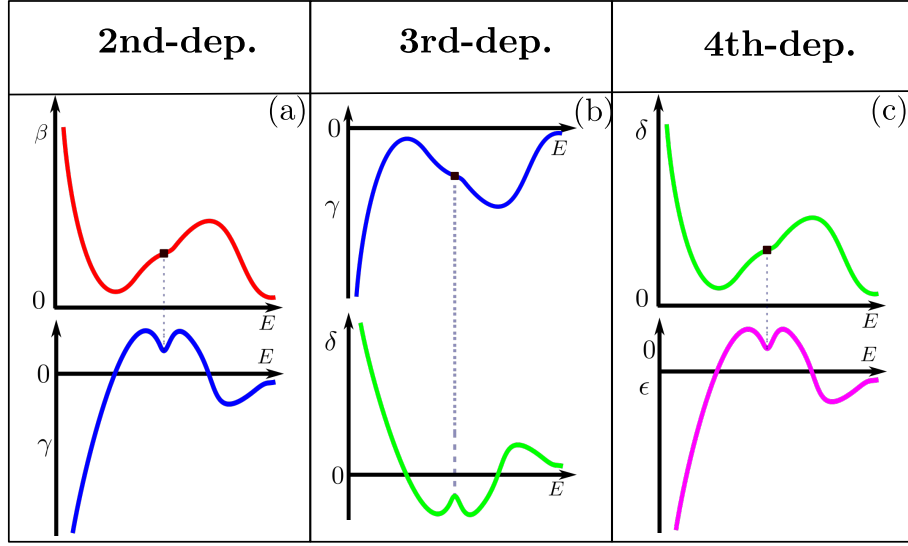


Figure 2.9: Sketch of *dependent transitions* up to fourth order as defined in the microcanonical inflection point analysis method. The inflection points are located in the entropy derivatives' backbending region that are resulted by lower order independent transitions. (a) A dependent second-order transition is defined by the inflection point within backbending region of $\beta = dS/dE$ and identified from a positive minimum in $\gamma = d^2S/dE^2$. (b) A dependent third-order transition is defined by the inflection point within backbending region of $\gamma = d^2S/dE^2$ and identified from a negative maximum in $\delta = d^3S/dE^3$. (c) A dependent fourth-order transition is defined by the inflection point within backbending region of $\delta = d^3S/dE^3$ and identified from a positive minimum in $\epsilon = d^4S/dE^4$.

CHAPTER 3

MODEL AND METHODS

3.1 Model

Coarse-grained Models of Biopolymers

In recent years, substantial research interest has been dedicated to applications in microbiology and nanotechnology on microscopic and mesoscopic scales, where surface effects can not be ignored. Different aspects of biomolecules have been studied extensively. As biomolecules fold into specific structures to perform biological functions in living cells, the computational modeling of these biopolymers, with the advantage of more precise control compared to experiments, has been a crucial way to study structural transitions, which furthermore leads to applications in many areas, e.g., drug discovery and design [37–40]. Biopolymers are so complex that different scales of simulations have been developed with different resolutions. All-atom simulations provide relatively high resolution about local structure dynamics, but with very high computational cost and only on a limited timescale [41, 42]. In addition, all-atom simulations require “force field” parameters which are usually of the order of $\mathcal{O}(10^3)$ [43] and not easily generalizable. On the other hand, coarse-grained models offer the advantage of lower computational cost that enables the study on a longer timescale and/or larger size by integrating out less relevant degrees of freedom. As shown

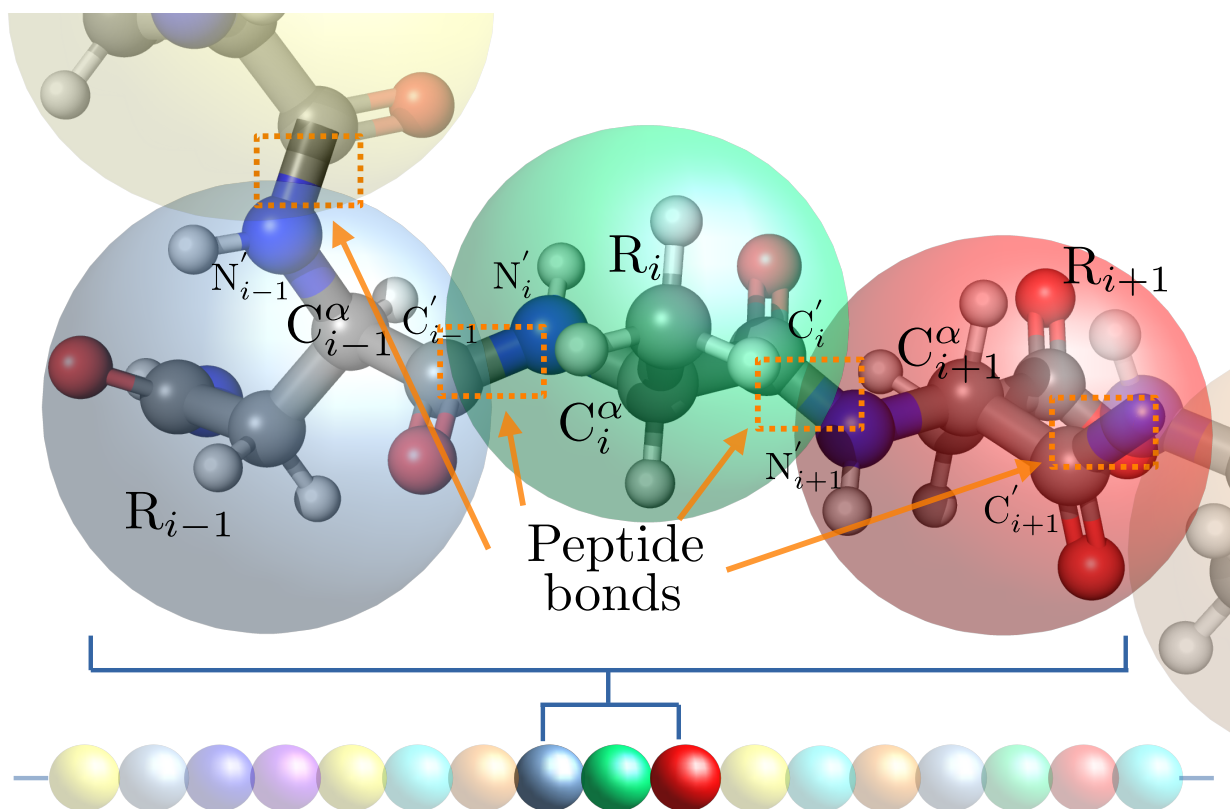


Figure 3.1: A coarse-graining procedure of a protein. Each monomer i represents an amino acid with side groups R_i that are connected by peptide bonds, which are shown as orange dotted rectangles. Some key atoms in the polypeptide chain are also labeled.

in Figure 3.1, a protein can be coarse-grained by using monomers to represent amino acids. The underlying quantum/atomic interactions are replaced by effective interactions between monomers. This approach, as a result, dramatically reduces computational costs. The amino acid sequence is also known as the primary structure of proteins. It is worth mentioning that, depending on the coarse-graining level, a monomer can also represent a smaller or larger group of repeating structures or subunits.

Moreover, coarse-grained modeling allows for the systematic study of specific aspects and thus provides a generic insight into the macroscopic properties that are not limited to specific biomolecules. For example, more than 200,000 protein structures are available in the protein

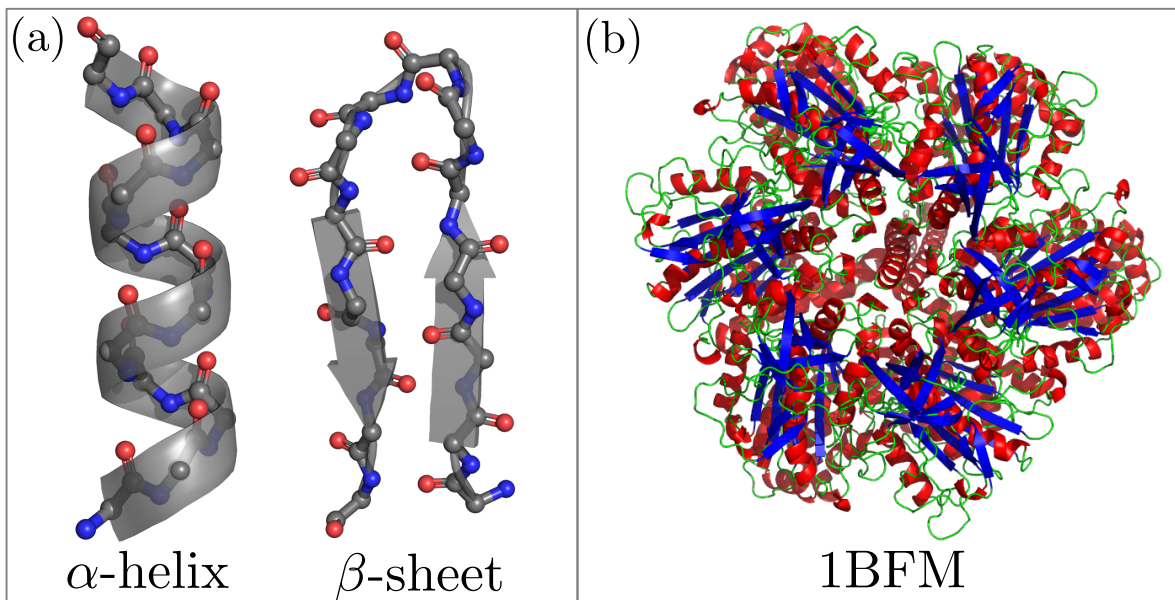


Figure 3.2: (a) Sketch (transparent gray) of two common secondary structures, α -helix and β -sheet, abstracted from the local spatial conformation of the polypeptide backbones. Carbon atoms are colored gray, nitrogen atoms are colored blue, and oxygen atoms are colored red. Side chains are not shown for clarity. (b) Structure of bovine mitochondrial F1-ATPase, PDB ID: 1BFM (<http://doi.org/10.2210/pdb1BMF/pdb>), using secondary structure representation. α -helix parts are colored in red and β -sheet parts are colored in blue.

data bank [44]. Although different in detailed structures, these proteins share similar secondary structures, in which α -helices and β -sheets are most common. The secondary structures are illustrated in Figure 3.2 (a). Additionally, as an example of representing a protein structure by secondary structures, bovine mitochondrial F1-ATPase [45] is visualized in Figure 3.2 (a), which is an enzyme protein for ATP synthesis. Paul D. Boyer and John E. Walker won 1997 the Nobel Prize in Chemistry for the determination of its structure and the explanation of the underlying enzymatic mechanism [46].

Coarse-grained Semiflexible Polymer Model

DNA, RNA, and even some proteins are classified as semiflexible polymers, which are characterized by their bending stiffness and finite persistence length. Moreover, bending stiffness has a different impact on biological functions and processes. It helps DNA pack in an organized way for efficient translations and transcription [47], which is important because DNA's length is extremely long compared to the size of the cell nucleus it resides in. RNA stiffness affects the self-assembly of virus particles [48]. Therefore, modeling semiflexible polymers has been of great interest. One of the simplest semiflexible polymer models is the well-known Krathy-Porod or worm-like-chain (WLC) model [14], which has been successfully used in studies of several structural and dynamic properties of semiflexible polymers. However, the lack of self-interactions in this model does not allow for the study of structural phase transitions in semiflexible polymers. Therefore, more complex coarse-grained models have been used widely to study different aspects of semiflexible polymers. Lattice models provide computational efficiency [49–51]. The more general continuum bead-stick and bead-spring models have been used to study structural phases of a single polymer [15–21], aggregation in bulk [52–55], and adsorption [56–59]. Conventional canonical analysis is mostly used in these studies. Especially, Seaton et al., (2013) [15] constructed the phase diagram for semiflexible polymers with $N = 30$ monomers canonically. In contrast, we have used the microcanonical inflection point analysis method to systematically investigate structural phase

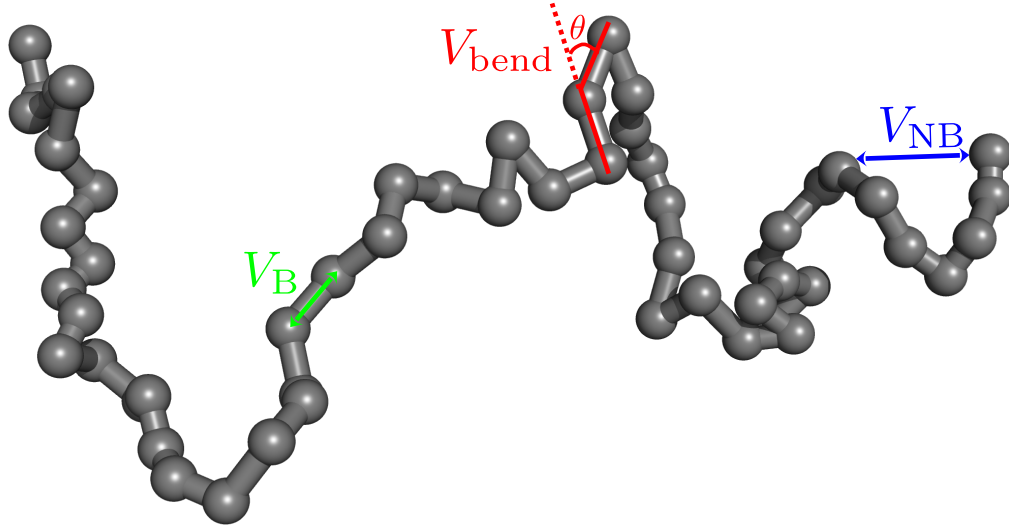


Figure 3.3: Schematic representation of interactions for a chain of $N = 55$ monomers. The bonded potential (green) V_B is highlighted for a pair of bonded monomers, the non-bonded potential (blue) V_{NB} for a pair of non-bonded monomers, and bending penalty V_{bend} (red) for two consecutive bonds that are characterized by bending angle θ .

transitions for semiflexible polymers with a generic coarse-grained semiflexible polymer model, and attempt to construct the first microcanonical phase diagram for semiflexible polymers.

Interaction Potentials and Energy Formation

For our study, we use a generalized semiflexible homopolymer model. In such a model, the total energy of a polymer chain with N monomers is composed of contributions from non-bonded and bonded interactions between monomers, along with an energetic bending penalty.

For the interactions between non-bonded monomers, we employ the standard 12-6 Lennard-Jones (LJ) potential [60]:

$$V_{\text{LJ}}(r) = 4\epsilon_{\text{LJ}} \left[\left(\frac{\sigma}{r} \right)^{12} - \left(\frac{\sigma}{r} \right)^6 \right]. \quad (3.1)$$

This potential originated from describing effective dipole-dipole interactions and effective repulsion of overlapping electronic clouds. Here, r is the monomer-monomer distance, $\sigma = 2^{-1/6}r_0$ is the van der Waals distance associated with the potential minimum at r_0 , and ϵ_{LJ} is the energy scale. For

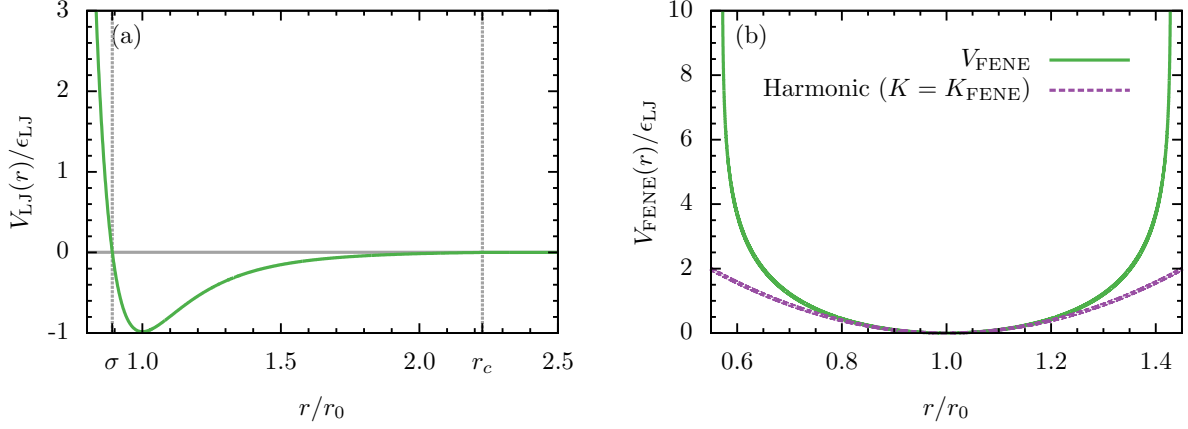


Figure 3.4: (a) Plot of the Lennard-Jones potential $V_{\text{LJ}}(r)/\epsilon_{\text{LJ}}$ versus monomer distance r/r_0 . Van der Waals distance σ and cutoff r_c are also labeled. (b) FENE potential $V_{\text{FENE}}(r)/\epsilon_{\text{LJ}}$ (solid) and harmonic potential (dashed) with the same elasticity as the FENE potential plotted as functions of bond length r/r_0 .

computational efficiency, we introduce a cutoff at $r_c = 2.5\sigma$. Shifting the potential by the constant $V_{\text{shift}} \equiv V_{\text{LJ}}(r_c)$ avoids a discontinuity at r_c , as shown in Figure 3.4 (a).

Thus, the potential energy of non-bonded monomers is given by

$$V_{\text{NB}}(r) = \begin{cases} V_{\text{LJ}}(r) - V_{\text{shift}}, & r < r_c, \\ 0, & \text{otherwise.} \end{cases} \quad (3.2)$$

The elastic bond between two neighboring monomers is modeled by a potential which combines a Lennard-Jones potential and the finitely extensible nonlinear elastic (FENE) potential:

$$V_{\text{B}}(r) = V_{\text{FENE}} + V_{\text{LJ}}(r) - V_{\text{shift}}, \quad (3.3)$$

where the same parameter values of $V_{\text{LJ}}(r)$ are chosen as in the previously introduced Lennard-Jones potential (3.1) and the FENE potential is given as [61–63]:

$$V_{\text{FENE}} = -\frac{1}{2}KR^2 \ln \left[1 - \left(\frac{r - r_0}{R} \right)^2 \right]. \quad (3.4)$$

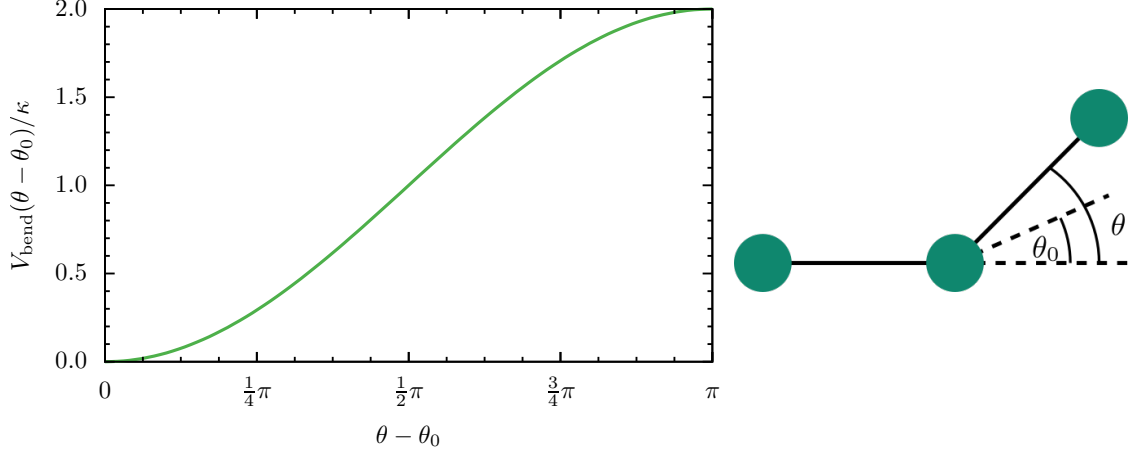


Figure 3.5: Plot of normalized bending potential $V_{\text{bend}}(\theta - \theta_0)/\kappa$ versus deviated bond angle $\theta - \theta_0$. The schematic representation of bond angles formed by two consecutive bonds is shown in the right figure. θ is actual bond angle and θ_0 is the actual reference angle.

Here FENE parameters are fixed to standard values $R = (3/7)r_0$ and $K = (98/5)\epsilon_{\text{LJ}}/r_0^2$ [64]. The bond length r is restricted to fluctuations within the range $[r_0 - R, r_0 + R]$. This more realistic potential leads to a much higher energetic penalty than a harmonic potential with the same K when close to the confinement boundary. Taylor expansion of $V_{\text{FENE}}(r)$ near equilibrium bond length r_0 results in this harmonic potential as the leading term. The difference is shown in Figure 3.4 (b). With these parameters, the minimum of V_{B} is located at r_0 .

For the description of the level of resistance to bending, an additional standard potential is introduced. Any deviation of bond angle θ from the reference angle θ_0 between neighboring bonds is subject to an energy penalty of the form:

$$V_{\text{bend}}(\theta) = \kappa [1 - \cos(\theta - \theta_0)]. \quad (3.5)$$

This energetic potential and the definition of bond angles are shown in Figure 3.5. The parameter $\kappa \geq 0$ controls the stiffness of the polymer chain. For $\kappa = 0$, the model describes flexible polymers. Regarding the choice of reference angle θ_0 , it depends on the specific model and the context. For example, there is a specific non-zero value used for the study of helical polymers [65–68]. However,

in this study, we chose $\theta_0 = 0$ for simplicity, which means any deviation from the straight chain results in an energetic penalty for $\kappa > 0$.

Finally, a conformation of a polymer chain with N monomers can be represented by $\mathbf{X} = (\mathbf{r}_1, \dots, \mathbf{r}_N)$, where \mathbf{r}_i is the position vector of the i th monomer. Then, the total energy of the polymer is given by

$$E(\mathbf{X}) = \sum_{i>j+1} V_{\text{NB}}(r_{i,j}) + \sum_i V_{\text{B}}(r_{i,i+1}) + \sum_l V_{\text{bend}}(\theta_l), \quad (3.6)$$

where $r_{i,j} = |\mathbf{r}_i - \mathbf{r}_j|$ is the distance between monomers i and j , and θ_l is the bond angle between two adjacent bonds.

In simulations and statistical analysis of the results, we set the basic scales to the following values: $k_{\text{B}} = 1$ (Boltzmann constant), the energy scale $\epsilon_{\text{LJ}} = 1$, and length scale $r_0 = 1$. The flexible chain with $N = 55$ monomers has already been studied extensively in the past [64, 69–75] and serves as the reference for the comparison with the semiflexible model. This chain length is sufficiently short to recognize finite-size effects but long enough for the polymer to form stable phases. The results we obtained from this study are have also been verified for chains with up to 100 monomers.

3.2 Monte Carlo Simulations

Markov Chains and Master Equations

Given the Hamiltonian of the system (3.6) as described in the previous section, it is tempting to directly generate all possible states of the system. In such an ideal scenario, the density of states $g(E)$ can be obtained, and thus all the macroscopic properties of the system can be calculated, e.g., the average of a quantity in canonical ensemble according to (2.35). However, even with modern computational power, exact enumeration is still limited to small lattice systems. The self-avoiding-

walk (SAW) model on square lattices is often used as the base for exact polymer studies [76–79]. Despite SAW’s simplicity, the total number of conformations already reaches $C_n \simeq 4.2 \times 10^{30}$ for $n = 71$ steps [80]. On the other hand, Monte Carlo simulations enable applications in the study of system properties in a more efficient way, and have been successfully employed in many statistical physics [8].

The main idea of Monte Carlo simulation is based on the identity of time and ensemble averages of a quantity

$$\overline{O} = \lim_{M \rightarrow \infty} \frac{1}{M} = \sum_{m=1}^M O \equiv \langle O \rangle = \int d^{3N} q \int d^{3N} p O(\mathbf{q}, \mathbf{p}) \rho(\mathbf{q}, \mathbf{p}). \quad (3.7)$$

Consequently, Markov Chain Monte Carlo (MCMC) simulation relies on generating finite series of states to estimate the average. In Markov theory, the transition probability from system state $\mathbf{X}_{t-\Delta\tau_0}$ to \mathbf{X}_t in a time step $\Delta\tau_0$ at time t is independent of the previous history of states [8, 43, 81],

$$t(\mathbf{X}_{t-\Delta\tau_0} \rightarrow \mathbf{X}_t; \Delta\tau_0) = P(\mathbf{X}_t | \mathbf{X}_{t-\Delta\tau_0}, \mathbf{X}_{t-2\Delta\tau_0} \dots, \mathbf{X}_{t=0}) = P(\mathbf{X}_t | \mathbf{X}_{t-\Delta\tau_0}), \quad (3.8)$$

where $P(\mathbf{X}_t | \mathbf{X}_{t-\Delta\tau_0})$ is the conditional probability, and $\sum_{\mathbf{X}_{t-\Delta\tau_0}} t(\mathbf{X}_{t-\Delta\tau_0} \rightarrow \mathbf{X}_t; \Delta\tau_0) = 1$. Moreover, the master equation describes the dynamics of the microstate probability $P(\mathbf{X})$ in Markov process,

$$\frac{\Delta P(\mathbf{X})}{\Delta\tau_0} = \sum_{\mathbf{X}'} [P(\mathbf{X}') t(\mathbf{X}' \rightarrow \mathbf{X}; \Delta\tau_0) - P(\mathbf{X}) t(\mathbf{X} \rightarrow \mathbf{X}'; \Delta\tau_0)], \quad (3.9)$$

which can be solved for the microstate transition probability under specific conditions. In equilibrium, the probability distribution $P(\mathbf{X})$ is stationary, which yields

$$\frac{\Delta P(\mathbf{X})}{\Delta\tau_0} = 0 = \sum_{\mathbf{X}'} [P(\mathbf{X}') t(\mathbf{X}' \rightarrow \mathbf{X}; \Delta\tau_0) - P(\mathbf{X}) t(\mathbf{X} \rightarrow \mathbf{X}'; \Delta\tau_0)] = 0. \quad (3.10)$$

In order to avoid cyclic solutions, we require the stricter detailed balance condition,

$$P(\mathbf{X}')t(\mathbf{X}' \rightarrow \mathbf{X}; \Delta\tau_0) - P(\mathbf{X})t(\mathbf{X} \rightarrow \mathbf{X}'; \Delta\tau_0) = 0. \quad (3.11)$$

The ratio of transition probabilities is then given by

$$\frac{t(\mathbf{X} \rightarrow \mathbf{X}'; \Delta\tau_0)}{t(\mathbf{X}' \rightarrow \mathbf{X}; \Delta\tau_0)} = \frac{P(\mathbf{X}')}{P(\mathbf{X})} \rightarrow \frac{t(\mathbf{X} \rightarrow \mathbf{X}')}{t(\mathbf{X}' \rightarrow \mathbf{X})} = \frac{P(\mathbf{X}')}{P(\mathbf{X})}, \quad (3.12)$$

The timescale $\Delta\tau_0$ is omitted since the right-hand side of the equations do not depend on time. For a more practical application, the transition probability can be factorized into two parts [43],

$$t(\mathbf{X} \rightarrow \mathbf{X}') = s(\mathbf{X} \rightarrow \mathbf{X}')a(\mathbf{X} \rightarrow \mathbf{X}'), \quad (3.13)$$

where $s(\mathbf{X} \rightarrow \mathbf{X}')$ is the selection probability for a specific update, and $a(\mathbf{X} \rightarrow \mathbf{X}')$ is the acceptance probability of that update. Therefore, according to (3.12),

$$\frac{a(\mathbf{X} \rightarrow \mathbf{X}')}{a(\mathbf{X}' \rightarrow \mathbf{X})} = \frac{s(\mathbf{X}' \rightarrow \mathbf{X})P(\mathbf{X}')}{s(\mathbf{X}' \rightarrow \mathbf{X})P(\mathbf{X})}. \quad (3.14)$$

Finally, by maximizing the larger acceptance probability to 1, the typical form of the acceptance probability is given as

$$a(\mathbf{X} \rightarrow \mathbf{X}') = \min \left[1, \frac{s(\mathbf{X}' \rightarrow \mathbf{X})P(\mathbf{X}')}{s(\mathbf{X}' \rightarrow \mathbf{X})P(\mathbf{X})} \right] = \min\{1, \sigma(\mathbf{X}, \mathbf{X}')\omega(\mathbf{X}, \mathbf{X}')\}. \quad (3.15)$$

Here, $\sigma(\mathbf{X}, \mathbf{X}')$ is defined as ratio of forward and backward selection probability

$$\sigma(\mathbf{X}, \mathbf{X}') = \frac{s(\mathbf{X}' \rightarrow \mathbf{X})}{s(\mathbf{X} \rightarrow \mathbf{X}')}, \quad (3.16)$$

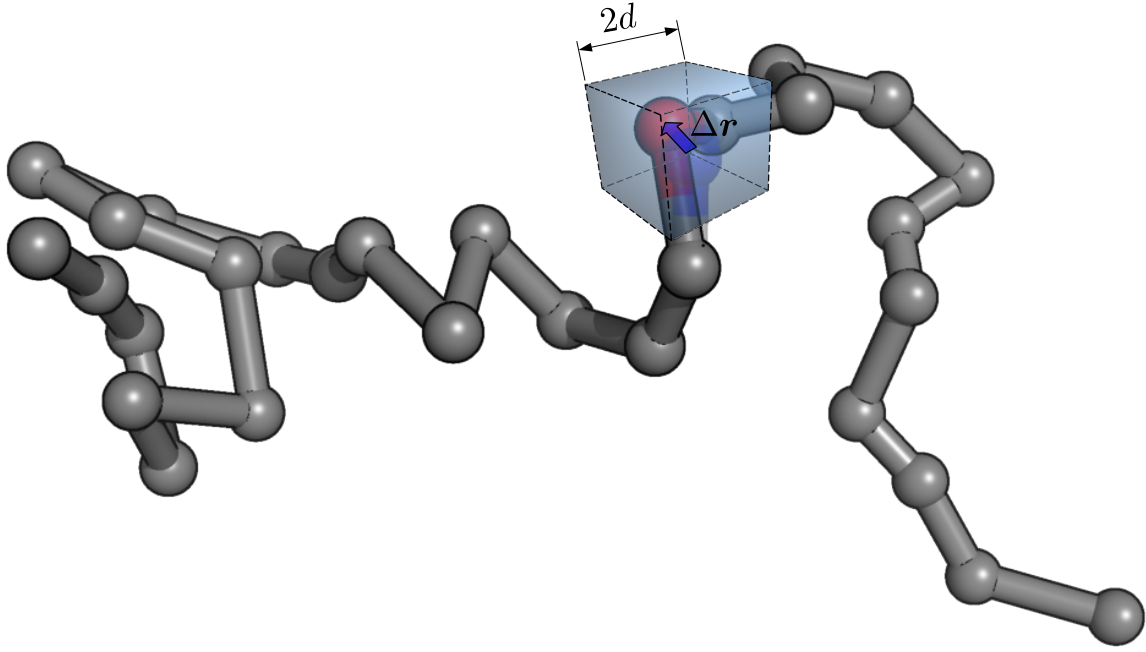


Figure 3.6: Illustration of the displacement update used in the polymer simulations. A randomly chosen monomer (blue) is moved to the new location (red) by a random vector $\Delta \mathbf{r} = (\Delta x, \Delta y, \Delta z)$. The available space for the monomer to update its position is shown as the cube that is centered around the originally chosen monomer (blue) with edge length d .

and $\omega(\mathbf{X}, \mathbf{X}')$ is defined as the ratio of microstate probabilities

$$\omega(\mathbf{X}, \mathbf{X}') = \frac{P(\mathbf{X}')}{P(\mathbf{X})}. \quad (3.17)$$

These two ratios are crucial for Monte Carlo simulations. The efficiency of Monte Carlo simulations depend on the proper choice of updates and the distribution of microstates.

3.2.1 Updates and Selection Probabilities

In actual simulations of semiflexible polymers, a series of states are generated as a Markov chain by attempting to update the structure in each step. For statistical analysis of results, the goal is to generate as many independent states as possible. To achieve this, other than running simulations

for a longer time, implementing more advanced local and global update moves not only helps reduce correlations of states but also helps overcome trapping in metastable states. However, more complicated updates are also associated with higher computational costs, and thus, reasonable combinations of low-cost and high-cost updates are needed. Moreover, optimized calculations for specific updates also improve the simulation efficiency.

One of the most basic local update moves for continuum polymer models is the displacement update. In such an update, a monomer is randomly chosen and randomly moved by a vector $\Delta\mathbf{r} = (\Delta x, \Delta y, \Delta z)$, where $\Delta x, \Delta y$ and Δz are independently chosen from random numbers that are uniformly distributed in the interval $[-d/2, d/2]$. Therefore, the possible updates of a monomer confined in a cube with an edge length d . The displacement update is illustrated in Fig. 3.6. The edge length d should be adjusted before taking any measurements in simulations to reach reasonable efficiency. For high temperature simulations with more extended conformations, if d is too small, most of the updates will be accepted and it will take much longer to scan the conformational space. Therefore, in this case, d should be increased but the length limit from FENE potential also needs to be considered. On the other side, most of the displacement updates will be rejected at low temperatures for large d , where a dramatic change in monomer position most likely results in short-range repulsion due to the dense conformations dominating is the solid phase. All considered, a practical adjustment [66] from current box edge length $d(T)$ at temperature T to a new edge length $d'(T)$ can be introduced as

$$d'(T) = d(T) + \alpha(\tilde{P}_d - P_d), \quad (3.18)$$

where α is the adjustment rate, \tilde{P}_d is the expected acceptance rate and P_d is the acceptance rate of displacement update with a certain amount of Monte sweeps (a Monte Carlo sweep is N update attempts, where N is the number of monomers in the chain). For this study, $\alpha = 0.004$, 100 sweeps are used to measure P_d , and $\tilde{P}_d = 0.5$, combinations of which would result in almost 50%

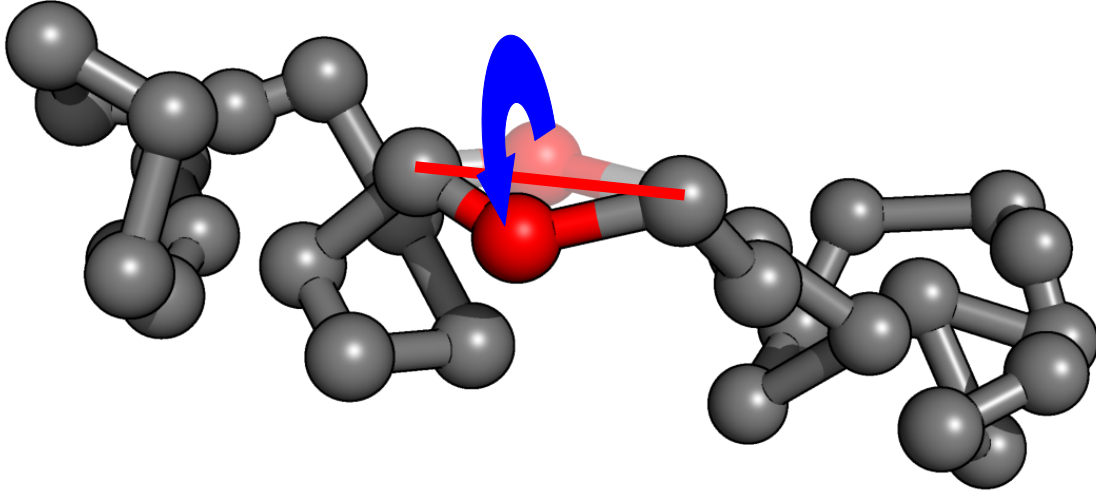


Figure 3.7: Illustration of the crankshaft update used in simulations. A randomly chosen monomer (red) is rotated by a random angle. The rotation axis formed by the two monomers bonded to the chosen monomer is shown as a red line.

acceptance rate. Forward and backward selection probabilities are the same for this type of update:

$$\sigma_d(\mathbf{X}, \mathbf{X}') = \frac{s_d(\mathbf{X}' \rightarrow \mathbf{X})}{s_d(\mathbf{X} \rightarrow \mathbf{X}')} = 1. \quad (3.19)$$

Besides, energy calculations can also be optimized for displacement updates. Only adjacent bonds are affected for bonded potentials and only non-bonded interactions between the chosen monomer and other monomers are affected, and also only neighboring bending angles are changed. Therefore, evaluating these energy changes is sufficient for the new state.

Another local update similar to the displacement update is the crankshaft rotation [82]. Similarly, a monomer is randomly chosen, and rotated a by a random angle ϕ within $[0, 2\pi]$ about a rotation axis, which is the line that connects the neighboring monomers of the chosen monomer. An illustration of the crankshaft update is shown in Fig. 3.7. Obviously, the selection probability

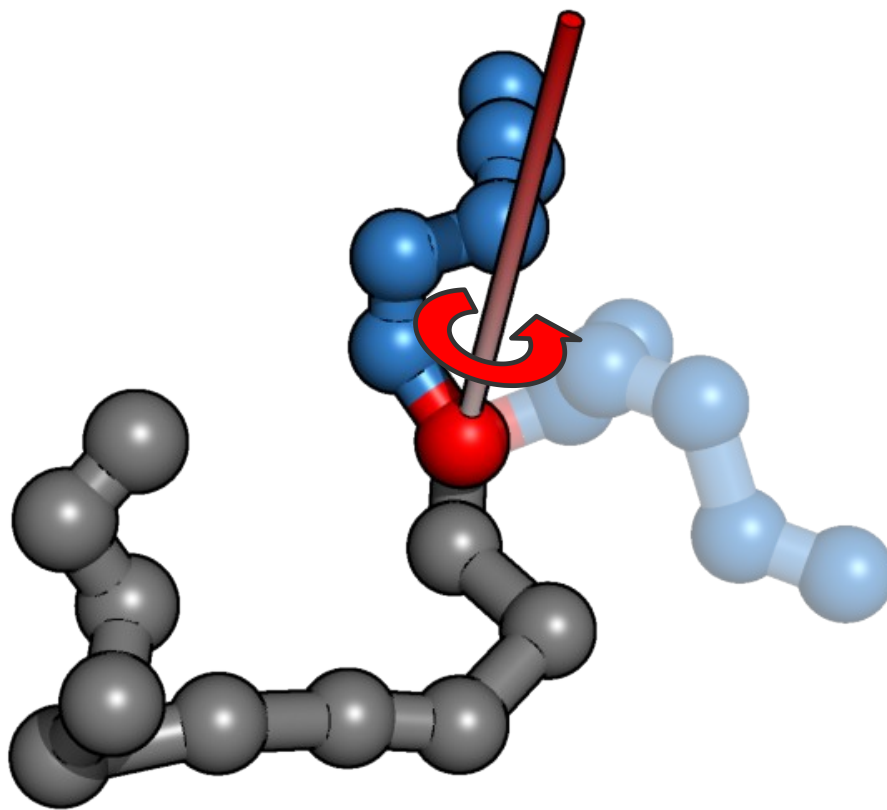


Figure 3.8: Illustration of the pivot update used in simulations. Randomly chosen monomer (red), and a random rotation axis generated. Then the rest of the chain (blue) is rotated by a random angle.

ratio for the update is also unity,

$$\sigma_c(\mathbf{X}, \mathbf{X}') = \frac{s_c(\mathbf{X}' \rightarrow \mathbf{X})}{s_c(\mathbf{X} \rightarrow \mathbf{X}')} = 1. \quad (3.20)$$

Energy calculations can also be optimized similarly to the displacement update but in a simpler way. In such an update, the bond length is not changed, and therefore the bonded potential is unaffected.

Other than the local updates introduced so far, global updates are also necessary for efficient simulations. The first global update we used is the pivot rotation [43], which usually attempts

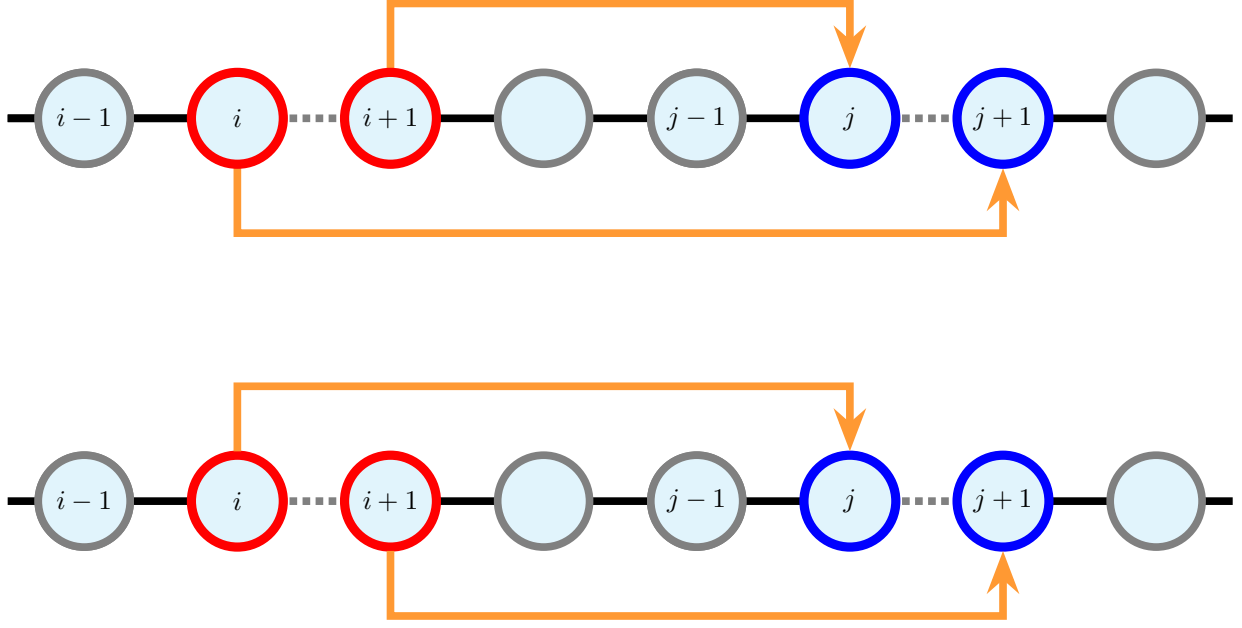


Figure 3.9: Illustration of the bond-exchange update based on indices. The monomer indexes are labeled and satisfy $j > i + 1$. (Upper part) Incorrect way of creating new two bonds, $(i + 1 \rightarrow j)$ and $(i \rightarrow j + 1)$, which breaks the chain into two parts. The broken bonds are marked by dashed lines. (Bottom part) The correct way of creating new two bonds, $(i \rightarrow j)$ and $(i + 1 \rightarrow j + 1)$.

to move more than one monomer in a step. First, similar to previous local updates, a non-end monomer is chosen. Second, a random rotation axis is generated at this monomer location. Finally, the rest of the chain starting from this chosen monomer is rotated by a random angle ϕ drawn from the interval $[0, 2\pi]$. Moreover, the probability of rotating the monomers from the new location back to the original position is the same, thus the ratio of selection probabilities still reads

$$\sigma_p(\mathbf{X}, \mathbf{X}') = \frac{s_p(\mathbf{X}' \rightarrow \mathbf{X})}{s_p(\mathbf{X} \rightarrow \mathbf{X}')} = 1. \quad (3.21)$$

Additionally, the energy calculations can also be optimized for this pivot rotational update, where bonded interactions are not altered, and only one bending angle is changed around the chosen monomer.

So far, all the introduced updates have a unitary selection probability ratio. Now we introduce two updates [83] that have different selection probabilities for forward and backward updates.

Considering dense conformations at low temperatures, pivot rotational updates are likely to be rejected in most cases with a high chance of collision in one of the monomers during the rotation process. Moreover, displacement updates and crank-shaft updates are inefficient when the polymer chain is trapped in some entangled compact structures. Therefore, rearranging bonds without moving monomers becomes an optimal solution. The first version of this type of update we used is the bond-exchange update. First, four close monomers $i, i + 1, j, j + 1$ with $j > i + 1$ are chosen, which form two neighboring bonds, $(i \rightarrow i + 1)$ and $(j \rightarrow j + 1)$. Then, these two bonds are broken, and new bonds are formed, $(i \rightarrow j)$ and $(i + 1 \rightarrow j + 1)$. The new bonds should also have bond length constraints from the FENE potential. One thing to be aware of in implementation is that creating a new bond $(i + 1 \rightarrow j)$ would result in a closed loop, which is demonstrated in Fig. 3.9. An example of the actual implementation is shown in Fig. 3.10.

Here we briefly talk about the selection probabilities. The selection probability for one direction can be factorized. First, the probability of a bond to be chosen for swapping is $1/N_{\text{bond}}(\mathbf{X})$, where $N_{\text{bond}}(\mathbf{X})$ is the number of total bonds. Then, the number of possible bonds that can be exchanged near the chosen bond is $n(\mathbf{X} \rightarrow \mathbf{X}')$, thus the probability of one of the nearest bonds to be chosen is $1/n(\mathbf{X} \rightarrow \mathbf{X}')$. Finally, the selection probability of the bond-exchange update from the state \mathbf{X} to a new state \mathbf{X}' is given by

$$s_b(\mathbf{X} \rightarrow \mathbf{X}') = \frac{1}{N_{\text{bond}}(\mathbf{X})n(\mathbf{X} \rightarrow \mathbf{X}')}.$$
 (3.22)

As a result, the ratio of forward and backward selection probabilities ratio becomes

$$\begin{aligned} \sigma_b(\mathbf{X}, \mathbf{X}') &= \frac{s_b(\mathbf{X}' \rightarrow \mathbf{X})}{s_b(\mathbf{X} \rightarrow \mathbf{X}')} \\ &= \frac{(N_{\text{bond}}(\mathbf{X})n(\mathbf{X} \rightarrow \mathbf{X}'))^{-1}}{(N_{\text{bond}}(\mathbf{X}')n(\mathbf{X}' \rightarrow \mathbf{X}))^{-1}} \\ &= \frac{n(\mathbf{X}' \rightarrow \mathbf{X})}{n(\mathbf{X} \rightarrow \mathbf{X}')}.$$
 (3.23)

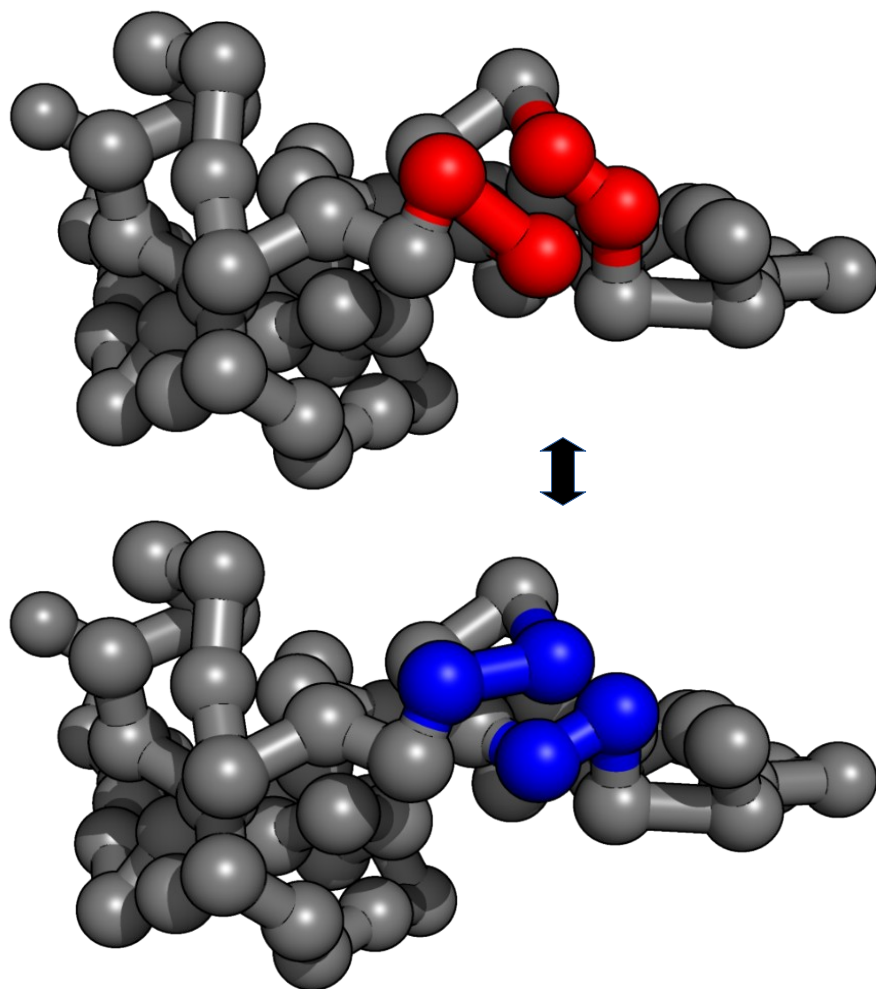


Figure 3.10: An example of the bond-exchange update used in simulations. From upper conformation to lower conformation, two nearby bonds (red) are chosen, and they are broken. Then two new bonds (blue) are formed without creating a discontinued loop, which is illustrated in Fig.3.9.

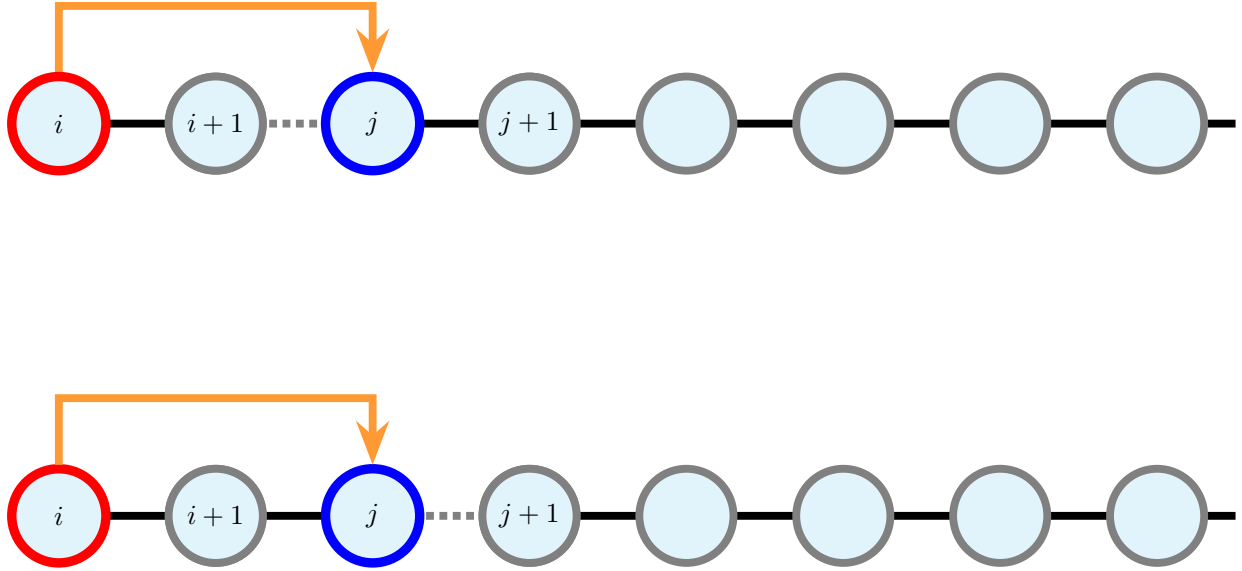


Figure 3.11: Sketch of the end-bond-exchange update based on monomer indices. The monomer indexes are labeled and satisfy $j > i + 1$. If the other end's monomer is chosen, reversing the full indices will recover this order due to symmetry. (Upper part) The correct way of creating a new bond between the end monomer (red) and a chosen nearby monomer (blue), where the bond between the blue monomer j and $j - 1$ are broken (red cross). (Bottom part) Breaking the bond ($j \rightarrow j + 1$) creates a closed loop and thus breaks the continuity of the chain.

The number of available bonds for the exchange is usually not the same for forward and backward selections, which leads to $\sigma_b(\mathbf{X}, \mathbf{X}') \neq 1$. The number of available bonds for each direction must be evaluated separately for every bond-exchange update.

Due to requirements of bond-exchange updates, the end monomers are always excluded. Therefore, the second version of the bond-exchange update is the end-bond exchange update. Compared to the bond-exchange update, the end-bond exchange update only involves one bond. More specifically, an end monomer is chosen to create a new bond between nearby nonbonded monomers. As a consequence, one of the nearby monomer's bonds is broken. Similarly, the selection probability of end-bond-exchange update from state \mathbf{X} to new state \mathbf{X}' can be factorized. The probability of one end monomer be chosen is $1/2$, and the number of possible bonds that can be connected nearby is

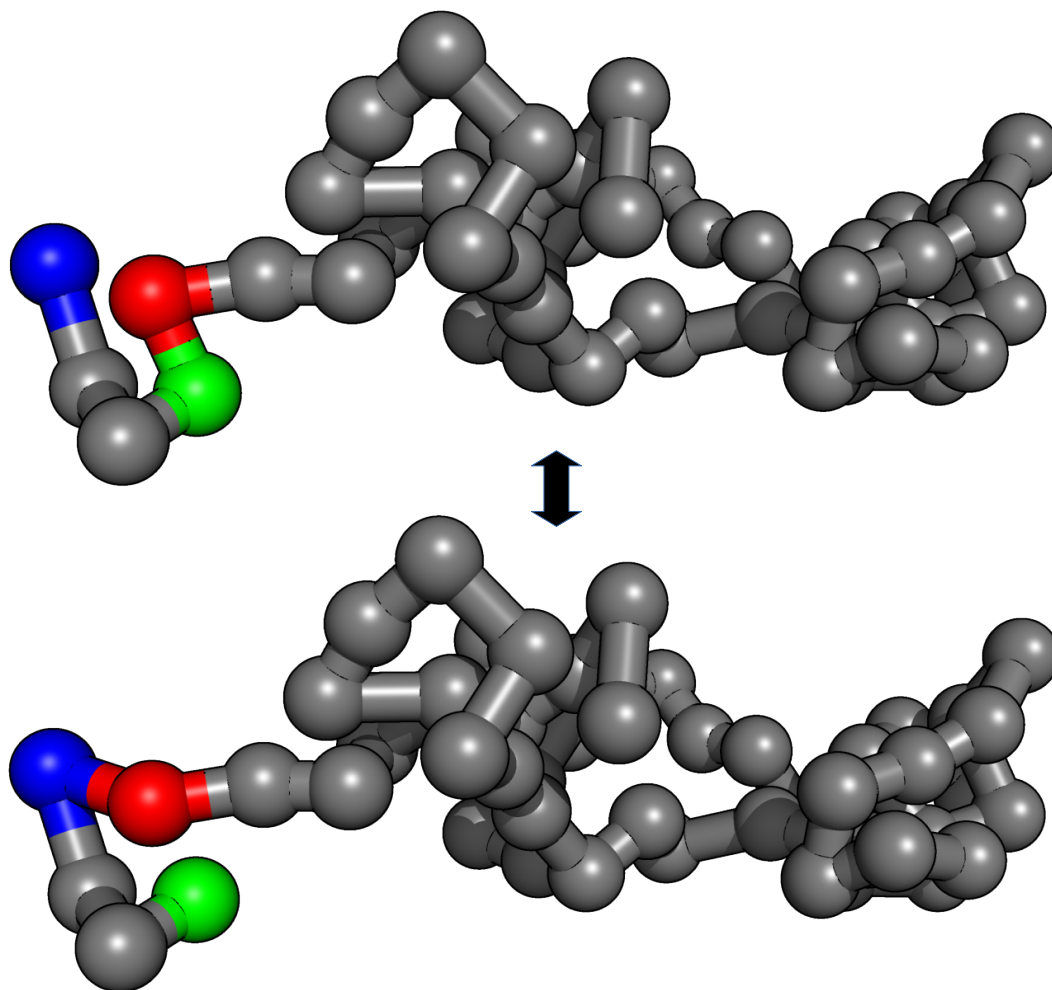


Figure 3.12: An example of the bond-exchange update used in simulations. From upper conformation to lower conformation, an end monomer is randomly chosen (blue), and then a nearby monomer (red) is selected. A bond between these two monomers is created, and the bond between the selected monomer (red) and the neighboring monomer (green) is broken. Consequently, the neighboring monomer (green) becomes the new end monomer. It can also be seen from these conformations that the end monomer (blue) of the upper conformation has only one possible monomer (red) to connect. However, for the lower conformation, the end monomer (green) has more than one available monomer to connect.

$n(\mathbf{X} \rightarrow \mathbf{X}')$. Similarly, the selection probability of end-bond-exchange is

$$s_e(\mathbf{X} \rightarrow \mathbf{X}') = \frac{1}{2n(\mathbf{X} \rightarrow \mathbf{X}')}, \quad (3.24)$$

and thus the selection probability ratio for the end-bond-exchange update is given by

$$\begin{aligned} \sigma_e(\mathbf{X}, \mathbf{X}') &= \frac{s_e(\mathbf{X}' \rightarrow \mathbf{X})}{s_e(\mathbf{X} \rightarrow \mathbf{X}')} \\ &= \frac{(2n(\mathbf{X} \rightarrow \mathbf{X}'))^{-1}}{(2n(\mathbf{X}' \rightarrow \mathbf{X}))^{-1}} \\ &= \frac{n(\mathbf{X}' \rightarrow \mathbf{X})}{n(\mathbf{X} \rightarrow \mathbf{X}')} . \end{aligned} \quad (3.25)$$

Similar to the bond-exchange update, the available bonds to form in forward and backward updates are usually different. The number of available bonds need to be calculated before and after performing the update. There are two bonds connected to the monomer that is going to be connected to the end monomer. It should be the bond between the monomer and the end monomer. Otherwise, a closed loop will be formed. This problem is illustrated in Fig. 3.11. What's more, an example is shown in Fig. 3.12, where an uneven number of possible bonds for forward and backward selection is chosen.

It is also worth mentioning again that the FENE bond length limit should always be considered for bond exchange updates, and monomer reindexing should be also performed after each bond-exchange update. Besides, energy calculations can also be optimized. The LJ interactions are not affected in both types of updates, and only relative bonds and bending angles are affected.

To summarize, we used various Monte Carlo update moves that are particularly useful for our model simulations and discussed selection probabilities. Particular features of actual implementations were noted. These updates have been sufficient for our simulations. Other types of updates such as spherical updates [84], bridging updates [85], dimer flip [86, 87] have also been used in the

past, but were not employed in our studies. More discussions about different updates can be found in [88].

3.2.2 Microstate Probabilities

In the previous section, we focused on selection probabilities that are contained in the acceptance probability (3.15) for Monte Carlo simulations. In this section, we will focus on the other part in Eq. (3.15), the transition possibility given by the microstate probabilities ratio (3.17).

Metropolis Algorithm

Because of its simplicity, the simulation algorithm used most in Monte Carlo simulations is the famous Metropolis algorithm [89]. In this method, the system is simulated in a heat bath temperature. The transition probability is

$$\begin{aligned}
 \omega(\mathbf{X}, \mathbf{X}') &= \frac{P(\mathbf{X}')}{P(\mathbf{X})} \\
 &= \frac{e^{-\beta_{\text{can}} E(\mathbf{X}') / Z_{\text{can}}}}{e^{-\beta_{\text{can}} E(\mathbf{X}) / Z_{\text{can}}}} \\
 &= e^{-\beta_{\text{can}} (E(\mathbf{X}') - E(\mathbf{X}))} \\
 &= e^{-\beta_{\text{can}} \Delta E}
 \end{aligned} \tag{3.26}$$

where Z_{can} is the canonical partition function for temperature T_{can} , $\beta_{\text{can}} = 1/k_{\text{B}} T_{\text{can}}$ and $\Delta E = E(\mathbf{X}') - E(\mathbf{X})$ is the total energy difference between proposed state \mathbf{X}' and current state \mathbf{X} . Combing the selection probabilities of different updates, the acceptance probability for this algorithm is then given as

$$a(\mathbf{X} \rightarrow \mathbf{X}') = \min \left[1, \sigma(\mathbf{X}, \mathbf{X}') e^{-\beta_{\text{can}} (E(\mathbf{X}') - E(\mathbf{X}))} \right]. \tag{3.27}$$

If the forward and backward selection probability ratio is $\sigma(\mathbf{X}, \mathbf{X}') = 1$, the Metropolis acceptance criteria (3.27) reduces to the most commonly used form

$$a(\mathbf{X} \rightarrow \mathbf{X}') = \min(1, e^{-\beta_{\text{can}} \Delta E}). \quad (3.28)$$

In the actual implementation, a random number r is chosen from a uniform distribution interval $[0, 1)$, and the update is accepted if $r \leq a$. Due to high cost and low efficiency of hardware random number generators (HRNG), algorithmic/software pseudo-random number generators (RNGs) are mostly used in simulations [8]. However, algorithmic/software RNGs possess finite periods and properties should be tested carefully before actual implementation [90–93]. In all simulations for our study, we used a 64-bit variant of RANMAR [94, 95] with very long period ($\approx 10^{61}$).

Replica-exchange Monte Carlo

The Metropolis algorithm is not particularly efficient in most cases. At low temperatures, the system can be trapped in low energy states due to small acceptance probability (if $\Delta E > 0$, and $\beta \rightarrow +\infty : e^{-\beta \Delta E} \rightarrow 0$). Besides, it suffers from critical slowing down for second-order transitions and an entropically suppressed energetic region at first-order transitions. Therefore, we mainly employed the type of generalized ensemble Monte Carlo method called replica-exchange Monte Carlo (parallel tempering) [96–101] for this study, which takes advantage of modern highly parallelized computational environments. Besides, in contrast to simulating the system at a fixed low temperature as is done in Metropolis sampling, parallel tempering has also been shown to reach equilibrium at low temperatures faster in simulations [102–106].

For clarity, all temperatures refer to canonical heat bath temperatures in this section. In the parallel tempering, replicas of the system are simulated at different inverse temperatures $\beta_k \in [\beta_{\min}, \beta_{\max}]$, with $k = 1, 2, \dots, K$, where K is the total number of temperature threads. One obvious advantage of this algorithm is that it can simulate the system at different temperatures simultaneously. At each temperature, Metropolis sampling is performed. Then, after a certain

amount of Monte Carlo sweeps, the replicas are swapped based on exchange probabilities. The selection probabilities are assumed to be the same for forward and backward exchanges, so only the transition probabilities are considered for replica exchange.

Suppose we have a replica with state \mathbf{X} at inverse temperature β_i , and an exchange is proposed with a replica in state \mathbf{X}' at neighboring inverse temperature β_j . The microstate probability ratio is then calculated using conditional probabilities:

$$\begin{aligned}
\omega(\mathbf{X} \leftrightarrow \mathbf{X}'; \beta_i, \beta_j) &= \frac{P(\mathbf{X}; \beta_j)P(\mathbf{X}'; \beta_i)}{P(\mathbf{X}; \beta_i)P(\mathbf{X}'; \beta_j)} \\
&= \frac{(e^{-\beta_j E(\mathbf{X})}/Z_{\text{can}}(\beta_j))(e^{-\beta_i E(\mathbf{X}')}/Z_{\text{can}}(\beta_i))}{(e^{-\beta_i E(\mathbf{X})}/Z_{\text{can}}(\beta_i))(e^{-\beta_j E(\mathbf{X}')}/Z_{\text{can}}(\beta_j))} \\
&= \frac{(e^{-\beta_j E(\mathbf{X})}e^{-\beta_i E(\mathbf{X}')})/(Z_{\text{PT}}(\beta_i, \beta_j))}{(e^{-\beta_i E(\mathbf{X})}e^{-\beta_j E(\mathbf{X}')})/(Z_{\text{PT}}(\beta_i, \beta_j))} \\
&= \frac{e^{-\beta_j E(\mathbf{X})}e^{-\beta_i E(\mathbf{X}')}}{e^{-\beta_i E(\mathbf{X})}e^{-\beta_j E(\mathbf{X}')}} \\
&= e^{-\beta_j E(\mathbf{X}) - \beta_i E(\mathbf{X}') + \beta_i E(\mathbf{X}) + \beta_j E(\mathbf{X}')} \\
&= e^{(\beta_i - \beta_j)(E(\mathbf{X}) - E(\mathbf{X}'))} \\
&= e^{\Delta\beta\Delta E},
\end{aligned} \tag{3.29}$$

where $Z_{\text{PT}}(\beta_i, \beta_j) = Z_{\text{can}}(\beta_i)Z_{\text{can}}(\beta_j)$ is the partition function of the generalized ensemble of these two temperatures. Consequently, the overall partition function of the generalized ensemble of all temperatures is given by

$$Z_{PT}(\beta_1, \dots, \beta_K) = \prod_{i=1}^K Z_{\text{can}}(\beta_i). \tag{3.30}$$

Finally, the exchange probability is given by

$$a(\mathbf{X} \leftrightarrow \mathbf{X}'; \beta_i, \beta_j) = \min(1, e^{\Delta\beta\Delta E}). \tag{3.31}$$

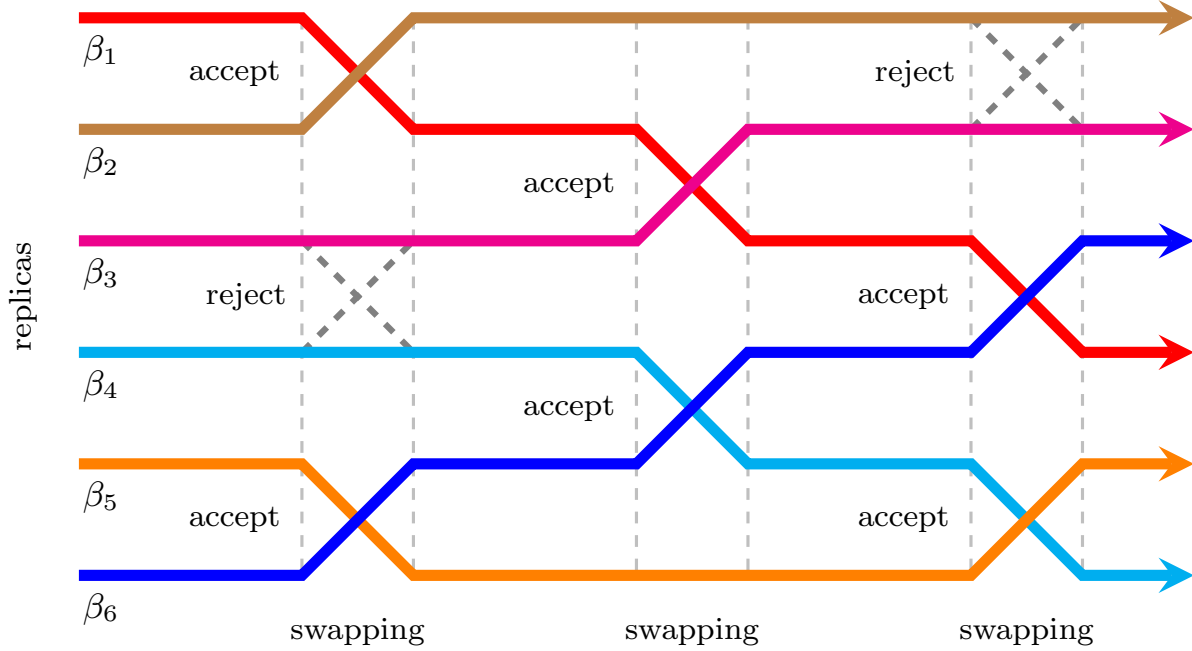


Figure 3.13: Schematic representation of parallel tempering swaps between adjacent replicas for an example with 6 different inverse temperatures β . In between the swaps, Metropolis Monte Carlo sweeps are performed. The swaps are proposed between either higher temperature threads or lower temperature threads periodically

In actual simulations, the exchange is proposed between the neighboring higher or lower temperature threads periodically as illustrated in Fig. 3.13.

Although the implementation of parallel tempering seems relatively simple, the selection of proper temperature sets is still the major obstacle. On the one hand, if the temperatures are too far apart, the energy difference ΔE between replicas will also typically be larger, which results from an overall lower exchange rate according to exchange probability (3.31), $(\Delta\beta\Delta E \rightarrow -\infty)$. On the other hand, for the same number of simulation threads, if the temperatures are too close, only a smaller energy range can be covered. As a result, it takes more time for temperature threads to synchronize (in practice, all threads wait for the slowest thread to finish the exchange attempt and then start the next round of in-thread Metropolis sampling), and the overall efficiency of the simulation reduces. Therefore, finding the proper temperature set has been an important topic in recent studies [107–113]. Among these methods, the feedback optimized method [110] provides a

quite good dynamic optimization of temperature threads. However, in the actual implementation of this method it takes considerable simulation time to generate enough exchanges for optimization. Therefore, with practicality considered, we found the combination of the geometric and the energy methods [109] provides reasonable temperature sets for our study, and it is easier to implement.

In the geometric method, the maximum inverse temperature β_{\max} and the minimum inverse temperature β_{\min} are fixed first. Then, the number of total threads M is decided. Finally, the inverse temperature β_i in thread i is decided by the geometric progression

$$\beta_i = \beta_{\min} R^{i-1}, \quad (3.32)$$

where $R = (\beta_{\max}/\beta_{\min})^{1/(M-1)}$. This method is most commonly used in parallel tempering due to its simplicity. However, as illustrated in Fig. 3.14, this method would not result in a good distribution of histograms, and it gets worse when a first-order transition is involved. If R is small, we get a reasonable overlap of high-temperature energy histograms but too dense low-energy histogram overlaps. If R is too large, we get a reasonable overlap of low-temperature energy histograms but too sparse high-energy histogram overlaps. Meanwhile, in both cases, the first-order transition region is not well covered, especially for large R . Therefore, further adjustments of temperatures are necessary for more efficient simulations.

In simulations, there is a quick run with a geometric temperature set with fixed temperature limits $\beta_{\min}, \beta_{\max}$ and number of threads M . As a result, we can get a roughly estimated function of average energy $\langle \hat{E} \rangle(\beta)$ as a monotonic function of inverse temperature β . Then a new temperature set is obtained by modifying temperatures such that when the estimated average energy is used in the exchange probability (3.31), the exchange probabilities are equal among all points,

$$P\left(\langle \hat{E} \rangle(\beta_{i-1}) \leftrightarrow \langle \hat{E} \rangle(\beta_i)\right) = P\left(\langle \hat{E} \rangle(\beta_i) \leftrightarrow \langle \hat{E} \rangle(\beta_{i+1})\right). \quad (3.33)$$

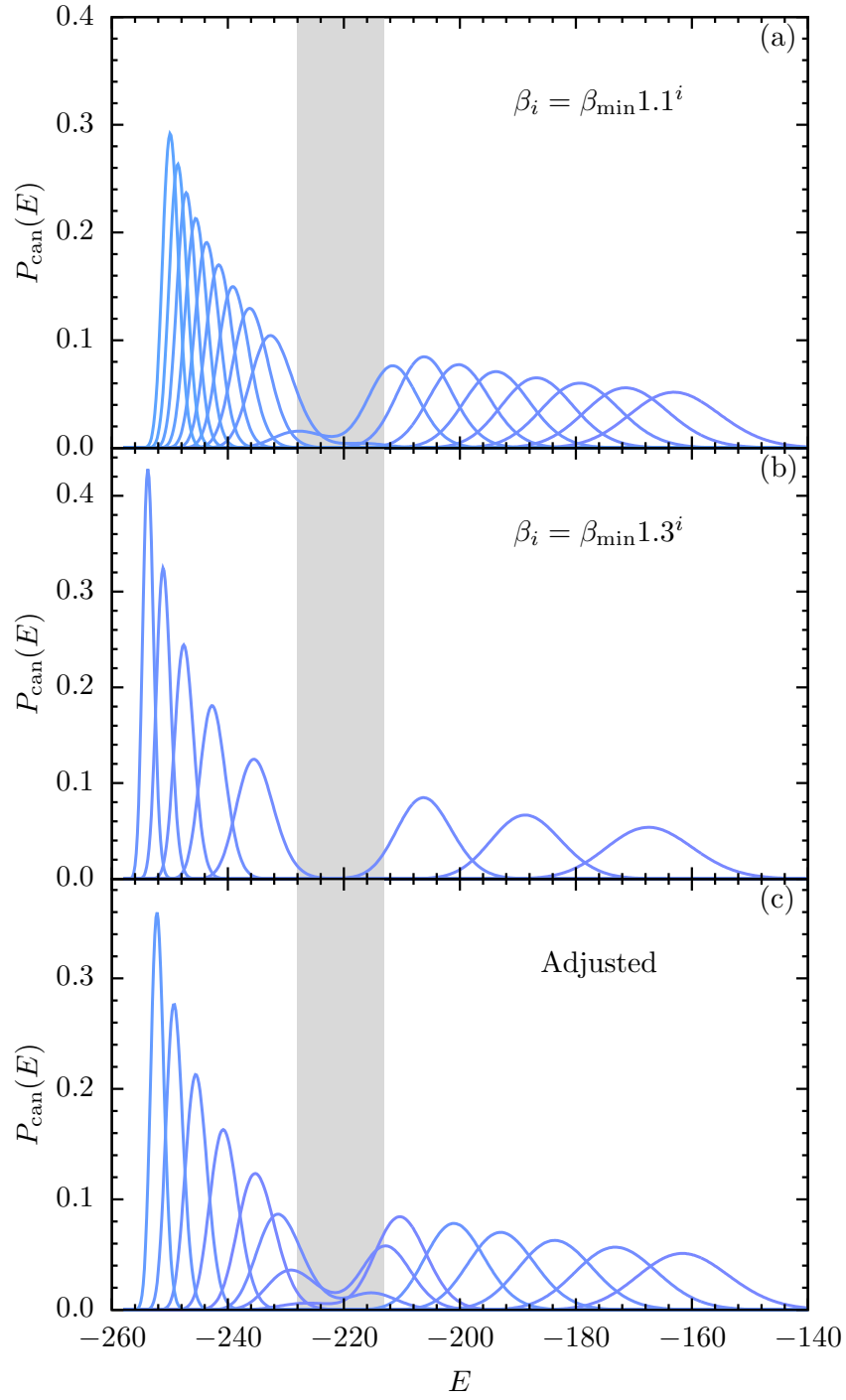


Figure 3.14: Energy histograms of the same system with different temperature sets. The first-order transition region is colored as gray. (a) Geometric setup of temperatures with $R = 1.1$. (b) Geometric setup of temperatures with $R = 1.3$. There is almost no overlap of histograms in the transition region. (c) Energy histogram if temperature sets are further adjusted.

Algorithm 1 A practical algorithm to adjust temperatures in PT simulations

- 1: Initialize an inverse temperature set $\beta_i = \beta_{\min} R^{i-1}$, $R = (\beta_{\max}/\beta_{\min})^{1/(M-1)}$, $1 \leq i \leq M$.
 - 2: Perform PT simulation and record estimated average energy $\langle \hat{E} \rangle$.
 - 3: Construct a monotonic function $\langle \hat{E} \rangle(\beta)$.
 - 4: Set a threshold for temperature difference ϵ .
 - while** $\sum |\beta'_i - \beta_i| > \epsilon$ **do**
 - 6: $\beta_i \leftarrow \beta'_i$.
 - 7: Find new inverse temperatures β'_i for even replicas using (3.33), while keeping odd replicas' inverse temperatures fixed.
 - 8: Find new inverse temperatures β'_i for odd replicas using (3.33), while keeping even replicas' inverse temperatures fixed.
 - end while**
 - 9: $\beta_i \leftarrow \beta'_i$.
-

The temperature adjustment can be done iteratively, and the whole process is summarized in Algorithm 1. After getting the adjusted inverse temperature set, new inverse temperatures can be added to the estimated transition region. In this simulation, using $R = 1.1$ for the initial average energy estimation worked relatively well, and $48 \leq M \leq 60$ temperature threads have been used for actual simulations.

Replica Exchange in 2D Parameter Space

Parallel tempering basically is simulating the system in the one-dimensional parameter space of inverse temperature β . In our semiflexible polymer model, there is another control parameter, the bending stiffness κ . The system total energy can be decoupled and the replica-exchange algorithm can be extended to the combined parameter space of inverse temperature and bending stiffness [16].

The system Hamiltonian (3.6) can be decoupled as following

$$\begin{aligned}
 E(\mathbf{X}) &= \underbrace{\sum_{i>j+1} V_{\text{NB}}(r_{i,j}) + \sum_i V_{\text{B}}(r_{i,i+1})}_{E_0} + \underbrace{\kappa \sum_{\theta_l} [1 - \cos(\theta_l)]}_{E_1} \\
 &= E_0 + \kappa E_1
 \end{aligned} \tag{3.34}$$

Consequently, the microstate probability ratio of replica \mathbf{X} with bending stiffness κ_i at inverse temperature β_i and replica \mathbf{X}' with bending stiffness κ_j at inverse temperature β_j can be derived as

$$\begin{aligned}
\omega(\mathbf{X} \leftrightarrow \mathbf{X}'; (\beta_i, \kappa_i), (\beta_j, \kappa_j)) &= \frac{P(\mathbf{X}; (\beta_j, \kappa_j))P(\mathbf{X}'; (\beta_i, \kappa_i))}{P(\mathbf{X}; (\beta_i, \kappa_i))P(\mathbf{X}'; (\beta_j, \kappa_j))} \\
&= \frac{(e^{-\beta_j(E_0 + \kappa_j E_1)} / Z_{\text{can}}(\beta_j, \kappa_j))(e^{-\beta_i(E'_0 + \kappa_i E'_1)} / Z_{\text{can}}(\beta_i, \kappa_i))}{(e^{-\beta_i(E_0 + \kappa_i E_1)} / Z_{\text{can}}(\beta_i, \kappa_i))(e^{-\beta_j(E'_0 + \kappa_j E'_1)} / Z_{\text{can}}(\beta_j, \kappa_j))} \\
&= \frac{(e^{-\beta_i(E'_0 + \kappa_i E'_1)} e^{-\beta_j(E_0 + \kappa_j E_1)}) / Z_{\text{RE}}((\beta_i, \kappa_i), (\beta_j, \kappa_j))}{(e^{-\beta_i(E_0 + \kappa_i E_1)} e^{-\beta_j(E'_0 + \kappa_j E'_1)}) / Z_{\text{RE}}((\beta_i, \kappa_i), (\beta_j, \kappa_j))} \\
&= e^{-\beta_i E'_0} e^{\beta_j E'_0} e^{-\beta_i \kappa_i E'_1} e^{\beta_j \kappa_j E'_1} e^{-\beta_j E_0} e^{\beta_i E_0} e^{-\beta_j \kappa_j E_1} e^{\beta_i \kappa_i E_1} \\
&= e^{E'_0(\beta_j - \beta_i)} e^{E'_1(\beta_j \kappa_j - \beta_i \kappa_i)} e^{E_0(\beta_i - \beta_j)} e^{E_1(\beta_i \kappa_i - \beta_j \kappa_j)} \\
&= e^{(\beta_j - \beta_i)(E'_0 - E_0)} e^{(\beta_j \kappa_j - \beta_i \kappa_i)(E'_1 - E_1)}. \\
&= e^{\Delta\beta\Delta E_0} e^{\Delta(\beta\kappa)\Delta E_1}, \tag{3.35}
\end{aligned}$$

where $Z_{\text{RE}}((\beta_i, \kappa_i), (\beta_j, \kappa_j)) = Z_{\text{can}}(\beta_i, \kappa_i)Z_{\text{can}}(\beta_j, \kappa_j)$ is the partition function of the generalized ensemble of these two parameters. Consequently, the overall partition function of the generalized ensemble of all threads is given by

$$Z_{RE} = \prod_{i=1} \prod_{j=1} Z_{\text{can}}(\beta_i, \kappa_j) \tag{3.36}$$

Finally, the exchange probability is given by

$$a(\mathbf{X} \leftrightarrow \mathbf{X}'; \beta_i, \beta_j) = \min(1, e^{\Delta\beta\Delta E_0} e^{\Delta(\beta\kappa)\Delta E_1}). \tag{3.37}$$

As expected, if κ values are identical, this extended exchange acceptance probability (3.37) reduces to the parallel tempering exchange probability (3.31). Moreover, this method can be extended to higher dimensional parameter space if the total energies can be decoupled with respect to more parameters.

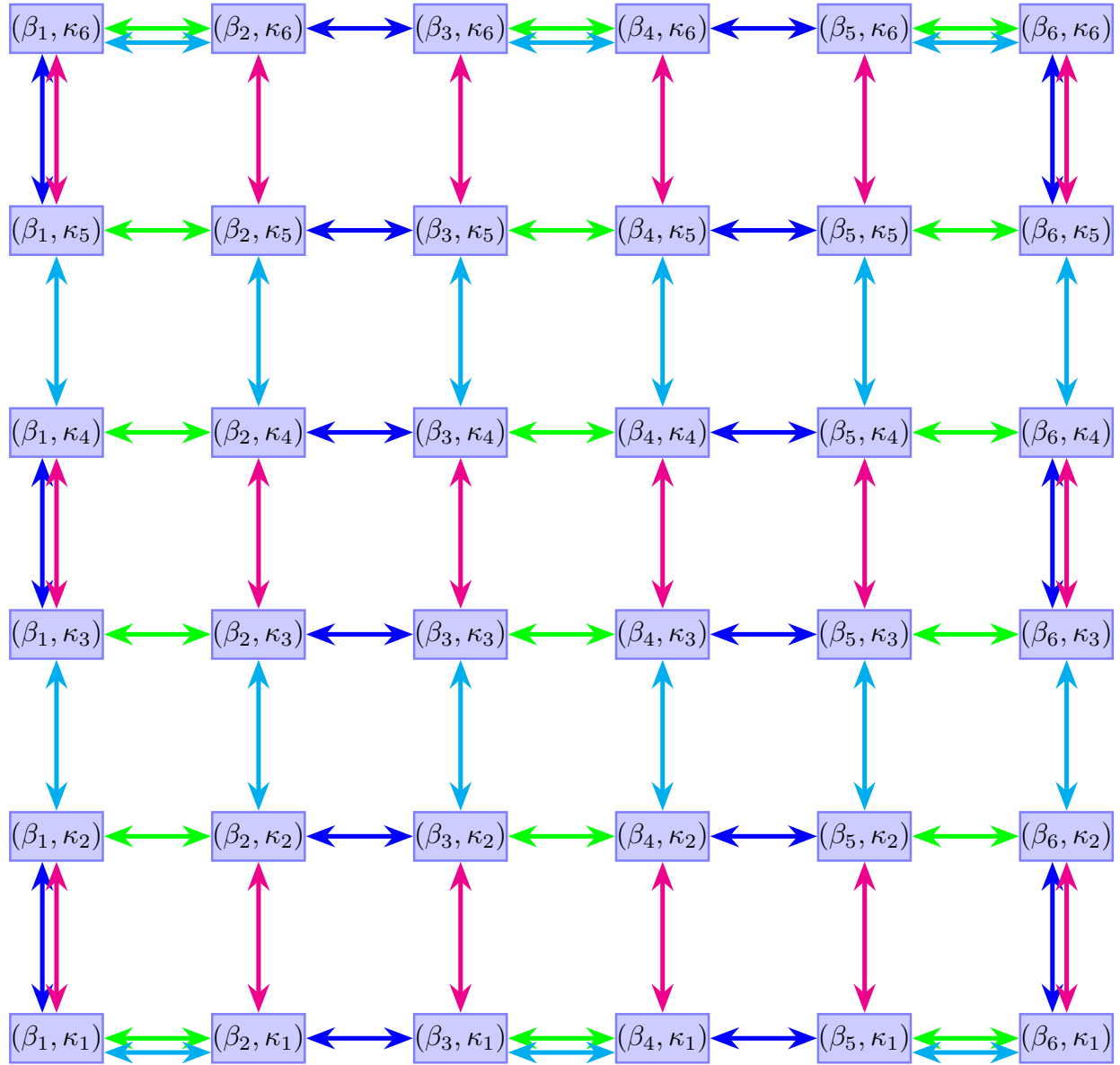


Figure 3.15: Illustration of an extended replica exchange Monte Carlo simulation in a combined parameter space of inverse temperature β and bending stiffness κ with the size of 6×6 . Each node (i, j) represents a simulation thread with a parameter combination of (β_i, κ_j) . In total, 4 different types of exchange directions are colored differently. The exchange directions are determined randomly with equal probabilities. The overlapping of exchange directions for corner nodes is conservation of flows.

As illustrated in Fig. 3.15, there are 4 directions of exchanges in the two-dimensional parameter space. The nodes at corners have overlapping exchange directions follow conservation of flows. In actual simulations, the exchange direction is determined randomly with equal probability after 1500-300 Monte Carlo sweeps.

3.2.3 Other Monte Carlo Simulation Methods

Other than the previously introduced replica exchange Monte Carlo methods, multiple Monte Carlo Methods are used to identify lowest-energy conformations. The results are compared and the best estimates of putative ground-state conformations are obtained. In the following, we briefly review the methods that have been used in this study.

Non-flat Distribution Wang-Landau Simulation

The Wang-Landau method [114] has been used in many studies due to its simplicity and the advantage of the efficient sampling of systems with first-order transition barriers. It samples the system according to an estimated inverse density of states $\hat{g}(E)$. As the simulation covers the entire energy range, the method is also commonly used as a ground-state search engine, as the system is pushed towards low entropy regions. In this method, updates of microstates are accepted with the probability:

$$P_{\text{WL}}(\mathbf{X} \rightarrow \mathbf{X}') = \min \left(\frac{\hat{g}(E(\mathbf{X}))}{\hat{g}(E(\mathbf{X}'))}, 1 \right). \quad (3.38)$$

In each Monte Carlo update, $\hat{g}(E)$ is updated with a modification factor $f(> 1)$: $\hat{g}(E) \rightarrow f \times \hat{g}(E)$. An iteration is finished if the energy histogram $H(E)$ is 'flat'. Then f is reduced: $f \rightarrow \sqrt{f}$. If $f \rightarrow 1$ within some limit (e.g., $\ln f \leq 10^{-8}$), the simulation is stopped. In the end, $\hat{g}(E)$ is expected to converge to the actual density of states $g(E)$.

To improve the efficiency, we used the modified nonflat-distribution Wang-Landau algorithm [115] with energy profile $p(E)$ along with multiple advanced updates. This leads to the

following acceptance probability for each update:

$$P'_{\text{WL}}(\mathbf{X} \rightarrow \mathbf{X}') = \min \left(\frac{\hat{g}(E(\mathbf{X}))p(E(\mathbf{X}'))}{\hat{g}(E(\mathbf{X}'))p(E(\mathbf{X}))} \sigma(\mathbf{X}, \mathbf{X}'), 1 \right), \quad (3.39)$$

where $\sigma(\mathbf{X}, \mathbf{X}') = s(\mathbf{X}' \rightarrow \mathbf{X}) / s(\mathbf{X} \rightarrow \mathbf{X}')$ is the ratio of forward and backward selection probabilities for specific updates. Combinations of displacement update with energy-dependent box size, crank-shaft move, pivot rotational update, bond-exchange update, and end-monomer exchange moves are used.

In our simulations, due to the vast range of volumes of the density of states usually covering many orders of magnitude, logarithmic representations are used in the acceptance probability (3.39), which is given by

$$P'_{\text{WL}}(\mathbf{X} \rightarrow \mathbf{X}') = \min \left(e^{(\ln \hat{g}(E(\mathbf{X})) - \ln \hat{g}(E(\mathbf{X}')) + \ln p(E(\mathbf{X}')) - \ln p(E(\mathbf{X})) + \ln \sigma(\mathbf{X}, \mathbf{X}'))}, 1 \right). \quad (3.40)$$

Simulated Annealing

Simulated annealing (SA) is a common algorithm [116] for locating a minimum of a complex function. The system is heated up to a high temperature and cooled down slowly, and Metropolis Monte Carlo sampling is performed at the current temperature. By repeating this cycle multiple times, the system may have come close to the global minimum at some point. At each temperature T_k , Metropolis updates are accepted according to the criterion

$$P_{\text{SA}}(\mathbf{X} \rightarrow \mathbf{X}'; T_k) = \min \left\{ \exp \left[-\frac{E(\mathbf{X}') - E(\mathbf{X})}{k_{\text{B}} T_k} \right] \sigma(\mathbf{X}, \mathbf{X}'), 1 \right\}. \quad (3.41)$$

We used an exponential cooling scheme for the temperature, $T_k = T_0 e^{-\alpha k}$, where T_0 is the initial temperature, α is cooling rate and k is the index of the current iteration. In order to improve efficiency, we implemented a parallelized version of this algorithm by distributing the cooling procedures to multiple simulation threads.

Energy Landscape Paving

The energy landscape paving method [117] has also been widely used as a Monte Carlo ground-state search algorithm. Generally, low-temperature Monte Carlo simulations are performed, but compared to the conventional Metropolis algorithm, the energy weight function $\omega(E, t)$ is time-dependent and modified dynamically. In our implementation, we used the cumulative energy histogram $H(E, t)$ as the time-dependent weight function

$$\omega(E, t) = e^{-\beta[E+H(E, t)]}. \quad (3.42)$$

The acceptance probability is given by

$$P_{\text{ELP}}(\mathbf{X} \rightarrow \mathbf{X}'; t) = \min \left(\frac{\omega(E(\mathbf{X}), t)}{\omega(E(\mathbf{X}'), t)} \sigma(\mathbf{X}, \mathbf{X}'), 1 \right). \quad (3.43)$$

The method periodically inclined to lower- or higher-energy regions. When the low-energy region is visited, the histogram counts increase, and thus the weight decreases. Therefore, the system prefers the high energy region as Metropolis sampling prefers larger weight region. Similarly, if the high energy region is visited more, the overall weight will be smaller than the low energy region. In consequence, the metropolis sampling will favor the low energy region again. As a result, the system travels back and forth between high-energy and low-energy regions. Similar to simulated annealing, the system is expected to get close to the lowest energy state during simulations. Moreover, this algorithm is self-adjusting, where the algorithm explores high and low-energy regions periodically, enabling it to overcome free-energy barriers.

3.3 Multiple-histogram Reweighting and Smoothing

In order to perform a microcanonical inflection-point analysis of the transition behavior, we not only need to perform sophisticated simulations as introduced in the previous sections, but also have to

estimate the density of states from the simulation data. By utilizing the canonical energy distribution function $P_{\text{can}}(E; \beta) \propto g(E)e^{-\beta E}$, the density of states can be obtained as $g(E) \propto P_{\text{can}}(E; \beta)e^{\beta E}$ by reweighting. The equilibrium energy histogram $h(E; \beta)$ obtained from Metropolis sampling at the inverse temperature β is indeed an estimate of the canonical energy distribution function $P_{\text{can}}(E; \beta)$. Therefore, the density of states can be estimated using the energy histogram, $\overline{g(E)} = h(E; \beta)e^{\beta E}$. However, due to low statistics in the tails of the histogram, using a single histogram only covers a narrow range of energies efficiently. Combining the histograms obtained at different inverse temperatures by employing the multi-histogram reweighting method [97, 118], which is also known as “weighted histogram analysis method” (WHAM), yields an improved estimator for the density of states that covers the entire energy range:

$$\widehat{g}(E) = \frac{\sum_{k=1}^K h(E; \beta_k)}{\sum_{k=1}^K \frac{M_k e^{-\beta_k E}}{Z_k}}. \quad (3.44)$$

Here M_k is the total number of Monte Carlo sweeps in thread k and Z_k is an estimator of the canonical partition function at the inverse temperature β_k :

$$Z_k = \sum_E \widehat{g}(E) e^{-\beta_k E} \Delta E, \quad (3.45)$$

where ΔE is the partitioned energy bin width in the simulation. By initializing all estimators of the canonical partition function, equations (3.44) and (3.45) are solved iteratively until reasonable convergence can be achieved. For this study, we stopped at the i th iteration if the following convergence condition is satisfied:

$$\sum_{k=1}^K \left| \frac{\ln Z_k^{(i)} - \ln Z_k^{(i-1)}}{\ln Z_k^{(i)}} \right| < 10^{-10}. \quad (3.46)$$

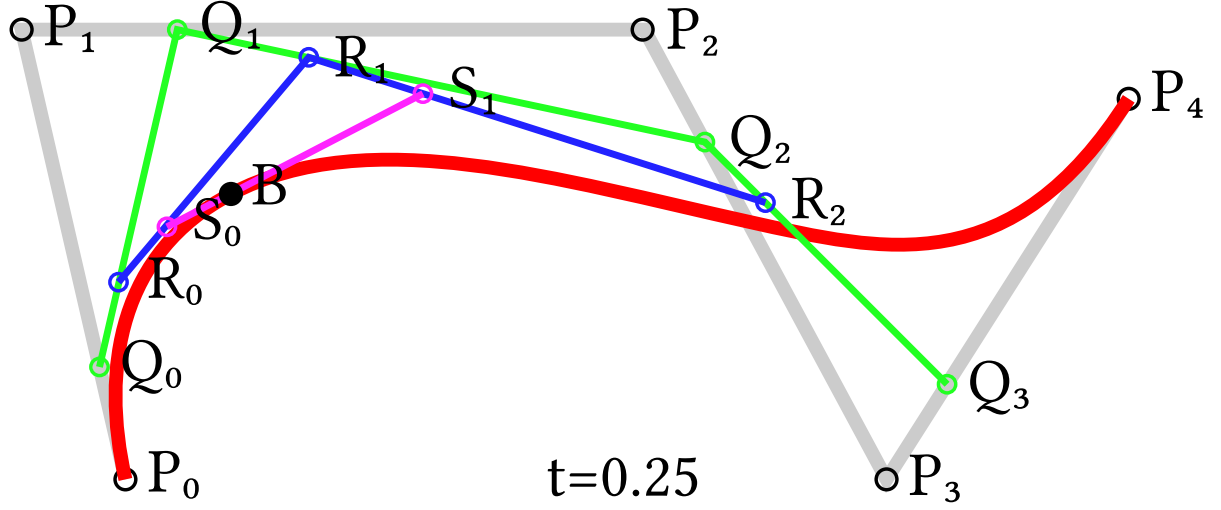


Figure 3.16: A fourth-order Bézier curve $B(t)$ constructed with five control points P_0, P_1, \dots, P_4 at $t = 0.25$. Intermediate points are defined as $Q_i(t) = P_i + t(P_{i+1} - P_i)$, $R_i(t) = Q_i + t(Q_{i+1} - Q_i)$, and $S_i(t) = R_i + t(R_{i+1} - R_i)$. Finally, the curve is constructed from $B_i(t) = S_i + t(S_{i+1} - S_i)$.

The density of states and the Boltzmann factor can be very large for the systems studied in this study. To avoid data overflow problems in the iterations, we used logarithmic summations [43] for the evaluation of equations (3.44) and (3.45) in each iteration.

3.3.1 Bézier Smoothing

For further analysis of the estimated density of states $g(E)$, we need to construct the entropy $S(E)$ as a smooth function and calculate the derivatives for the microcanonical inflection-point analysis. The entropy $S(E)$ is system-dependent and cannot be fitted analytically by polynomials or other functions. Another option is to employ data smoothing techniques, but most of the relative methods only smooth the original curve and provide only up to the first-order derivative. For the microcanonical inflection-point analysis method, we also need precise higher-order derivatives. Therefore, we used a technique called Bézier curve construction [119, 120]. Originally, the Bézier curve was developed to construct smooth curves for car design, but later has been used for constructing smooth n th order functions with $n + 1$ data points. This means derivatives up to n th order can be determined *analytically*. This is more than enough for our study, where we usually have

$n > 1000$ data points. Moreover, Bézier smoothing has also shown to be one of the best methods for reconstructing the original function with fewer fluctuations [121].

An n th degree Bézier curve of $n + 1$ control points $\mathbf{P}_0, \mathbf{P}_1, \dots, \mathbf{P}_n, \mathbf{P}_{n+1}$ is constructed by

$$\mathbf{B}(t) = \sum_{i=0}^n b_{i,n}(t) \mathbf{P}_i, \quad 0 \leq t \leq 1, \quad (3.47)$$

where the coefficients are known as Bernstein basis polynomials,

$$b_{i,n}(t) = \binom{n}{i} (1-t)^{n-i} t^i = \frac{n!}{i!(n-i)!} (1-t)^{n-i} t^i. \quad (3.48)$$

An example of constructing a fourth-order Bézier curve is shown in Fig. 3.16. The general formula for k th derivative of the Bézier curve with respect to t can be obtained by using the De Casteljau algorithm [122],

$$\mathbf{B}^{(k)}(t) = n(n-1)(n-2) \cdots (n-k+1) \sum_{i=0}^{n-k} b_{n-k,i}(t) \mathbf{D}_i^k, \quad (3.49)$$

where the first level difference is defined as $\mathbf{D}_i^1 = \mathbf{P}_{i+1} - \mathbf{P}_i$, and the k th level difference is calculated recursively,

$$\mathbf{D}_i^k = \mathbf{D}_{i+1}^{k-1} - \mathbf{D}_i^{k-1}, \quad 0 \leq i \leq n-k. \quad (3.50)$$

For two-dimensional data points $\mathbf{P}_i = (x_i, y_i)$, the k th parametric Bézier derivative (3.49) can be explicitly written as,

$$\mathbf{B}^{(k)}(t) = (x^{(k)}(t), y^{(k)}(t)) \quad (3.51)$$

However, the k th parametric Bézier derivative (3.49) is calculated for the parameter t , and thus extra transformations are needed for calculating the derivatives of y with respect to x . Therefore,

the first-order derivative is given by

$$\frac{dy}{dx} = \frac{\frac{dy}{dt}}{\frac{dx}{dt}} = \frac{y^{(1)}(t)}{x^{(1)}(t)}. \quad (3.52)$$

The second-order derivative then can be calculated further,

$$\begin{aligned} \frac{d^2y}{dx^2} &= \frac{d\left(\frac{dy}{dx}\right)}{dx} = \frac{d\left(\frac{dy}{dx}\right)}{dt} \frac{dt}{dx} = \frac{d\left(\frac{y^{(1)}(t)}{x^{(1)}(t)}\right)}{dt} \left(\frac{dx}{dt}\right)^{-1} \\ &= \frac{y^{(2)}(t)x^{(1)}(t) - x^{(2)}(t)y^{(1)}(t)}{x^{(1)}(t)^2} \frac{1}{x^{(1)}(t)} \\ &= \frac{x^{(1)}(t)y^{(2)}(t) - x^{(2)}(t)y^{(1)}(t)}{x^{(1)}(t)^3}. \end{aligned} \quad (3.53)$$

Similarly, we can obtain the third-order derivative as follows,

$$\begin{aligned} \frac{d^3y}{dx^3} &= \frac{d\left(\frac{d^2y}{dx^2}\right)}{dx} = \frac{d\left(\frac{d^2y}{dx^2}\right)}{dt} \frac{dt}{dx} = \frac{d\left(\frac{x^{(1)}(t)y^{(2)}(t) - x^{(2)}(t)y^{(1)}(t)}{(x^{(1)}(t))^3}\right)}{dt} \left(\frac{dx}{dt}\right)^{-1} \\ &= \frac{[x^{(2)}(t)y^{(2)}(t) + x^{(1)}(t)y^{(3)}(t) - x^{(3)}(t)y^{(1)}(t) - x^{(2)}(t)y^{(2)}(t)] x^{(1)}(t)^3}{x^{(1)}(t)^7} \\ &\quad - \frac{3x^{(1)}(t)^2 x^{(2)}(t) [x^{(1)}(t)y^{(2)}(t) - x^{(2)}(t)y^{(1)}(t)]}{x^{(1)}(t)^7} \\ &= \frac{x^{(1)}(t)^2 y^{(3)}(t) - x^{(1)}(t)x^{(3)}(t)y^{(1)}(t) + 3x^{(2)}(t)^2 y^{(1)}(t) - 3x^{(1)}(t)x^{(2)}(t)y^{(2)}(t)}{x^{(1)}(t)^5}. \end{aligned} \quad (3.54)$$

The higher-order derivatives can be calculated accordingly or can be obtained from the general explicit formulas of the n th derivative from Todorov [123], one of which is given by

$$\frac{d^n y}{dx^n} = \frac{1}{(x^{(1)}(t))^{n(n+1)/2}} \begin{vmatrix} \frac{d}{dt} \frac{x(t)}{1!} & \frac{d}{dt} \frac{x(t)^2}{2!} & \cdots & \frac{d}{dt} \frac{x(t)^{n-1}}{(n-1)!} & \frac{dy(t)}{dt} \\ \frac{d^2}{dt^2} \frac{x(t)}{1!} & \frac{d^2}{dt^2} \frac{x(t)^2}{2!} & \cdots & \frac{d^2}{dt^2} \frac{x(t)^{n-1}}{(n-1)!} & \frac{d^2 y(t)}{dt^2} \\ \vdots & \vdots & \ddots & \vdots & \vdots \\ \frac{d^n}{dt^n} \frac{x(t)}{1!} & \frac{d^n}{dt^n} \frac{x(t)^2}{2!} & \cdots & \frac{d^n}{dt^n} \frac{x(t)^{n-1}}{(n-1)!} & \frac{d^n y(t)}{dt^n} \end{vmatrix}. \quad (3.55)$$

A comparison of the Bézier curve and the results obtained by the commonly used Savitzky-Golay [125] smoothing method is shown in Fig. 3.17. The Bézier method smooths data better and provides a better first-order derivative. The latter method's performance can be improved with parameter tuning, whereas the Bézier approach is parameter-free.

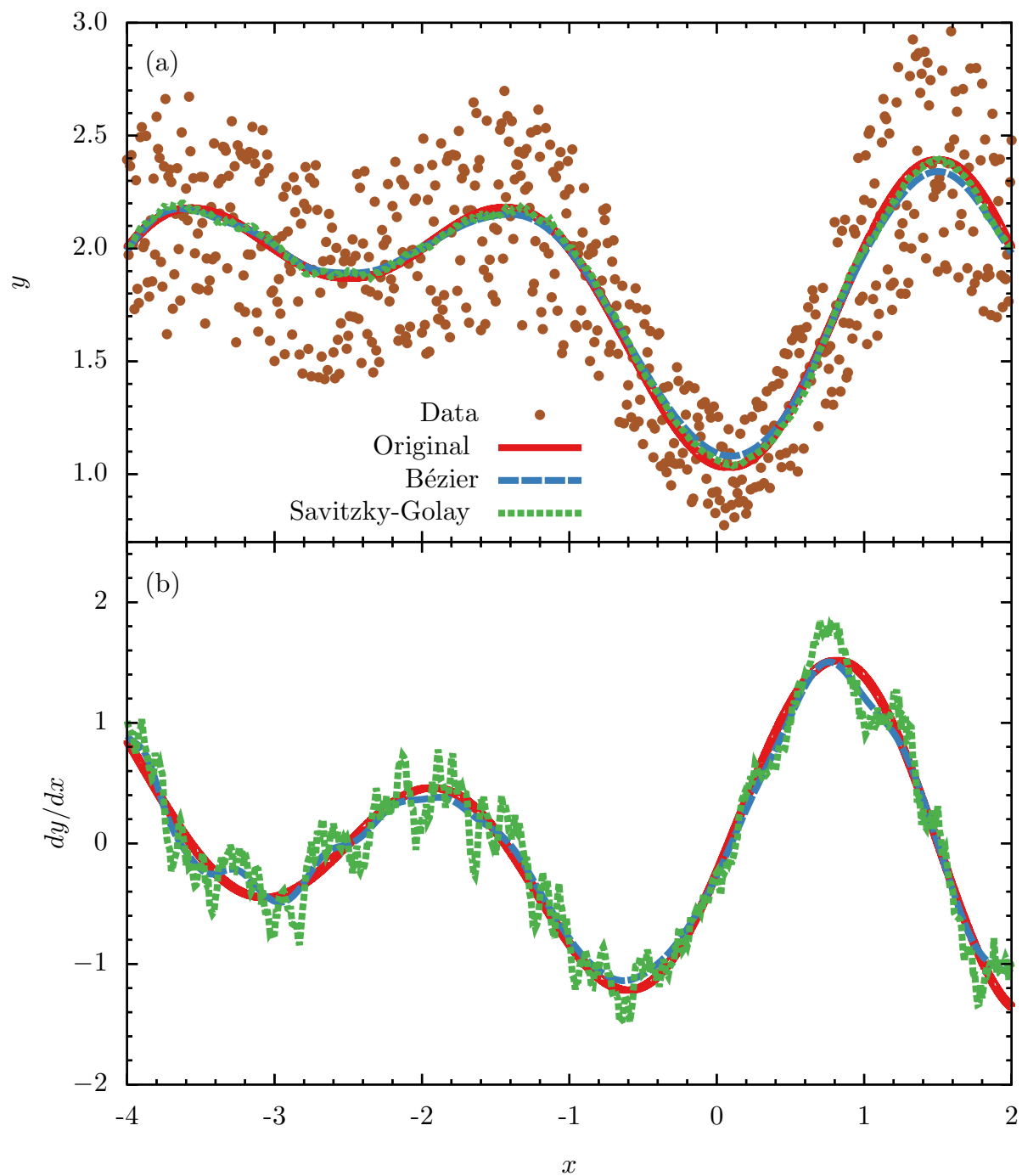


Figure 3.17: Comparison of two different smoothing methods on a noisy data set of a function. (a) The original function (solid redline) and noisy data points are generated by adding random noise to the original function. The blue dashed line is the smoothed line of the data points by our Bézier method. The green dotted line is the results of the Savitzky-Golay method [124], where the window size is set to 51 data points and the order of the polynomial is set to 3. (b) The first-order derivatives of the original function and the estimated first-order derivatives from the two smoothing methods.

CHAPTER 4

SIMULATION AND ANALYSIS OF A POLYMER SYSTEM

The model studied in this dissertation project, as described in Section 3.1, $\kappa = 0$ represents fully flexible elastic polymers, which have been studied extensively. Therefore, it serves as the reference for the comparison with the semiflexible model ($\kappa > 0$), and also as the testing ground for the newly developed Monte Carlo technique before using it for the semiflexible polymer model. In this chapter, we use this flexible polymer model to demonstrate the whole simulation and analysis process.

4.1 Parallel Tempering Temperature Set

In order to test the previously proposed algorithm for the temperature adjustment, we performed a parallel tempering simulation with 48 temperature threads using a geometric setup. The inverse heat bath temperature in the i th thread is initialized as

$$\beta_i^{\text{can}} = 0.2 \times 1.0868^{i-1}, \quad (4.1)$$

which generates a temperature set in the range $\beta_{\min}^{\text{can}} = 0.2$ and $\beta_{\max}^{\text{can}} = 10.0$. Then we estimated the average energy $\langle E \rangle(\beta)$ as a function of the inverse temperature β , which is plotted in Fig. 4.1 (a).

To examine the performance of this temperature setup, we measured the exchange rate of replicas from the simulation, and the results are shown in Fig. 4.1 (b). In the low-temperature region (large β_{can}), the exchange rate is frequent. However, it is obvious that at the first-order freezing transition point ($\beta_{\text{can}} \approx 3$), the exchange rate significantly decreases. Moreover, in the high-temperature region (small β_{can}), due to the large overlap of energy histograms, the exchange rate is much larger. Interestingly, if we plot the known transition points of this model and identify the corresponding typical structures in each phase, we observe that the phase transitions are also reflected by the change in the exchange rate. Near the random-coil to liquid-globular transition point ($\beta_{\text{can}} \approx 0.66$), the transition rate stops decreasing drastically and decreases at a slower rate in the liquid-globular phase compared to the random-coil phase. The transition rate is suppressed the most near the liquid-globular to solid-globular transition point ($\beta_{\text{can}} \approx 3$). This distribution of imbalanced exchange rates with relatively low values at some temperatures usually affects the simulation efficiency. Ideally, we expect a uniform distribution of the exchange rates, so we use the energy method described in the following to update the temperature set to better a better distribution of temperatures.

As mentioned in the previous chapter, after having estimated the average energy, we can use it to update the temperature set by a series of iterations. The expected exchange rate $\hat{\mathcal{R}}$ then can be estimated by using the average energy in the parallel tempering exchange probability

$$\hat{\mathcal{R}}(\langle E_{i-1} \rangle, \beta_{i-1}^{\text{can}} \leftrightarrow \langle E_i \rangle, \beta_i^{\text{can}}) = \exp \left((\beta_i^{\text{can}} - \beta_{i-1}^{\text{can}}) (\langle \hat{E} \rangle_i - \langle \hat{E} \rangle_{i-1}) \right). \quad (4.2)$$

In the actual update, the temperatures are split into odd and even orders, which are marked by two different colors in Fig. 4.1 (a). Then, while the odd-order temperature points are fixed, each even-order inverse temperature β_i^{can} is modified between two neighboring odd-number temperatures until the following expected uniform exchange rate condition is satisfied,

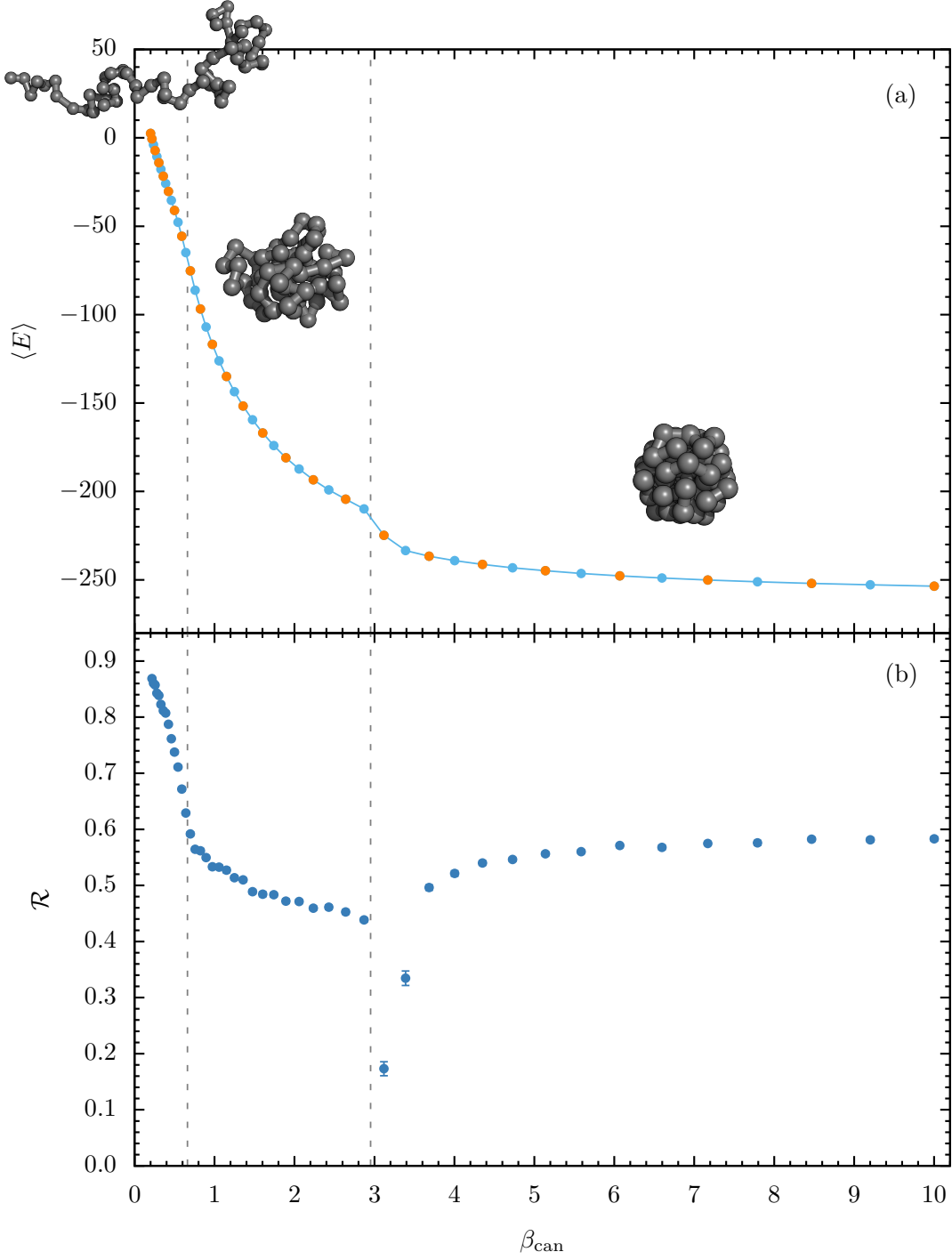


Figure 4.1: (a) Average energy $\langle E \rangle$ obtained from a parallel tempering Monte Carlo simulation with a geometric temperature setup for a flexible polymer with $N = 55$ monomers. Data points from even and odd temperature threads are colored differently. (b) Actual exchange acceptance rate \mathcal{R} between neighboring temperature threads from the same simulation. Both quantities are plotted as functions of the inverse heat bath temperature β_{can} . Structural phase transition points are indicated by dashed lines and corresponding dominant structures in each phase are shown.

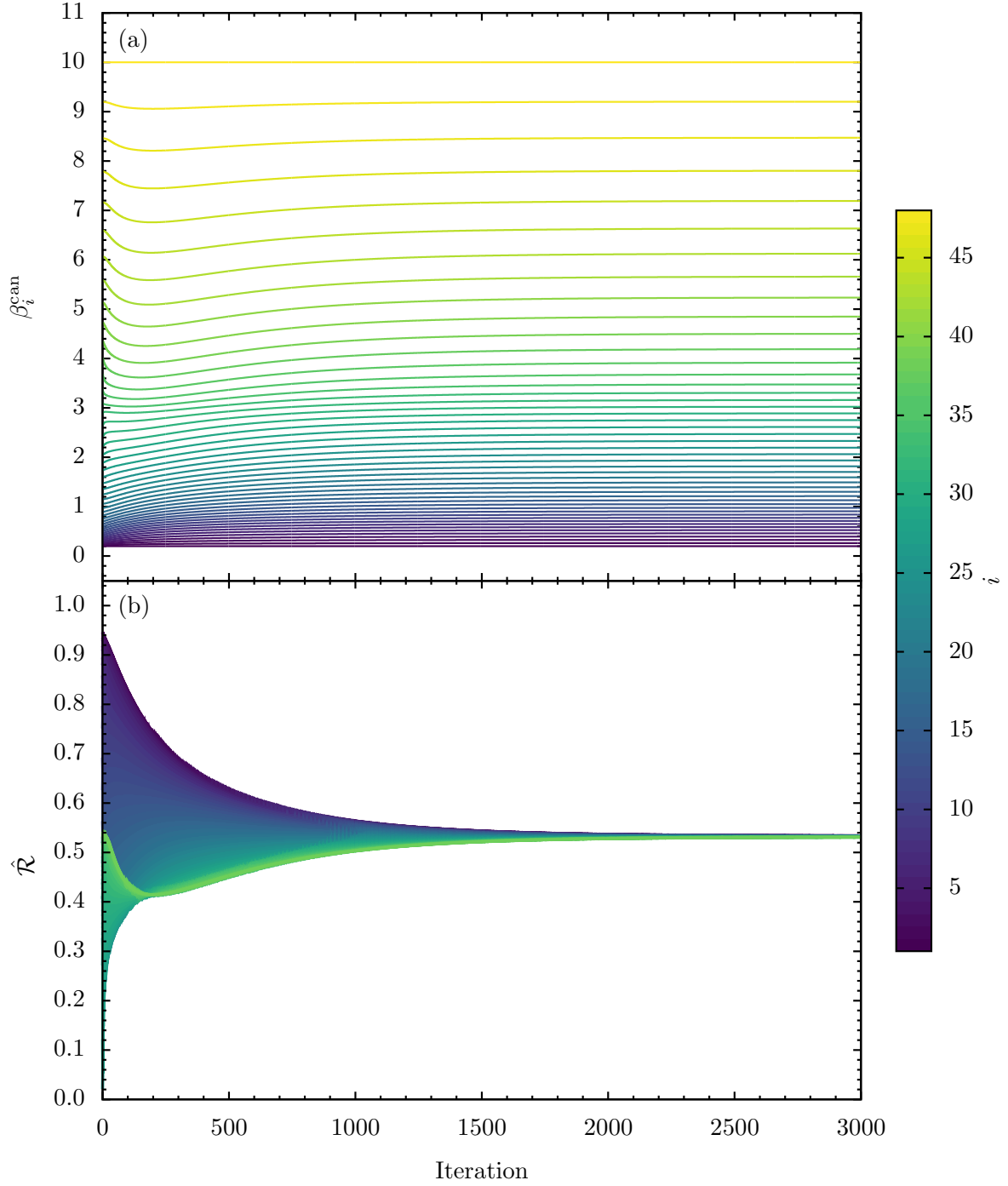


Figure 4.2: (a) Iteration process of adjusting temperatures for parallel tempering using the expected exchange rate given in Eq. (4.2) and (b) corresponding estimated exchange rates for each iteration for a flexible polymer with $N = 55$ monomers. The total number of simulation threads is 48, and the threads colored from deep green to yellow-green color in increasing order.

Table 4.1: A parallel tempering temperature set obtained from the energy method iterations illustrated in Fig. 4.2 for a 55-mer flexible polymer model i is the index of the simulation thread.

i	β_i^{can}	i	β_i^{can}	i	β_i^{can}	i	β_i^{can}	i	β_i^{can}	i	β_i^{can}
1	0.20000	9	0.71112	17	1.30142	25	2.19498	33	3.30581	41	5.65759
2	0.26206	10	0.77403	18	1.39407	26	2.33193	34	3.47586	42	6.12293
3	0.32738	11	0.83880	19	1.49173	27	2.47244	35	3.67790	43	6.63282
4	0.39380	12	0.90626	20	1.59465	28	2.61407	36	3.91552	44	7.19119
5	0.45966	13	0.97704	21	1.70303	29	2.75391	37	4.18980	45	7.80226
6	0.52411	14	1.05165	22	1.81713	30	2.89001	38	4.50084	46	8.47085
7	0.58709	15	1.13042	23	1.93714	31	3.02323	39	4.84855	47	9.20207
8	0.64914	16	1.21361	24	2.06316	32	3.15873	40	5.23364	48	10.00100

$$\hat{\mathcal{R}}(\langle E_{i-1} \rangle, \beta_{i-1}^{\text{can}} \leftrightarrow \langle E_i \rangle, \beta_i^{\text{can}}) = \hat{\mathcal{R}}(\langle E_i \rangle, \beta_i^{\text{can}} \leftrightarrow \langle E_{i+1} \rangle, \beta_{i+1}^{\text{can}}). \quad (4.3)$$

The same procedure is repeated in the following iteration for the even-order temperatures by keeping the odd-order temperatures fixed. Repeating these two steps sufficiently frequently, the exchange rate will converge. In addition, for estimating the average energy a linear extrapolation between the data points was used. The actual iteration process is illustrated in Fig. 4.2. It is worth mentioning that the two end temperatures are not altered during the whole iteration process and the number of temperature threads is kept the same. After convergence is reached, the new temperature set was used in the subsequent parallel tempering simulations. The actual temperature values obtained in the iteration process are listed in Tab. 4.1 with their thread indices. Then the actual exchange rate is measured during the simulation. The comparison of the exchange rates obtained with the updated temperature set and the previous simulation is shown in Fig. 4.3.

As we expected from the uniform exchange rate estimate, the overall distribution of the actual exchange rates is flattened compared to the previous geometric temperature setup. The high exchange rates in the random-coil phase are reduced to reasonable values, and the exchange near the freezing transition point is enhanced noticeably. In addition, the exchange rates are increased in the intermediate temperature region as well. We also tracked the replicas. Usually, the end replicas are expected to travel back and forth multiple times between the end temperatures. The tracks of two end replicas are shown in Fig. 4.4. The replicas can travel back and forth as desired. The

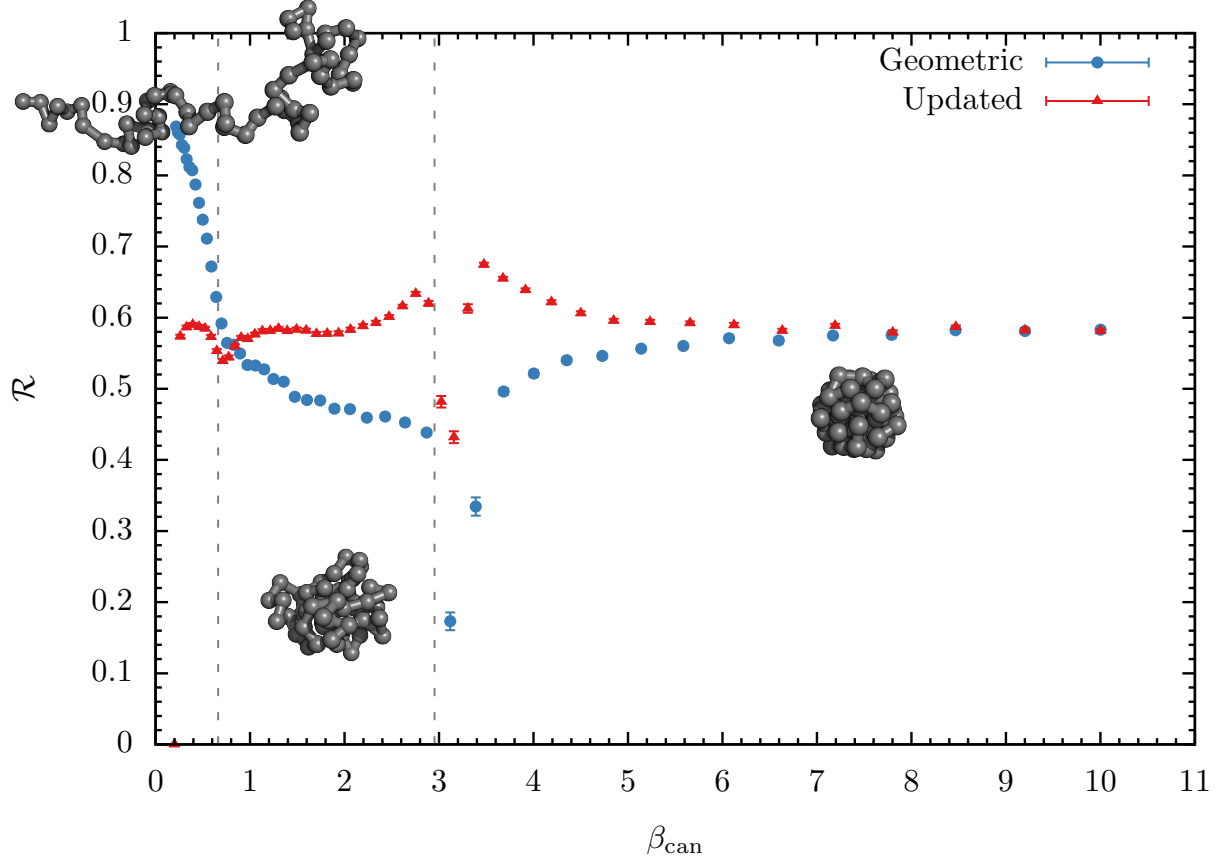


Figure 4.3: Comparison of the actual exchange rate for parallel tempering with the same number of simulation threads for a flexible polymer with $N = 55$ monomers. The known transition points are indicated by the dotted lines, and typical structures of the corresponding phases are shown.

obvious barrier near temperature thread 30 is caused by the freezing transition. To conclude, this type of iteration process results in reasonable and improved exchange rate distributions. Thus this method has also been used in the simulations of semiflexible polymers ($\kappa > 0$).

4.2 Combination of Advanced Updates

Besides improving temperature sets, another aspect of making the simulations more efficient is to employ more advanced update moves. Therefore, we implemented five different updates that have been introduced in the previous chapter: displacement updates, pivot rotational updates, bond-exchange updates, end-monomer-exchange updates, and crankshaft updates. In the actual

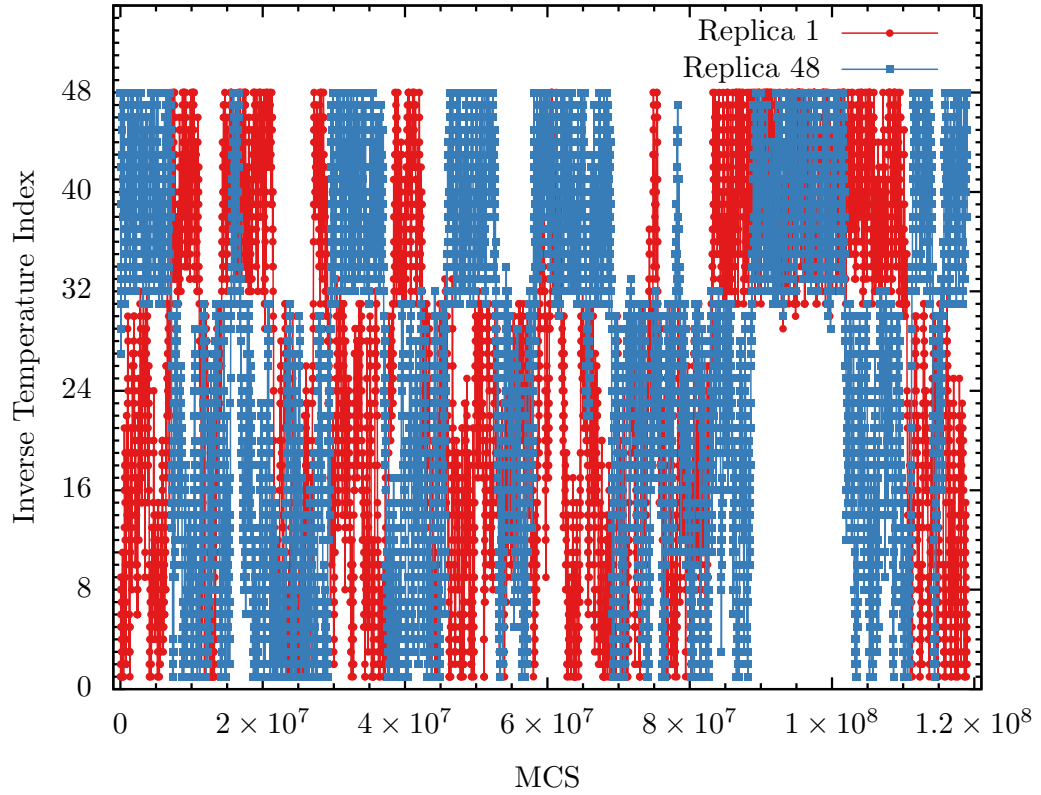


Figure 4.4: Tracking of two replicas in a parallel tempering simulation with 48 temperature threads within 10^8 Monte Carlo sweeps for a flexible polymer with $N = 55$ monomers.

simulation, we also modified the displacement box sizes according to the procedure (3.18), so that the overall displacement update acceptance rates of all simulation threads will be about 50%. As shown in Fig. 4.5, the adjustment is able to reach the equilibrium quickly within a short period of Monte Carlo sweeps. Besides, the displacement box size ratio of the largest ($\approx 0.3r_0$) and the smallest $\approx 0.05r_0$ can be up to 6, suggesting the necessity of adjusting the box sizes. The next step is to use the adjusted box sizes with other updates. In all the simulation threads, the portions of these updates are distributed as follows, 84% of displacement updates and 4% of each other updates. Actual measured acceptance rates of these updates are shown in Fig. 4.6. It is interesting to see that the acceptance rate distributions of different updates are affected by the dominant structures in each phase. As expected, displacement update acceptance rates in all the simulation threads are about 50% due to the preadjustment as described earlier. It is shown as the brown dots in Fig. 4.6

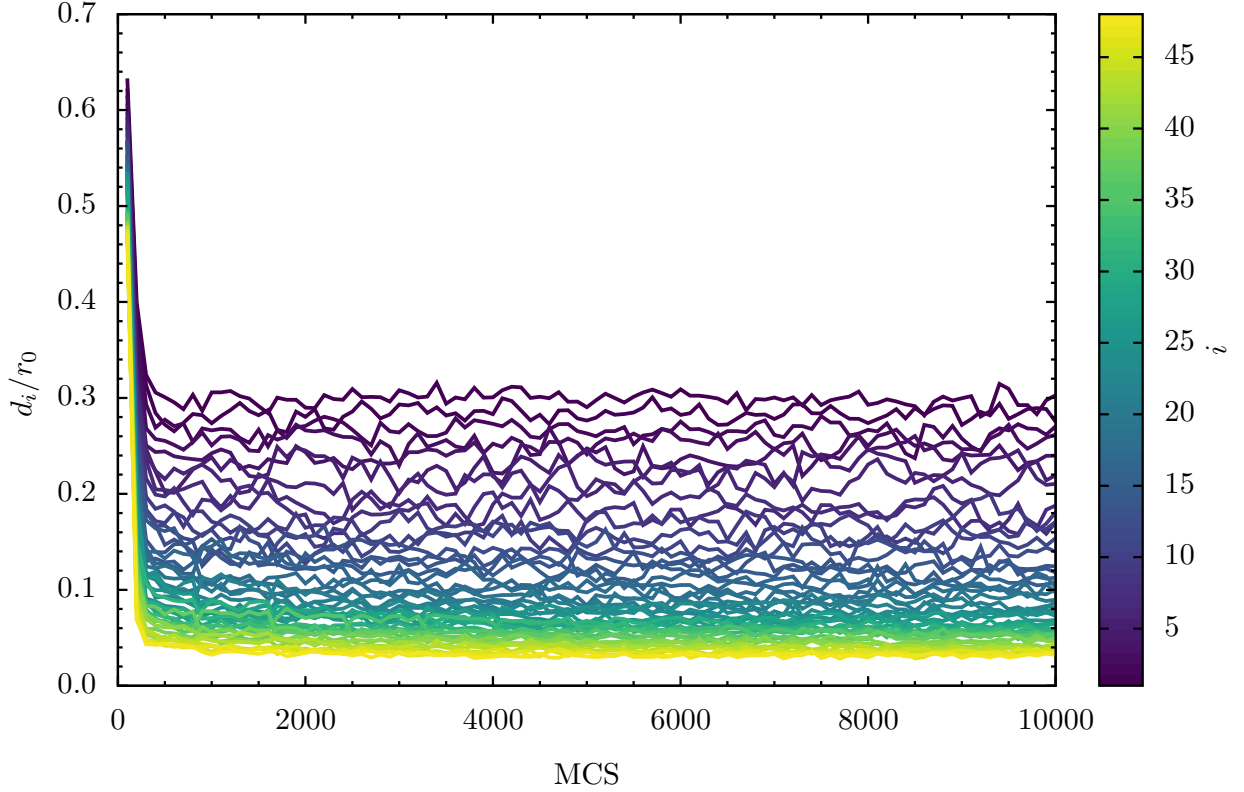


Figure 4.5: Actual adjustment of the displacement box edge length d_i in the temperature thread i for a flexible polymer with $N = 55$ monomers. The initial values are all set to $d_i = 0.5r_0$. The length is adjusted every 100 Monte Carlo sweeps (MCS). Larger index i indicates larger β_i^{can} (lower temperatures).

that the acceptance rate is close to zero at low temperatures if the uniform box size ($d_i = 0.3r_0$) is used for all simulation threads. However, the pivot rotational update acceptance rate quickly drops closer to zero from the random-coil phase to the liquid-globular phase after the collapse transition. Rotating the part of the polymer chain mostly causes the overlap of monomers, thus they are mostly rejected, and the same as well for the dense solid-globular conformations. The crankshaft update acceptance rates also show similar behavior as the pivot rotational update, and it is also affected by the available space for monomers to rotate. However, it does not drop to zero even at low temperatures. The reason is that the crankshaft update is a local update in contrast to the pivot rotational update, which is a global update. Therefore, the crankshaft update is still able to explore the locally available spaces even though the conformation is globally compact. However,

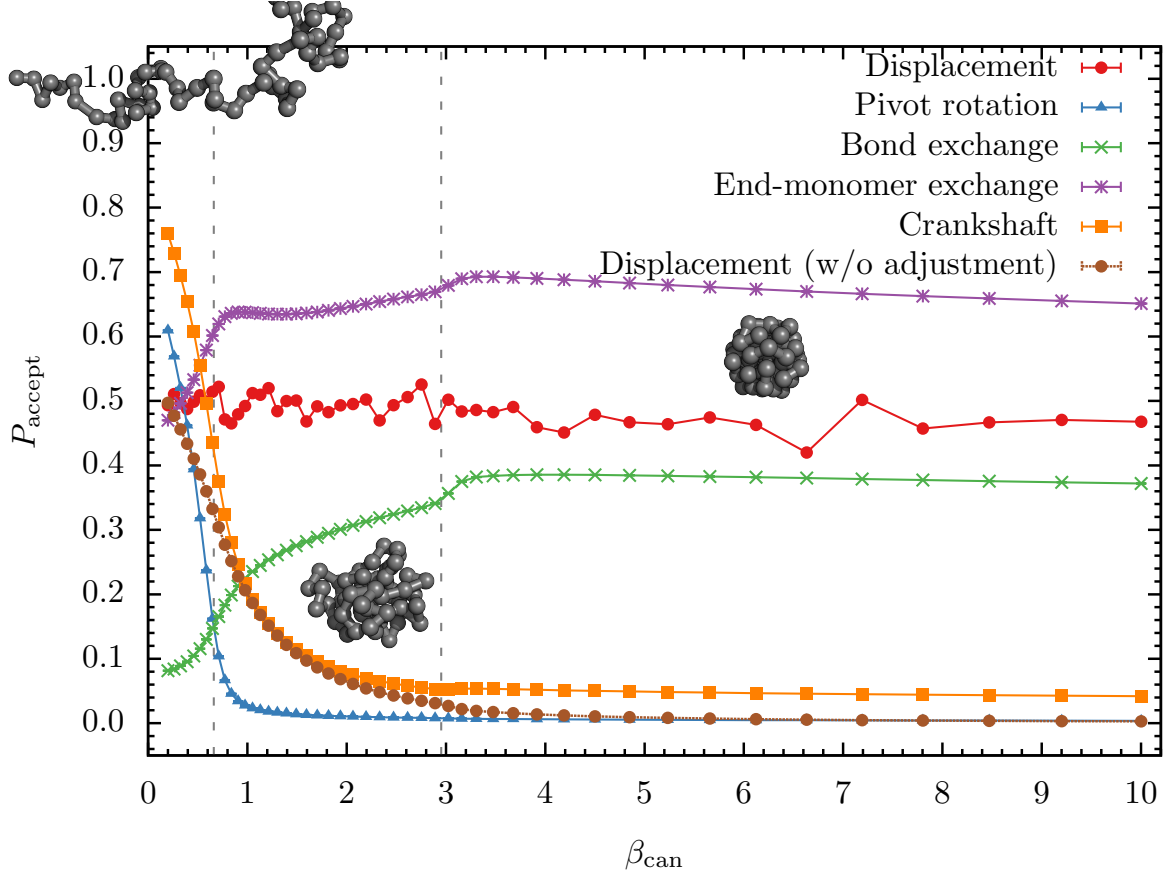


Figure 4.6: Actual acceptance rate of different updates in the simulation thread for a flexible polymer with $N = 55$ monomers. The brown is the acceptance rate of the displacement updates from a different simulation with the same temperature setups, where the box edge length is set to $d_i = 0.3r_0$ in all simulation threads i . The known transition points are indicated by the dotted lines, and typical structures of the corresponding phases are shown.

bond-exchange and end-monomer-exchange updates show reversed trends compared to previous updates. They have relatively low acceptance rates in the random-coil phase and benefit from compact liquid- and solid-globular conformations. Besides, the kinks also reflect the transition points, as they are inherently related to the compactness of the structures. Moreover, the high acceptance rate of the end-monomer exchange indicates that the end monomers are always closer to the rest of the chain, no matter which phase. On the other hand, the bond-exchange updates require more compact and more internally ordered conformations to find available bonds for exchange.

What's more, these two updates have almost constant acceptance rates in the solid-globular phase, which also indicates the stability of the frozen compact conformations in this phase.

In conclusion, adjusting the box sizes for displacement updates results in a near-uniform acceptance rate distribution among different temperature threads. Pivot rotational updates and crankshaft updates are helpful for sampling in the high-temperature region, where the conformations are mostly extended but are mostly rejected in the low-temperature region. The reverse trend applies to the bond exchange and end-more exchange updates. Therefore, these combinations of updates ensure efficient sampling in all temperature threads by high-acceptance-rate updates compensating for low-acceptance-rate updates.

4.3 Canonical Analysis

The canonical approach has been the conventional way to study the thermodynamic behavior of a system. It usually involves finding the extremal point of the thermal fluctuations, which is defined by Eq. (2.35) and typically indicates a dramatic change in macrostates. Since the system energy E is calculated in each update during the Monte Carlo simulations, its thermal fluctuation, the heat capacity

$$C_V = \frac{d\langle E \rangle}{dT_{\text{can}}} = \frac{\langle E^2 \rangle - \langle E \rangle^2}{k_B T_{\text{can}}^2}, \quad (4.4)$$

is most commonly used as an indicator for phase transitions. Its peak usually indicates the enhanced thermal activity that is reflected by the fluctuations in system energy. As described in the previous chapter, the $1/T_{\text{can}}^2$ term in heat capacity may cause a false transition signal in fluctuating quantities. Therefore, also looking at the pure energy variance,

$$\text{Var}(E) = \langle E^2 \rangle - \langle E \rangle^2 = -\frac{d\langle E \rangle}{d\beta_{\text{can}}}, \quad (4.5)$$

helps identify extremal fluctuations of the energy. If there are no transitions, the variance is a monotonic function of the temperature. The fluctuations are much smaller at low temperatures

compared to the high-temperature region. The peaks of the variance, which represent larger fluctuations of the energy compared to neighboring temperatures, can also be used to identify the transitions as well.

For polymer systems, it is necessary to look at more observables. When the transition is entropy-driven, the peaks in the thermal fluctuations of the structural properties are much more pronounced compared to the energy fluctuations C_V . Therefore, we also analyzed the square radius of gyration,

$$R_{\text{gyr}}^2 = \frac{1}{N} \sum_{j=1}^N (\mathbf{r}_j - \mathbf{r}_{\text{c.m.}})^2, \quad (4.6)$$

where \mathbf{r}_j is the j th monomer's coordinate vector and $\mathbf{r}_{\text{c.m.}} = \sum_{j=1}^N \mathbf{r}_j / N$ is the center of mass. The radius of gyration describes the overall effective size of a polymer conformation, and thus its thermal fluctuation,

$$\Gamma_g = \frac{d\langle R_{\text{gyr}}^2 \rangle}{dT_{\text{can}}} = \frac{\langle R_{\text{gyr}}^2 E \rangle - \langle E \rangle \langle R_{\text{gyr}}^2 \rangle}{k_B T_{\text{can}}^2}, \quad (4.7)$$

is particularly helpful to capture the major structural changes.

Figure 4.7 shows the plots of the heat capacity C_V , the variance of the system energy, and the square radius of gyration fluctuation $d\langle R_{\text{gyr}}^2 \rangle / dT_{\text{can}}$ of the flexible polymer model with 55 monomers as a function of the inverse heat-bath temperature $\beta_{\text{can}} = 1/T_{\text{can}}$. First, there is a shoulder in the heat capacity at $\beta_{\text{can}} \approx 0.6$ indicating a possible transition. The clearly visible peaks in the energy variance and the fluctuations of the square radius of gyration confirm the transition. This is the well-known Θ transition, where extended random-coil structures collapse into more compact liquid-globular structures upon lowering the temperature. It is worth mentioning that the shoulder in the specific heat does not allow for precisely locating the transition point but the energy variance $-d\langle E \rangle / d\beta_{\text{can}}$ shows a clear peak, again suggesting that the inverse temperature is a more suitably defined thermodynamic variable than the temperature.

As shown in Fig 4.7, the freezing transition from the liquid-globular phase to the more ordered solid-globular phase is clearly reflected in all three fluctuation quantities by peaks at around

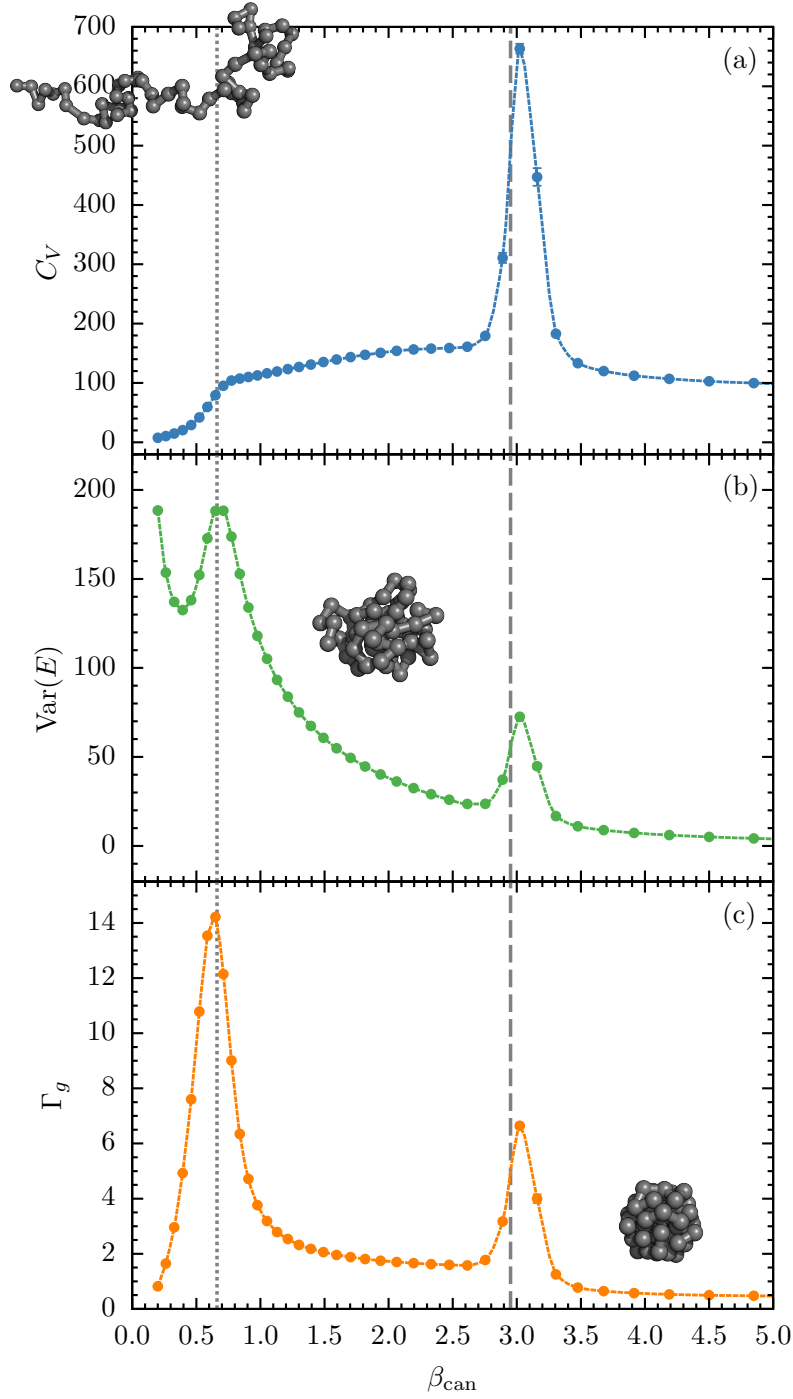


Figure 4.7: (a) Measured thermal fluctuations of the system energy, $C_V = d\langle E \rangle / dT_{\text{can}}$, (b) system energy variance $\text{var}(E)$, and (c) the thermal fluctuations of the square radius of gyration $\Gamma_g = d\langle R_{\text{gyr}}^2 \rangle / dT_{\text{can}}$ as a function of the inverse heat bath temperature $\beta_{\text{can}} = 1/T_{\text{can}}$ for a flexible polymer with $N = 55$ monomers. The known transition points are indicated by the dotted lines, and typical structures of the corresponding phases are shown. Error bars are about the size of data points.

$\beta_{\text{can}} \approx 3.0$. Besides, the peak value of Γ_g is smaller compared to the collapse transition, indicating a less drastic change in the compactness of the conformations.

However, even if the transitions are identified this way, there are some noteworthy problems. Due to the finite number of temperature measurements, we can not make sure the largest measured data point is the actual peak location. Besides, different quantities may indicate slightly different transition points. The difference between the shoulder of the heat capacity and the peak location of the fluctuations of the square radius of gyration for this model is shown in Fig. 2.4. To avoid ambiguities we perform a microcanonical inflection-point analysis to uniquely identify and classify the transitions.

4.4 Microcanonical Inflection-Point Analysis

In order to perform the microcanonical inflection-point analysis up to the third order, we first need to use the multiple-histogram reweighting method to estimate the density of states as described in section . From the parallel tempering simulations, we obtain the energy histograms at different temperature threads. The actual iteration process for this flexible polymer model is shown in Fig. 4.8. After about 1500 iterations, the convergence is achieved for all temperatures. It is interesting to see that the lower ranks (smaller β^{can}) converge slower than the higher ranks (larger β^{can}). The reason might be the uniform initialization of the partition function $Z(\beta_i^{\text{can}})$ overestimates the Boltzmann factor $e^{-\beta_{\text{can}}E}$ in the partition function for lower ranks (smaller β_{can}) in early iterations compared to higher ranks (larger β_{can}).

After obtaining the estimated density of states $\hat{g}(E)$, we recalculated the energetic quantities such as average energy, heat capacity, and energy variance to compare with the measured values from the parallel tempering simulation to cross-check the reweighting method. Moreover, in principle, we can obtain these energetic quantities for any temperature within the relevant temperature range. The comparison is shown in Fig 4.9. The reweighted results match the measured values, which provides additional confidence for our reweighting procedure. As suspected earlier, the freezing

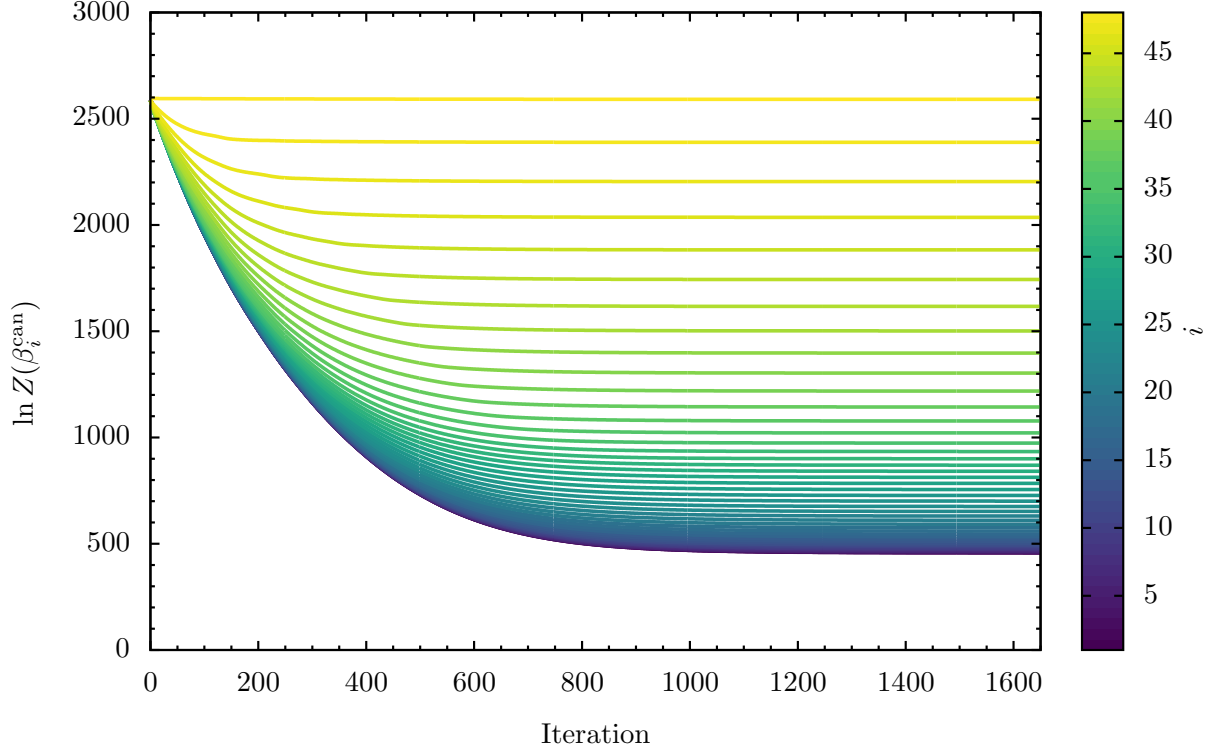


Figure 4.8: Interaction of logarithmic partition functions $\ln Z(\beta_i^{\text{can}})$ in the multi-histogram reweighting process for a flexible polymer model with 55 monomers. Larger index i indicates larger β_i^{can} (lower temperatures).

transition peak location of the heat capacity and the energy variance is different from the measured peak location of fluctuation quantities. In the next step, we used the Bézier method to smooth the estimated density of states to obtain the entropy curve and to calculate the derivatives up to 4th order. For the error calculations, we have used the Jackknife method in time series with correlated data and gaussian error calculation for independent runs. Eventually, the errors in the relative region are sufficiently small (typically much smaller than the line widths or point sizes) and thus can be for clarity in the remaining part of this dissertation. There are multiple contributions to these small errors. Firstly, we performed extensive Monte Carlo runs $\mathcal{O}(10^8) - \mathcal{O}(10^9)$ sweeps. This generates much less correlated and accurate data. As shown in Fig. 4.7, even the response quantities have relatively small error bars near the peak locations. Secondly, the multi-histogram reweighting method inherently optimizes error weights based on histogram statistics. Histograms

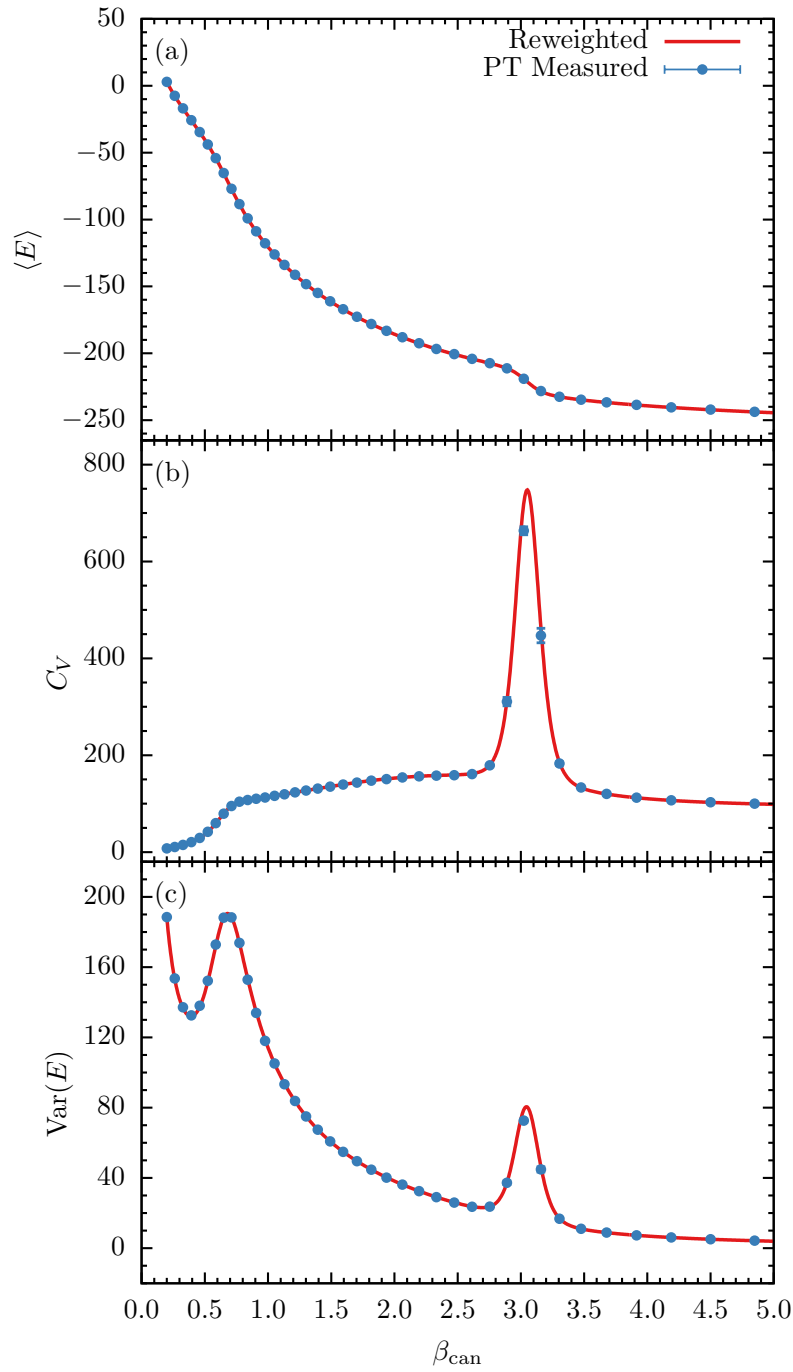


Figure 4.9: Comparison of recalculated values from reweighting (red lines) for (a) average energy, (b) heat capacity, and (c) energy variance between measured values from the parallel tempering simulations overflow a flexible polymer model with 55 monomers. Error bars are about the size of data points.

with more statistics in a certain energy region are given more weight for estimating the density of states. Finally, we use Bézier smoothing to reduce noise further.

As in the canonical analysis, we first discuss the low- β (or high-temperature) regime in the relevant energy region. The entropy $S(E)$, plotted in Fig. 4.10, does not possess any least-sensitive inflection points and thus there is no first-order transition, as expected. However, a least-sensitive inflection point in the first derivative $\beta(E)$ signals a second-order transition, which reflects the previously discussed entropy-driven Θ collapse transition from random-coil to liquid-globular structures. As a result, the corresponding next-order derivative $\gamma(E)$ shows a clear negative peak that helps unique determination of the transition point in energy and thus in β , in contrast to the ambiguity in the canonical analysis of response functions. Since there is no least-sensitive inflection point in $\gamma(E)$, the flexible polymer does not undergo a third-order transition in this region.

Figure 4.10 shows the same microcanonical quantities as plotted in Fig. 4.11, but for a lower energy range that covers the inverse temperatures in the interval $\beta \in [2.5, 4.0]$. The entropy curve does exhibit a least-sensitive inflection point, as expected for flexible polymers. This corresponds to the positive minimum in the backbending region found $\beta(E)$, which is a characteristic behavior for a first-order transition in microcanonical inflection-point analysis. The inverse temperature associated with it is approximately $\beta \approx 2.9$, which confirms earlier results about the freezing transition from liquid-globular to solid-globular structures for flexible polymers. Interestingly, identified by a positive minimum in the third-derivative $\delta(E)$, there is another inflection point in the second derivative $\gamma(E)$ at slightly lower energy than the major freezing transition energy, which corresponds to the inverse temperature $\beta \approx 3.14$. By performing a structure analysis [69], it can be shown that the major freezing transition point at the higher energy point corresponds to the formation of the icosahedral core from the less ordered liquid-globular phase, but the outer layer is still liquid-like. Upon lowering the energy further to the third-order transition point, the surface layer is adjusted and the overall structure is icosahedral (solid-like). The typical structures in this energy range are shown in Fig. 4.11. It is rather striking that this third-order signal is washed out

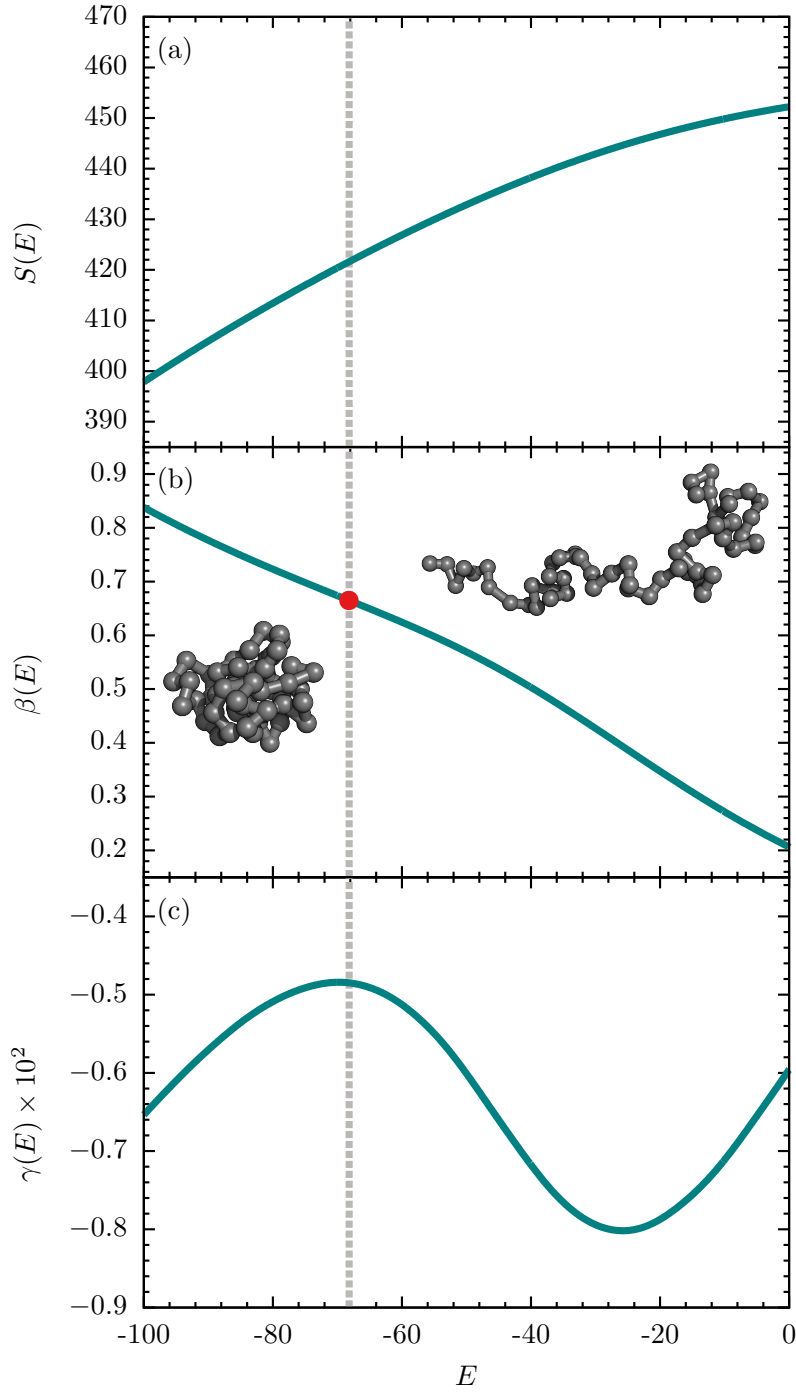


Figure 4.10: (a) Microcanonical entropy $S(E)$ and its derivatives (b) $\beta(E) = dS/dE$, and (c) $\gamma(E) = d\beta/dE$ as functions of the energy for a flexible model with 55 monomers. In this figure, we focus on the high-energy (or high-temperature) regime. Least-sensitive inflection points are marked by a dot, and the corresponding transition energy is indicated by a dashed line.

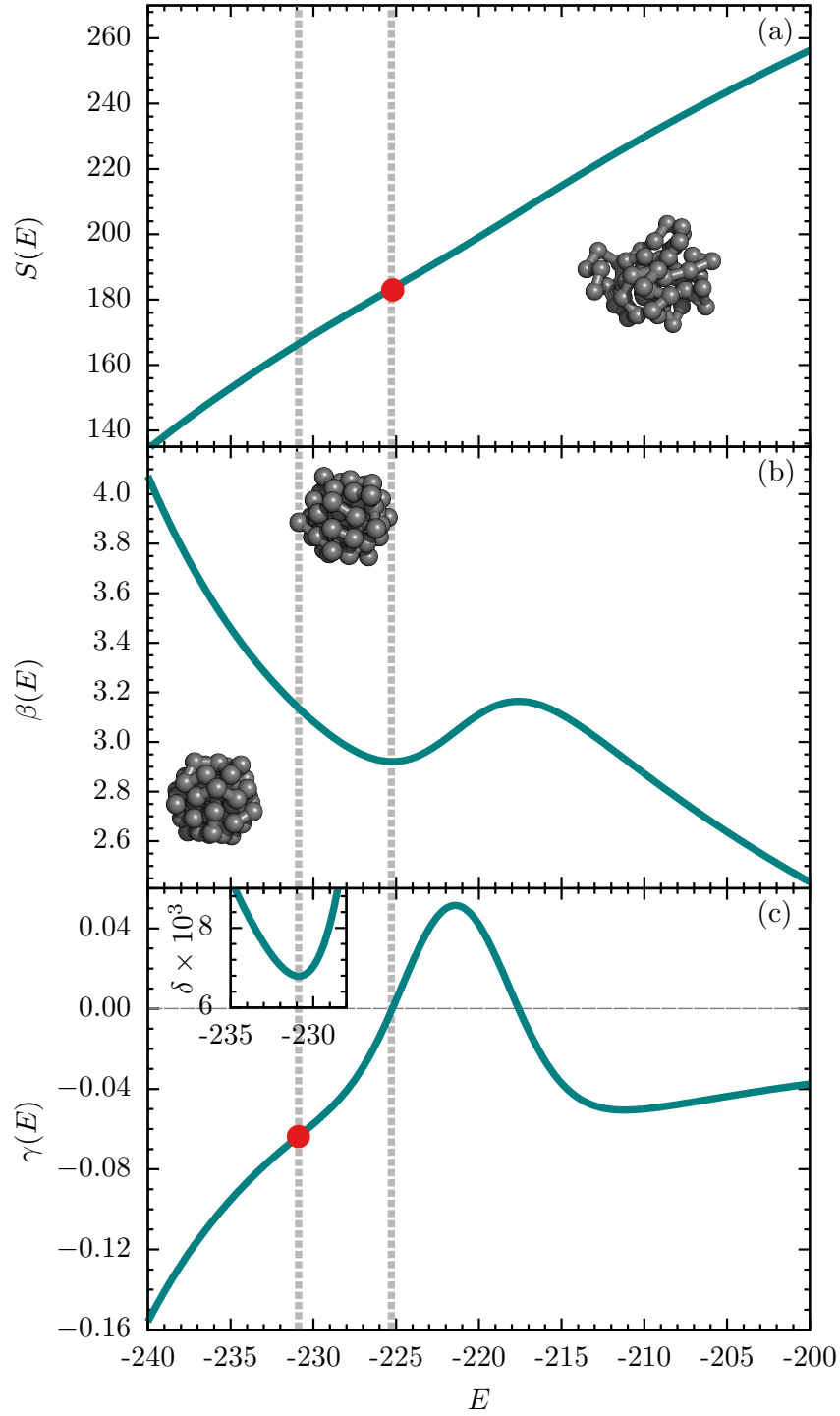


Figure 4.11: (a) Microcanonical entropy $S(E)$ and its derivatives (b) $\beta(E) = dS/dE$, (c) $\gamma(E) = d\beta/dE$, and (inset) $\delta(E) = d\gamma/dE$ as functions of the energy for a flexible model with 55 monomers. In this figure, we focus on the low-energy (or low-temperature) regime. Least-sensitive inflection points are marked by dots, and the corresponding transition energies are indicated by dashed lines.

during the averaging in the canonical analysis. Besides, we did not identify other transitions in the whole energy range.

To conclude, even though canonical analysis has long been the primary analysis method for studies of finite systems such as polymers in simulations, it turned out that this approach is not sensitive enough if transition signals are too close. These separate signals can be easily washed out during the averaging processes. In contrast, the recently introduced microcanonical inflection-point analysis method not only enables the systematic identification and classification of transitions, but it is also able to distinguish close transitions that standard canonical analysis cannot resolve. With this whole simulation and analysis process validated by the flexible polymer model, we will apply these methods to study the phase behavior of semiflexible polymers,

CHAPTER 5

ANALYSIS OF SEMIFLEXIBLE POLYMERS

In contrast to the flexible polymer model discussed in the previous chapter, the phase behavior of semiflexible polymers is affected by the bending stiffness. Therefore, in this chapter, we perform a detailed analysis of the transitions in semiflexible polymers. The focus is on the collapse transition, as well as the ground states[126–128].

5.1 Collapse Transition in Semiflexible Polymers

5.1.1 Replica-exchange Simulations of Semiflexible Polymers

Because of the chain rigidity that is introduced by the nonzero bending stiffness, the collapse transition temperatures are expected to shift toward lower temperatures, and so do the freezing transition temperatures. Therefore, the number of temperature threads in the simulation is increased to 60 for most κ values to enable the polymer to approach the ground states.

We first started from the same geometric temperature setup as we did for the flexible polymer to estimate the average energies as functions of the inverse temperature. Due to slower simulation dynamics compared to the flexible polymer, it takes longer for the semiflexible polymer to reach equilibrium. Less statistics available for the estimation of the average energy impacts the

temperature adjustment. After roughly estimating the average energies as functions of the inverse temperatures, we used the same energy method to adjust the temperatures for simulations of the semiflexible polymer. Exemplary iteration processes are shown for $\kappa = 5$ and $\kappa = 14$ in Fig. 5.1. The effect of less statistics can already be seen. The changes in the expected exchange rates are not as smooth as the iteration process for the flexible polymer. Nonetheless, the expected exchange rates approach $\hat{\mathcal{R}} \approx 0.6$, which is already a relatively high expected exchange rate for replica-exchange simulations.

Even though the previously discussed advanced updates were used for the parallel tempering simulations of the semiflexible polymers, these systems still follow relatively slow dynamics at low temperatures to reach equilibrium. Therefore, we expanded the replica-exchange simulations to the combined parameter space of simulation temperature and bending stiffness for efficiency. A comparison of simulating the semiflexible polymer at $T_{\text{can}} = 0.11$ using the conventional parallel tempering simulation and the extended replica-exchange technique is shown in Fig. 5.2 for the bending stiffness $\kappa = 10$. It depicts the running average of the system energy E with the same temperature setup in both types of simulations. Toward equilibrium, the running average of the system energy converges to a constant values when the measurement window is much larger than the autocorrelation time of the energy in Monte Carlo simulations. It can be seen that the simulation reaches equilibrium after about 6×10^7 Monte Carlo Sweeps (MCS), whereas the extended replica-exchange simulation only needs about 2.5×10^7 Monte Carlo Sweeps. It is almost a 60% reduction. Therefore, we mainly employed the extended replica-exchange simulations in the relatively interesting regions of the combined parameter space. The main advantage is that the additional degree of freedom in the 2D simulation allows the replicas to bypass free energy barriers.

In this study, we found $\Delta\kappa = 1$ is a sufficient spacing for varying κ values in the study of the phase behavior for semiflexible polymers, but we have also simulated several additional intermediate κ values where a finer resolution was needed. For $\kappa = 1$ and $\kappa = 2$, since their behavior is still similar to the flexible polymer ($\kappa = 0$), we still mainly employed the parallel tempering method.

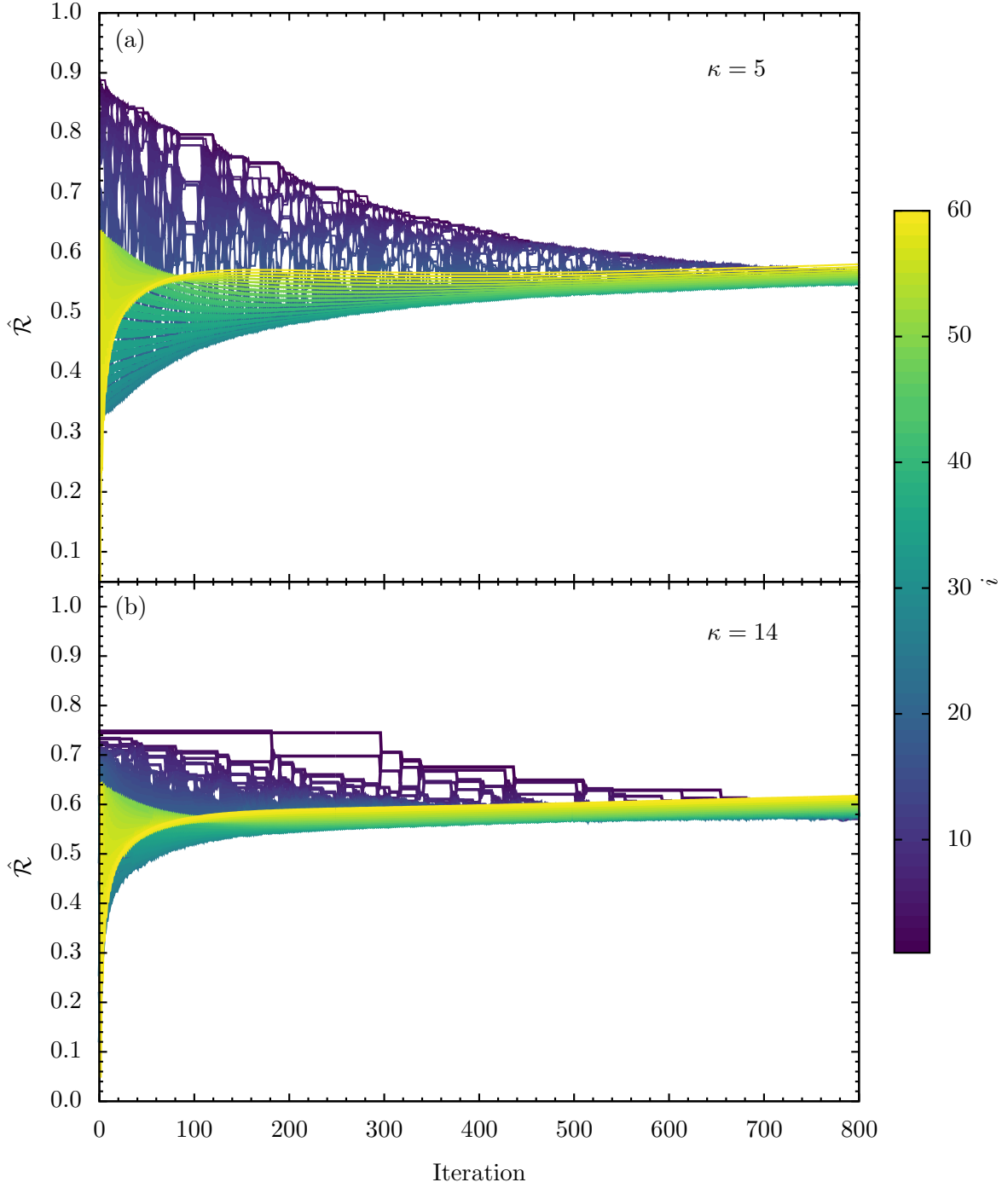


Figure 5.1: Iteration process of adjusting temperatures in parallel tempering using expected exchange rates for a semiflexible polymer with $N = 55$ monomers with bending stiffness (a) $\kappa = 5$, and (b) $\kappa = 14$. The total number of simulation threads is 60, and the index of the i th thread's heat-bath temperature is indicated by the color bar.

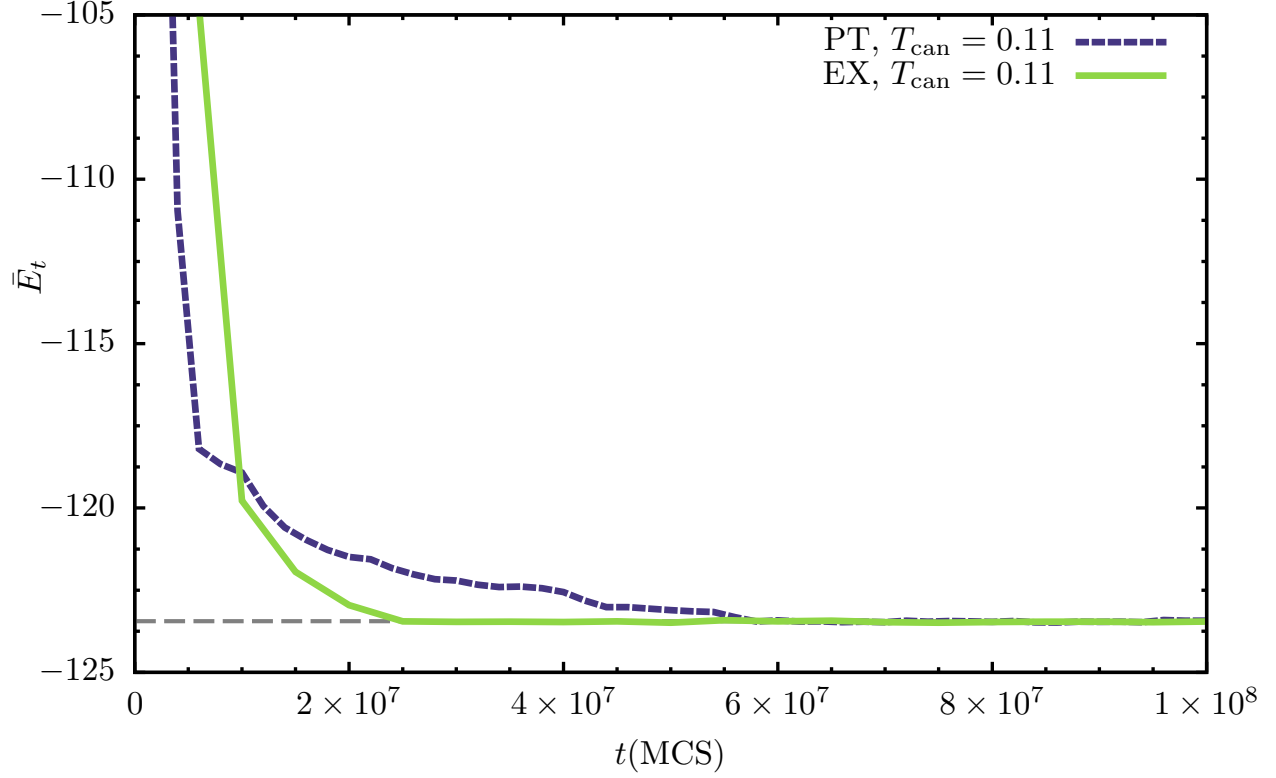


Figure 5.2: Running average of the energy when simulated with (a) parallel tempering, and with (b) extended (EX) replica-exchange method for a semiflexible polymer with bending stiffness $\kappa = 10$ at temperature T_{can} . The bin widths for the average calculation are 10^6 Monte Carlo Sweeps (MCS) for the PT and 2.5×10^6 for the extended replica exchange simulation.

Starting from $\kappa = 3$, we switched to the extended replica-exchange simulations with the temperature sets obtained from the adjustments that were previously introduced in Sec. 3.2.2. For the number of κ values for each extended simulation, we found it is sufficient to have 4 different bending stiffness values with 60 temperatures for each for a total of 240 simulation threads. In such a case, the total number of threads is sufficiently large.

5.1.2 Results for $\kappa \leq 6$

Canonical Analysis

The measured exchange rates of the extended replica-exchange simulation are shown in Fig. 5.3 for $\kappa = 3$, $\kappa = 4$, $\kappa = 5$ and $\kappa = 6$ at relatively high temperatures. The stable high exchange rates

in the temperature direction also show that the adjusted temperature sets from parallel tempering simulations work well in the extended simulations. The exchange rates are relatively large (darker orange color) at high temperatures. However, since there is more bending involved in the compact phase after the collapse transitions, the same conformation has a relatively large energy difference for different bending stiffness κ . Therefore, it causes a reduction of the exchange rates in the κ direction. Besides, it is interesting to see that the shifting of the collapse transition toward lower temperatures (larger β_{can}) is already noticeable for increased bending stiffness by the qualitatively changing of the exchange rates in the κ direction. Even though the exchange rate is smaller at lower temperatures, the high exchange rates at high temperatures still provide sufficient efficiency for the overall simulations.

As shown in Fig. 5.4, we have also measured the actual acceptance rates of different update moves. First, it shows that the displacement box-size adjustment produced an acceptance rate of about 50% for all the bending stiffness and temperature values. Second, the pivot rotational update acceptance rate decreases for lower temperatures (large β_{can}) for all bending stiffness values because of the compact structures. For increased bending stiffness, the pivot rotational update acceptance rates approach zero at lower temperatures which typically indicates the locations of collapse transitions. Interestingly, at these temperatures, the displacement acceptance rates have noticeable kinks with the largest deviations from smooth uniform distributions. This means that the pre-adjustment of the displacement box sizes is affected by the large fluctuations of the structures that are caused by the collapse transitions. It deviates more from the expected acceptance rate of 50%. Finally, the end-monomer- and bond-exchange update experience relatively low acceptance rates compared to other updates, especially at low temperatures. These low acceptance rates suggest that the conformations of semiflexible polymers are systematically affected by the bending stiffness, as expected. Because of the bond rigidity, the relative distances of monomers are larger compared to the flexible polymer conformations, and thus it dramatically reduces the number of possible new bonds to form after breaking the old bonds. However, these types of updates are still necessary and

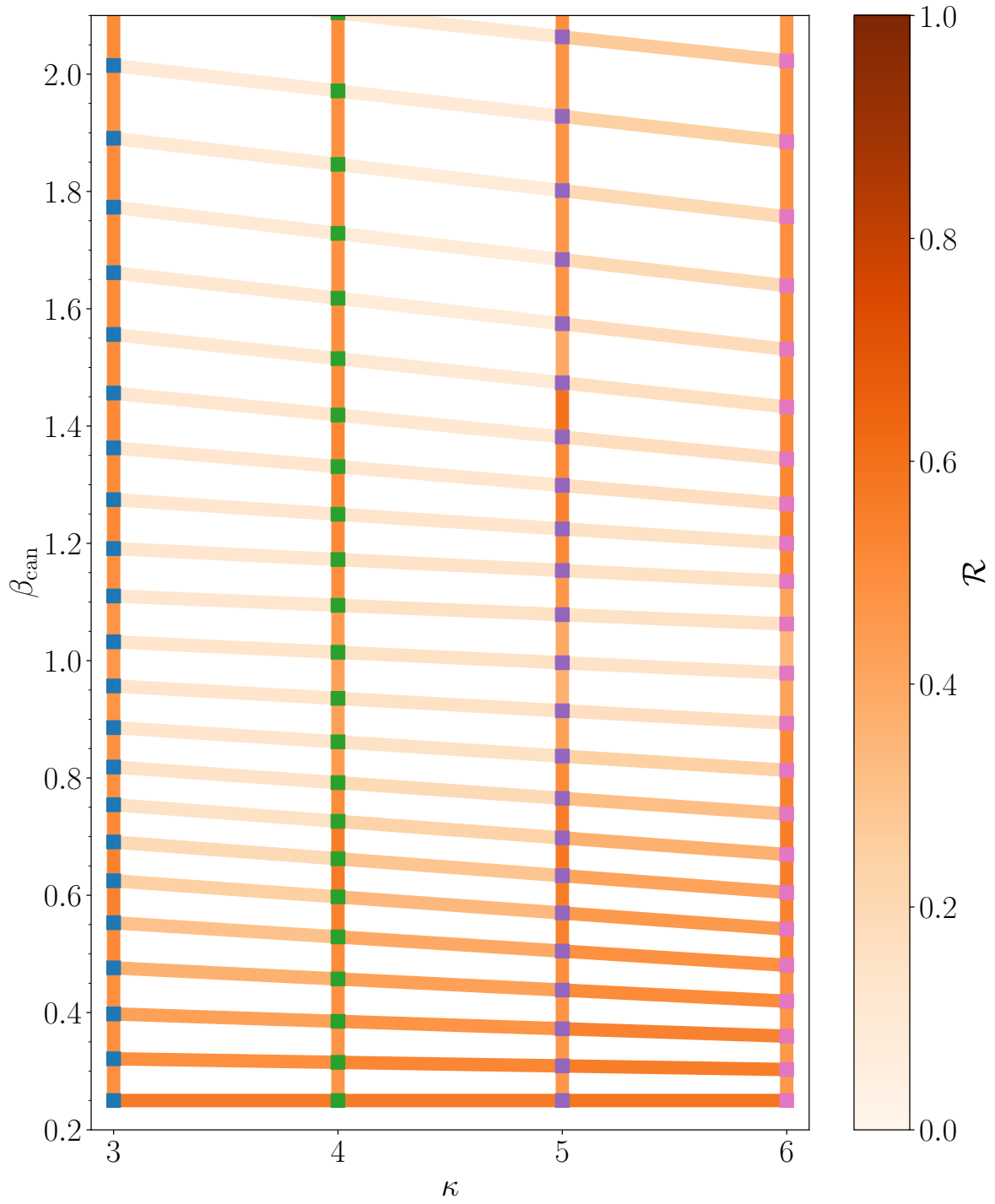


Figure 5.3: Measured exchange rates \mathcal{R} of extended replica-exchange simulations in the combined space of the inverse temperature and bending stiffness for $\kappa = 3$, $\kappa = 4$, $\kappa = 5$ and $\kappa = 6$ at relatively high temperatures. The square points mark the simulation threads in the parameter space. The shades of lines between neighboring threads corresponds to the exchange rate.

crucial at low temperatures to get out of trapped metastable states. In the plotted region, they still have nonzero ($\geq 1\%$) acceptance rates during about 5×10^8 attempted updates.

The plots of fluctuating quantities, such as the heat capacity $C_V = d\langle E \rangle / dT_{\text{can}}$, energy variance $\text{Var}(E) = -d\langle E \rangle / d\beta_{\text{can}}$ and the fluctuations of the square radius of gyration, $\Gamma_g = d\langle R_{\text{gyr}}^2 \rangle / dT_{\text{can}}$, allow for a more detailed analysis. All quantities are shown as functions of β_{can} in Figs. 5.5(a)-(c), respectively. Whereas we certainly see peaks forming from shoulders for increased bending stiffness in the curvature of the C_V , the plots of $\text{Var}(E)$ and the structural fluctuations show extrema for all the systems. These indicate the well-known Θ collapse transition between extended, random-coil structures and compact globular conformations. The transition signal is more pronounced for stiffer chains. Since this transition is more entropy- than energy-driven, it is not surprising that it shows up more prominently in the structural rather than the energetic fluctuations. It can also be seen that the peak values for all quantities increase for the stiffer chains, indicating greater fluctuations in both energetic and structural quantities in the system during the collapse transition. Interestingly, for $\kappa = 6$, the fluctuations of the square radius of gyration Γ_g is negative above the collapse transition temperature. This suggests that the semiflexible chain actually stretches out before collapsing into more compact structures, in contrast to the flexible polymer case, which continuously reduces its size upon lowering the temperature. The reason is that in this extended coil phase, the effect of the bending restraint is more prominent. If the temperature is reduced, so is the thermal energy $k_B T_{\text{can}}$ that causes fluctuations in the system. Finally, the peak locations of the response quantities confirm our previous observations in the exchange rates and the acceptance rates of different updates: The collapse transition occurs at lower temperatures for increased bending stiffness.

As described in the previous chapters, it is not surprising to see the ambiguity and inconsistency of canonical analysis persist for these systems. For $\kappa \leq 4$, the heat capacity only shows shoulders for the collapse transition, making it difficult to locate the transition points. Even though the energy variance and the fluctuations of the square radius of gyration show peaks, they clearly indicate different transition temperatures. Especially for $\kappa = 5$, there are two inverse temperature

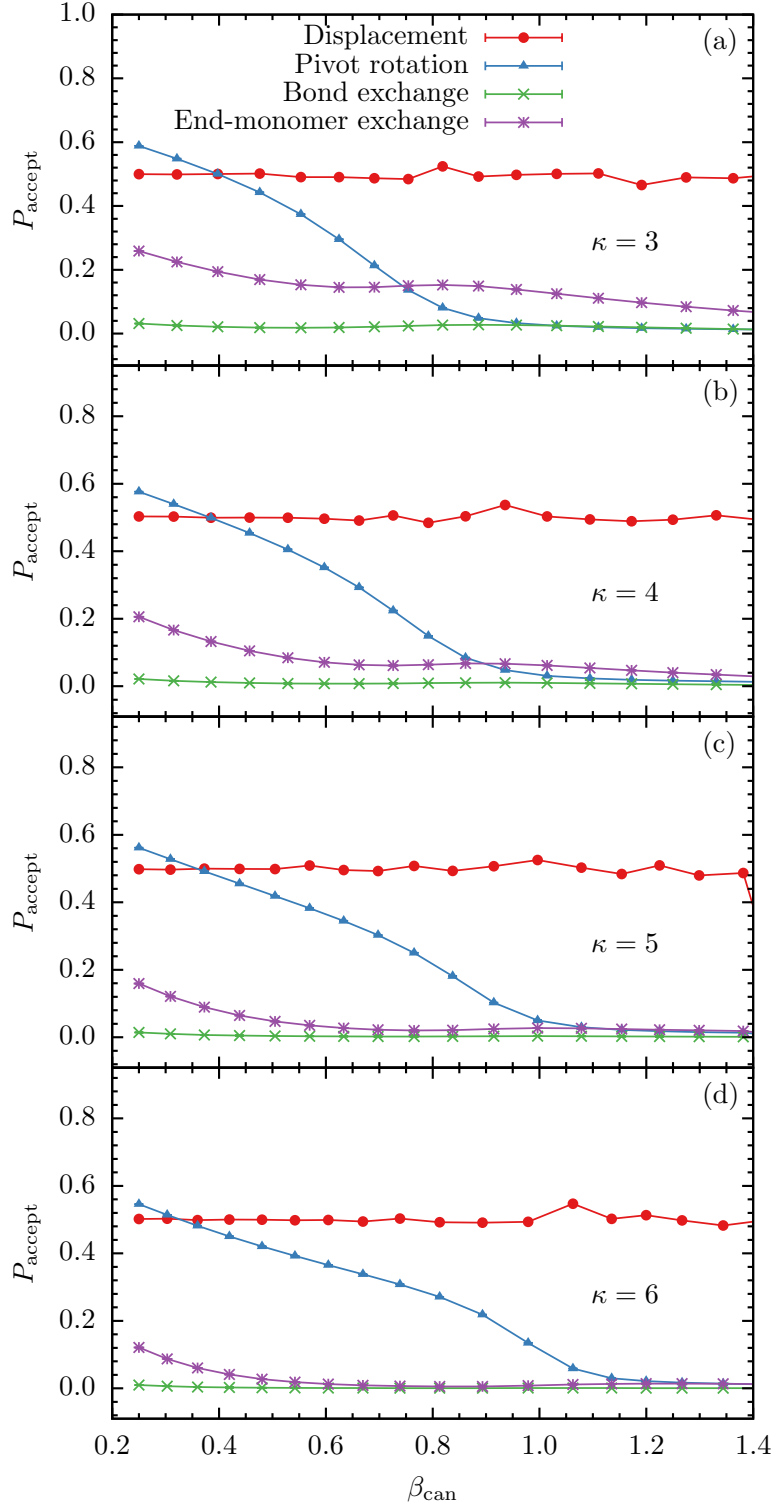


Figure 5.4: Measured acceptance rates of different updates in the extended replica-exchange Monte Carlo simulations for a semiflexible polymer model with 55 monomers with various bending stiffness κ

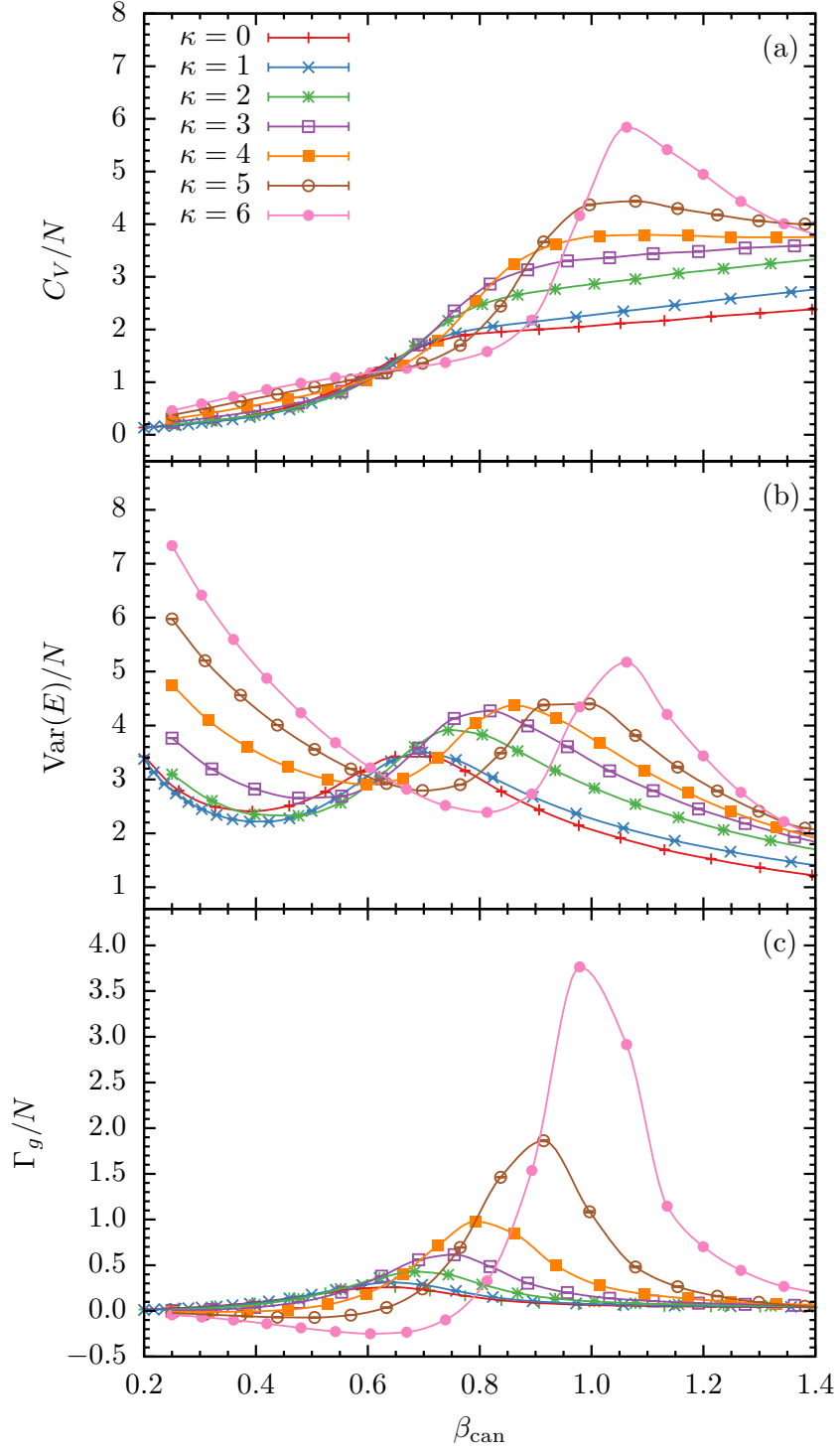


Figure 5.5: Thermal fluctuations of (a) energy (heat capacity $C_V = d\langle E \rangle / dT_{\text{can}}$), (b) energy variance $\text{Var}(E) = -d\langle E \rangle / d\beta_{\text{can}}$ and (c) thermal fluctuations of the square radius of gyration ($\Gamma_g = d\langle R_{\text{gyr}}^2 \rangle / dT_{\text{can}}$) for the semiflexible 55mer, plotted as functions of β_{can} for $\kappa = 3$, $\kappa = 4$, $\kappa = 5$ and $\kappa = 6$.

candidates, $\beta_{\text{can}} \approx 0.9$ and $\beta_{\text{can}} \approx 1.1$, to locate the peak location in the energy variance. To avoid these ambiguities, we perform a detailed microcanonical inflection-point analysis of these systems that aims at the unique identification and classification of the collapse transition in these systems in the following.

Microcanonical Inflection-Point Analysis

We performed multiple-histogram reweighting and employed the Bézier method to smooth the density of states and to calculate the derivatives of the microcanonical entropy. Figure 5.6 shows the microcanonical entropy and its derivatives up to the second order as functions of the reduced energy $\Delta E^{(\kappa)} = E - E_{\text{min}}^{(\kappa)}$, i.e., we subtracted from the energy the respective putative global energy minima $E_{\text{min}}^{(\kappa)}$. These were obtained for each system in the replica-exchange simulations and verified by the global optimization described in 3.2.3. This shift allows for an easier comparison of the results.

As in the canonical analysis, we discuss the low- β (or high-temperature) regime in the relevant energy space. The entropies plotted in Fig. 5.6(a) for all cases do not possess least-sensitive inflection points and thus there is no first-order transition. However, least-sensitive inflection points in the first derivative (β) signal second-order phase transitions in all these systems, which reflect the mostly entropic Θ collapse from random-coil to globular polymer structures. The corresponding peak locations in the second entropy derivative (γ), shown in Fig. 5.6(c), allow for a unique determination of the transition points in energy space and thus also in β . Two possible inflection points in γ for $\kappa = 3$ and $\kappa = 4$ are still under investigation. The quantitative results of the microcanonical inflection-point analysis obtained for the polymer systems studied here are listed in Table 5.1. As expected from the canonical analysis, the inverse temperature of the collapse transition increases for larger bending stiffness.

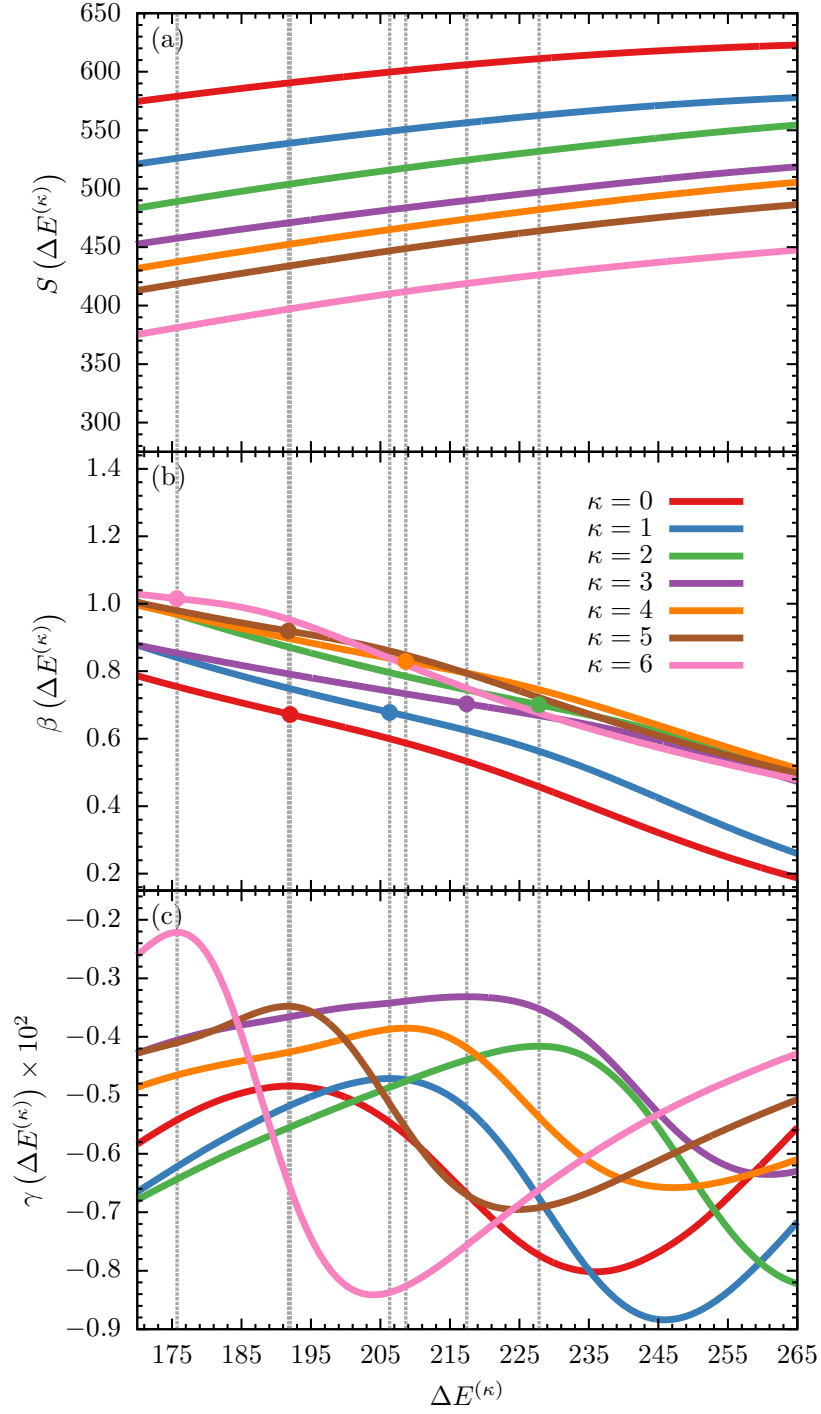


Figure 5.6: (a) Microcanonical entropy S and its derivatives (b) $\beta = dS/dE$, (c) $\gamma = d\beta/dE$, (d) $\delta = d\gamma/dE$ plotted as functions of the energy difference from the κ -dependent global energy minimum estimate for the semiflexible polymer with $\kappa \in [0, 6]$. Least-sensitive inflections in β are marked by a dot.

Table 5.1: Second-order transitions found from microcanonical analysis for the flexible ($\kappa = 0$) and semiflexible ($\kappa \in [1, 6]$) polymers. Transition energy E_{tr} , distance from putative ground-state energy $\Delta E^{(\kappa)}$, inverse microcanonical transition temperature β_{tr} are listed.

Bending stiffness	E_{tr}	$\Delta E^{(\kappa)}$	β_{tr}
$\kappa = 0$	-69.7	192.02	0.672
$\kappa = 1$	-24.6	206.3	0.678
$\kappa = 2$	5.0	227.8	0.701
$\kappa = 3$	12.6	217.4	0.703
$\kappa = 4$	21.3	208.7	0.829
$\kappa = 5$	16.1	191.8	0.919
$\kappa = 6$	9.19	175.7	1.015

5.1.3 Results for $7 \leq \kappa \leq 16$

Canonical Analysis

In this region of bending stiffness, we first simulated two sets of four κ values each, (7, 8, 9, 10) and (11, 12, 13, 14), by means of extended-replica exchange Monte Carlo simulations. We also employed the parallel tempering method for systems with bending stiffness $\kappa = 7.5$ and $\kappa = 8.5$ to investigate the behavior of the systems at a higher resolution between $\kappa = 7$ and $\kappa = 9$, as well as for $\kappa = 15$ and $\kappa = 16$ to expand the studied κ region.

We first measured the exchange rates to learn more about the performance of the simulations. The results are shown in Fig 5.7. For the two groups of extended replica-exchange Monte Carlo simulations, the overall exchange rates are relatively high ($\geq 50\%$) for both inverse temperature and bending stiffness directions. Especially, as shown in Fig 5.7(b) for $\kappa = 11, \dots, 14$, the exchange rates in both directions are almost uniform, indicating similar system behavior for these bending stiffness values. However, as it can be seen from Fig 5.7(a), the obviously reduced exchange rate between $\kappa = 7$ and $\kappa = 8$ around the inverse temperature $\beta_{\text{can}} = 1.2$ suggests that the system behavior might be qualitatively distinct for $\kappa = 7$ and $\kappa = 8$. This will be investigated further in the microcanonical inflection-point analysis.

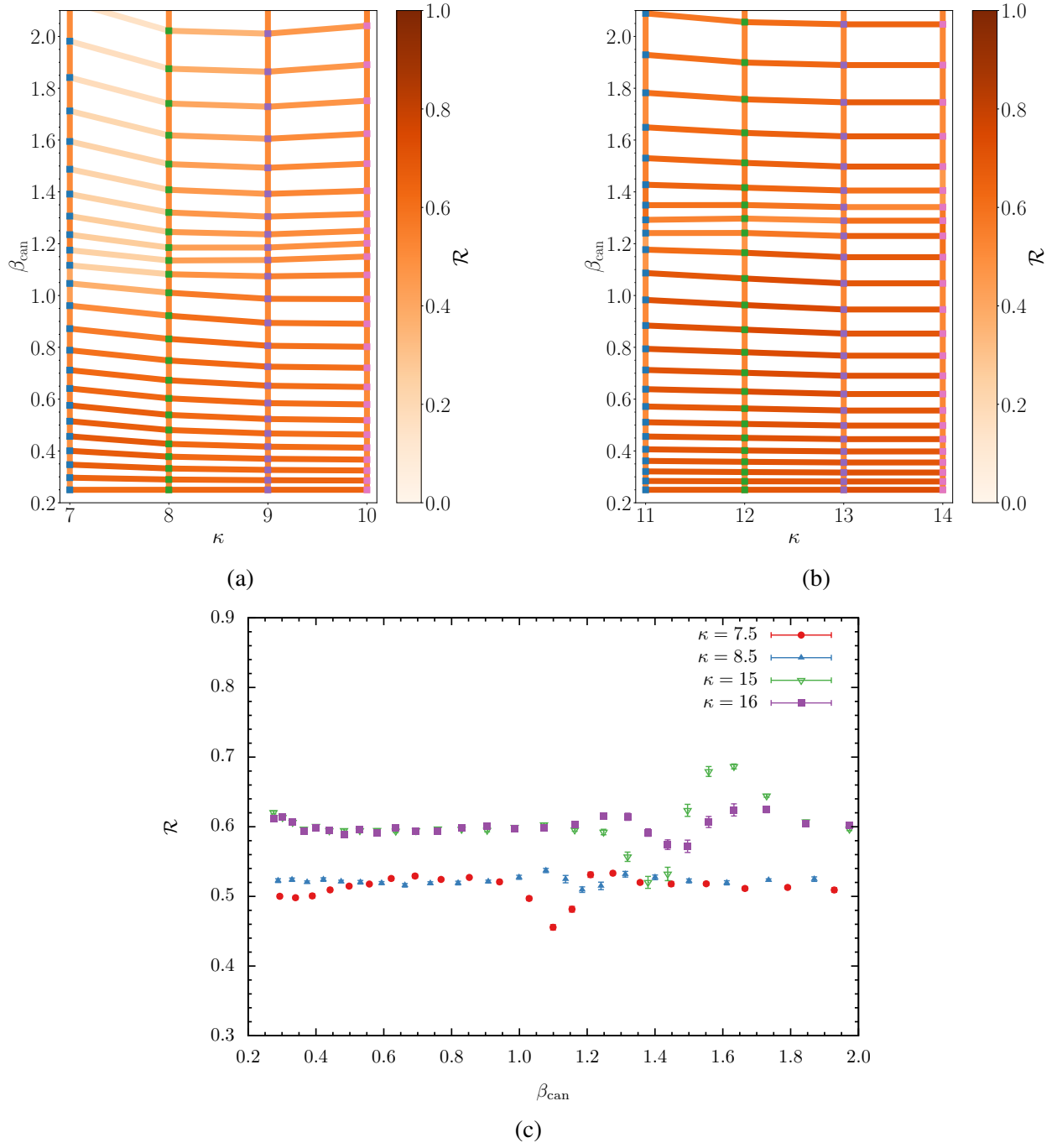


Figure 5.7: Measured exchange rates of separate extended replica-exchange simulations in the combined space of the inverse temperature and bending stiffness at relatively high temperatures for (a) for $\kappa = 7, 8, 9, 10$ and (b) for $\kappa = 11, 12, 13, 14$. Square symbols mark the location of simulation threads in the parameter space. The line colors represent exchange rates between neighboring threads. (c) Measured exchange acceptance rates at relatively high temperatures for $\kappa = 7.5, 8.5, 15, 16$.

Due to the extensive effort of parameter tuning, the expected shift of collapse transition temperature is not visible in the exchange rates from the extended replica-exchange simulations. However, we do find the qualitative indication of the transition shift as shown in Fig. 5.7(c). Typically, large deviations in the exchange rates from a uniform distribution can be associated with phase transitions. As expected, the estimated collapse transition inverse temperature increases from $\beta_{\text{can}} \approx 1.15$ for $\kappa = 7.5$ to $\beta_{\text{can}} \approx 1.6$ for $\kappa = 16$. This continues the trend already observed in the previous section for $\kappa \leq 6$.

Canonical response quantities, such as heat capacity $C_V = d\langle E \rangle / dT_{\text{can}}$, energy variance $\text{Var}(E) = -d\langle E \rangle / d\beta_{\text{can}}$ and fluctuations of the square radius of gyration, $\Gamma_g = d\langle R_{\text{gyr}}^2 \rangle / dT_{\text{can}}$ are shown as functions of β_{can} in Fig. 5.8 for this range of bending parameter values. For $7 \leq \kappa \leq 10$, we observe sharper peaks in the curvature of the C_V upon increasing the bending stiffness. The same trend can be observed from the plots of $\text{Var}(E)$ and the fluctuations of the square radius of gyration Γ_g as well. These indicate the same behavior as we observed for the chains with $\kappa \leq 6$, where the Θ collapse transition signal is more pronounced for the stiffer chains and occurs at lower temperatures. Surprisingly, the reverse trend is observed for $11 \leq \kappa \leq 16$. The peak values decrease and the peaks become wider again for larger κ values. However, these canonical response quantities do not provide extra information and insight into this interesting behavior. As described for $\kappa = 6$, the fluctuations of the square radius of gyration $\Gamma_g = d\langle R_{\text{gyr}}^2 \rangle / dT_{\text{can}}$ is negative above the collapse transition temperature for all κ values. It confirms again that for relatively large bending stiffness, the chains stretch out even more upon lowering the temperature in the extended coil phase. Finally, only one major peak in all these quantities still suggests a single collapse transition with enhanced thermal activity between entropically favored worm-like chains at higher temperatures and energetically more ordered structures at lower temperatures.

It is also worth mentioning again that the ambiguity of canonical analysis for finite systems also exists here. As it can be seen for $\kappa = 7$ and $\kappa = 15$ in Fig. 5.8, the energetic fluctuation quantities and structural fluctuation quantities locate the transition at different temperatures. Therefore, in the

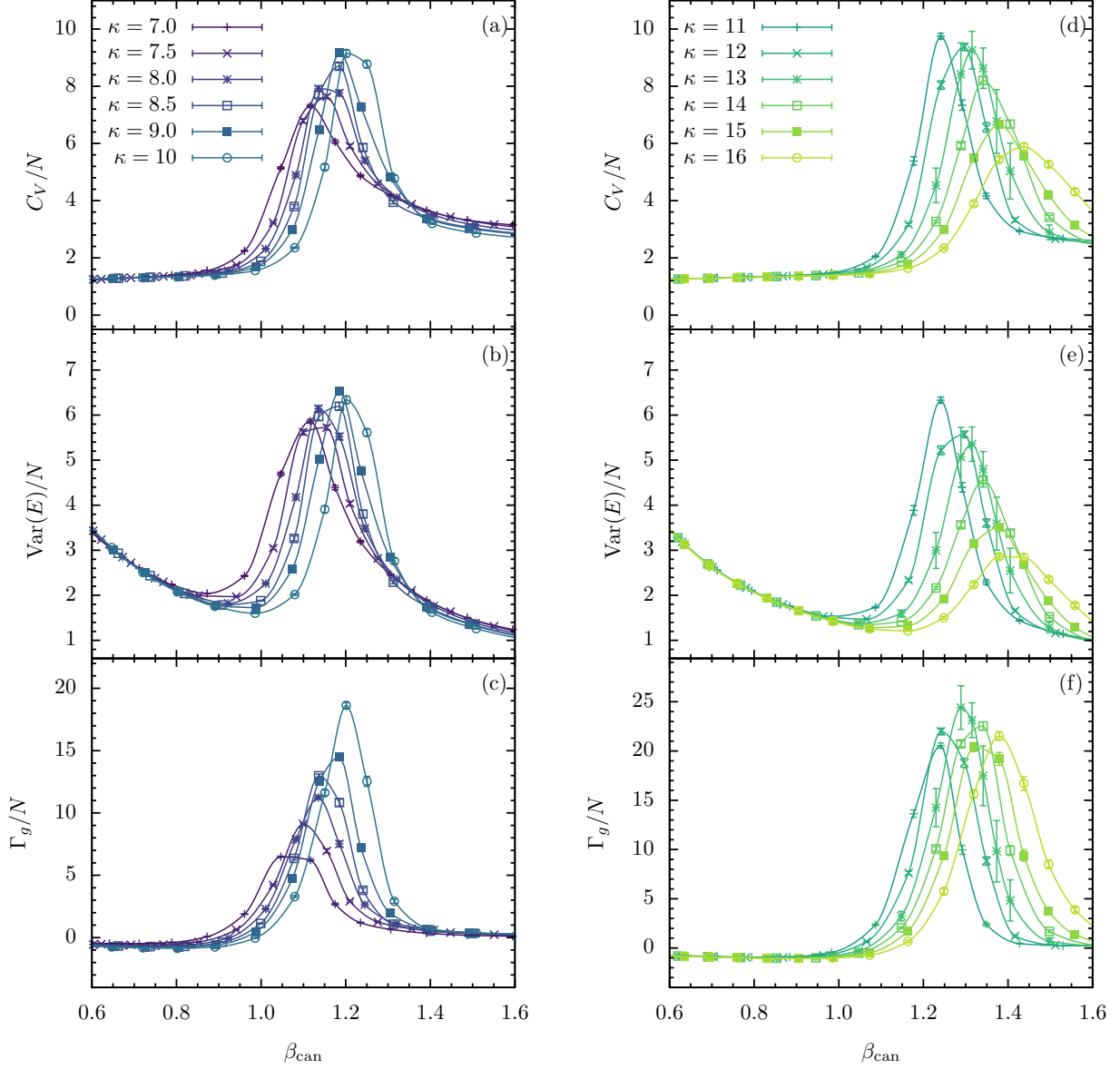


Figure 5.8: Thermal fluctuations of (a), (d) energy (heat capacity $C_V = d\langle E \rangle / dT_{\text{can}}$), (b), (e) energy variance $\text{Var}(E) = -d\langle E \rangle / d\beta_{\text{can}}$ and (c), (f) square radius of gyration ($\Gamma_g = d\langle R_{\text{gyr}}^2 \rangle / dT_{\text{can}}$), plotted as functions of β_{can} at selected values of the bending stiffness, $7 \leq \kappa \leq 16$.

next section, we perform a detailed microcanonical inflection-point analysis to get insights into the interesting reduction in exchange rates between $\kappa = 7$ and $\kappa = 8$, and the reduction in peak values and widening of peaks in response quantities.

Microcanonical Inflection-Point Analysis

We again performed multiple-histogram reweighting methods and employed the Bézier method to obtain smooth estimates for the microcanonical entropy and its derivatives up to second order as shown in Figure 5.9 as functions of the reduced energy $\Delta E^{(\kappa)} = E - E_{\min}^{(\kappa)}$ in the collapse transition region.

The entropy S does not possess any least-sensitive inflection point in this region for $\kappa = 7$. However, we identified a least-sensitive inflection point in the β curve at $\Delta E^{(\kappa)} \approx 162$, which is an independent second-order transition according to the microcanonical inflection-point classification scheme. It corresponds to a negative maximum in γ . Similar to the chains with bending stiffness $\kappa \leq 6$, only one second-order transition was identified for the collapse transition in this region for the bending stiffness $\kappa = 7$.

For slightly increased bending stiffness $\kappa = 7.5$, surprisingly, least-sensitive inflection points are identified in both β and γ , in contrast to the expectation of a single transition point from the canonical analysis. One inflection point in β is located at $\Delta E^{(\kappa)} \approx 158$ and additional one emerges at the lower energy $\Delta E^{(\kappa)} \approx 144$ in γ , suggesting an independent third-order transition besides the main second-order transition.

The inflection point at $\Delta E^{(\kappa)} \approx 148$ in the entropy S for the greater bending stiffness $\kappa = 8.0$, corresponds to an independent first-order transition according to our scheme, and associated with a positive minimum in β . This indicates that the second-order collapse transition develops into a first-order transition, whereas the other inflection point in γ at $\Delta E^{(\kappa)} \approx 138$ remains a third-order order transition for $\kappa = 8.0$.

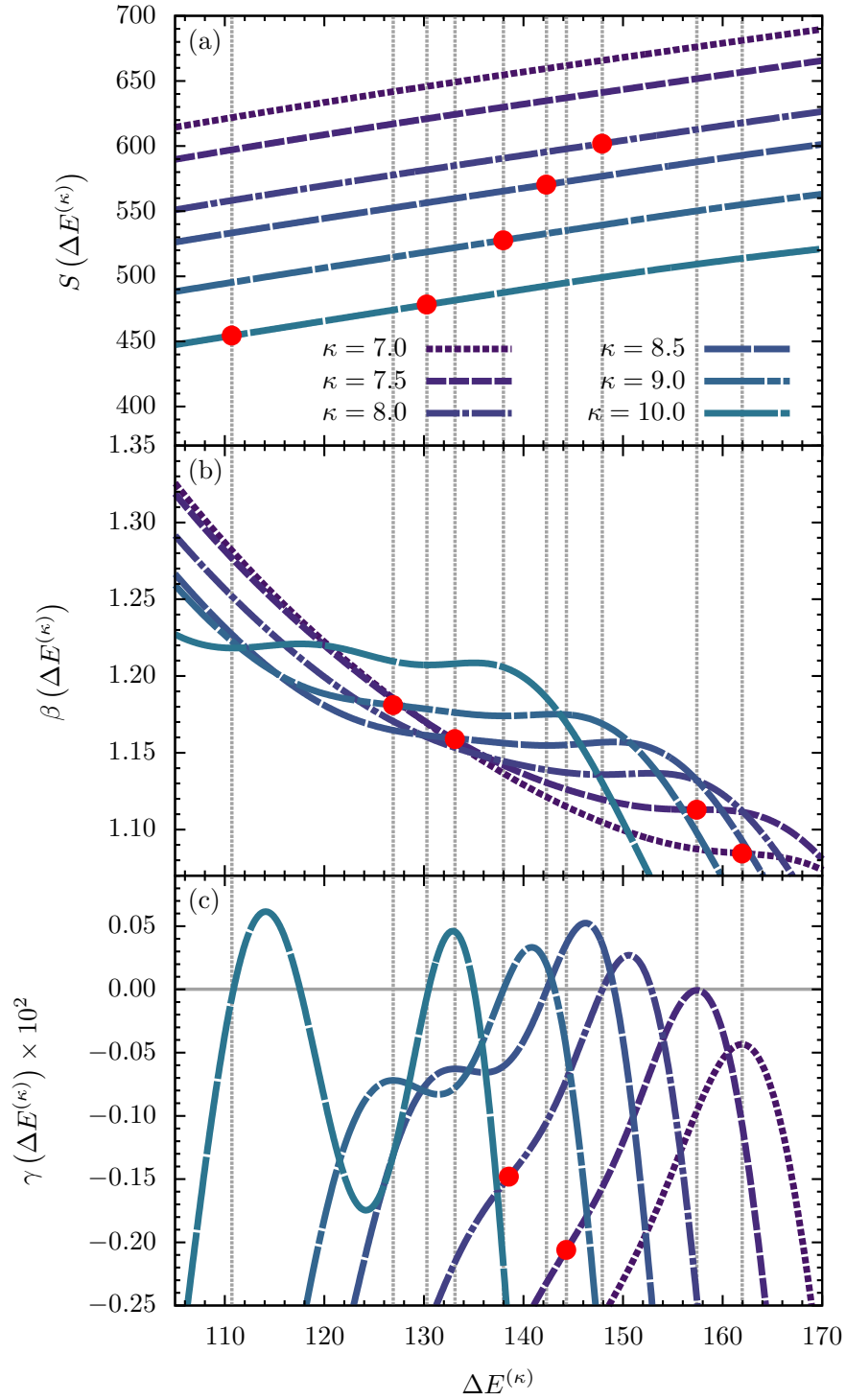


Figure 5.9: (a) Microcanonical entropy S and its derivatives (b) $\beta = dS/dE$, (c) $\gamma = d\beta/dE$ for the different models with $\kappa = 7.0, \dots, 10.0$ plotted as functions of the $\Delta E^{(\kappa)}$. Least-sensitive inflection points are marked by dots and transition energies are indicated by dotted lines.

For $\kappa = 8.5$ and $\kappa = 9.0$, the first least-sensitive inflection points at higher energies are in the entropy curves at $\Delta E^{(\kappa)} \approx 142$ and $\Delta E^{(\kappa)} \approx 138$, respectively. Therefore, these transitions are classified as first-order transitions. Interestingly, identified by the least-sensitive inflection points in β , the transitions at lower energies $\Delta E^{(\kappa)} \approx 143$ for $\kappa = 8.5$ and $\Delta E^{(\kappa)} \approx 127$ for $\kappa = 9.0$ are now second-order transitions, instead of third-order transitions.

It is striking that both least-sensitive inflection points are found in S for $\kappa = 10.0$, which are signaled by two separate positive minima in β . Thus, it confirms that the new transition branch finally turns into another first-order transition line and these two first-order transitions are found at $\Delta E^{(\kappa)} \approx 130$ and at $\Delta E^{(\kappa)} \approx 110$.

On an important note for generality, the transitions up to third order can also be studied only by analysis γ curves. This can be illustrated by the development of the bifurcation regarding the collapse transition up to third order for this range of κ values, as shown Fig. 5.9(c). First, the third-order transitions are identified by the least-sensitive inflection points in γ . Second, as we can see for $\kappa = 7$, the second-order transition causes a negative peak in γ , which is the case before the bifurcation happens. Finally, the first-order transitions cause positive minima in β , and thus the next derivative $\gamma = d\beta/dE$ at such a minimum point is zero and there will be a positive peak at slightly larger energies because of the backbending of β . Therefore, first-order transitions can be identified by the intersection of the ascending flows of the γ curve with the $\gamma = 0$ line. Consequently, the development of the second-order transitions into first-order transitions seems more natural, where the negative peaks of the second-order transitions cross the zero line in γ and become positive peaks. In this case, we can see from Fig. 5.9(c) that the major collapse transition starts from a negative peak (second order) for $\kappa = 7$ and eventually grows into a positive peak (first order) for $\kappa \geq 8.0$. Regarding the appearance of the new transition, it starts as an inflection point (third order) for $\kappa = 8.0$, forms a negative peak (second order) for $\kappa = 9.0$, and finally results in another positive peak (first order) for $\kappa = 10$.

We extended our microcanonical inflection-point analysis further for bending stiffness values $\kappa = \dots, 16$. The results are shown in Fig. 5.10. For all this range of bending stiffness values, there are two least-sensitive inflection points only in the entropy curves in this region. Therefore, these are independent first-order transitions that are clearly signaled by positive minima in β curves. Moreover, as can be seen from Fig. 5.10(a), the transition energy difference between the two first-order transitions increases for stiffer chains. This is also reflected in the β curves. For larger bending stiffness values, the difference of the corresponding microcanonical inverse transition temperatures is larger as well. Moreover, the back-bending features are more prominent for chains with greater bending stiffness.

In order to have more insight into the bifurcation of the collapse transition, we investigated the conformations in the relative energy range that is guided by the previous microcanonical inflection-point analysis. Finally, we constructed the hyperphase diagram, parametrized by bending stiffness κ and inverse temperature β , in the vicinity of the bifurcation point. It is shown in Fig. 5.11 for the range of κ values discussed in this section. The transition points identified by microcanonical inflection point analysis of simulation data are marked by symbols.

In the plotted region, the coil-globule transition line is still intact as a single second-order transition from the flexible case ($\kappa = 0$). However, it starts to split into two branches at about $\kappa = 7$ and $\beta = 1.08$, and thus the plotted region is dominated by three phases. It is important to note that, for increased bending stiffness, the upper line of the bifurcation starts off with third-order transitions, then turns into second order, and eventually becomes first order. We discussed this behavior in the context of γ curves as well. This is a typical characteristic feature of transition lines branching off a main line. Transitions of higher-than-second order are common in finite systems [13, 69]. Without their consideration, the phase diagram would contain a gap.

In the higher temperature regime (low β), the disordered phase C is governed by wormlike random-coil structures. As described in the canonical analysis of the negative thermal fluctuations in the square radius of gyration, the structures are more extended if close the collapse transition.

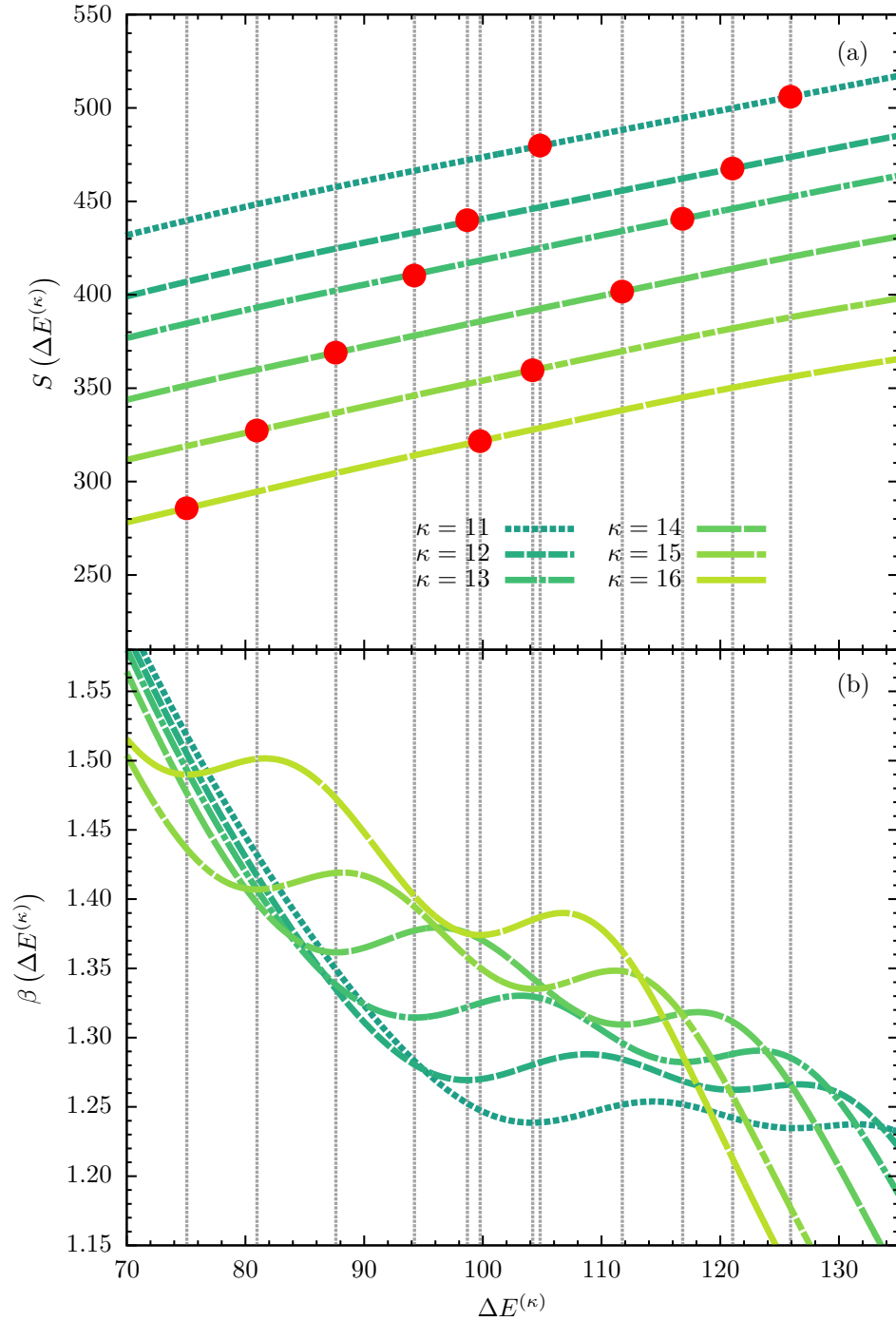


Figure 5.10: (a) Microcanonical entropy S and its derivatives (b) $\beta = dS/dE$ for the different models with $\kappa = 11, \dots, 16$ plotted as functions of $\Delta E^{(\kappa)}$. Least-sensitive inflection points are marked by a dot and transition energies are indicated by dotted lines.

In this regime, entropic effects enable sufficiently large fluctuations that suppress the formation of stable energetic contacts between monomers. For the bending stiffness right below $\kappa \leq 7$, the coil structures directly transition into the toroidal phase T upon lowering the temperature (increasing β). However, more interestingly, the formation of a new stable phase between the random-coil phase C and the toroidal phase T is observed if $\kappa > 7$. Such a phase is characterized by the coexistence of hairpins (H) and loop (L) structures. Therefore, we call it a mixed phase. The wormlike chains fold into hairpins or loops through this transition if the temperature is lowered. Eventually, further cooling leads to another transition into the toroidal phase T.

By analyzing the structures in these phases, we found that they process unique features of monomer-monomer contacts. Therefore, we used distance maps of monomers to characterize the phases. As shown in Fig. 5.11, the representative conformations as well as their distance maps for each phase are included. The two nonbonded monomers n and m are considered to be in close contact if their distance $r_{nm} < 1.2$, but the results are not very sensitive to this choice, as long as counting the nonnearest neighbor contacts is avoided. This distance is close to the minimum of the Lennard-Jones potential and represented by the red region in the triangular distance maps shown underneath the conformations. For the extended coil structures, stable contacts of monomers are prevented by thermal fluctuations, and thus they do not possess any particular features. In the intermediate phase, the tails of hairpin structures are in contact with antiparallel orientation. This results in the contact line that is perpendicular to the diagonal in the contact map, which made it easy to identify these structures. In loops, on the other hand, the tails have parallel orientation. Consequently, the short contact line is parallel to the diagonal in the contact map. In contrast to loops, toroids try to reduce system energy by forming additional contacts. As a result, an additional streak parallel to the diagonal in the contact map accounts for additional winding.

In order to quantify the population of different structures in each phase and to gain more insights into the transition behavior in this energy range, we have estimated the probabilities for each structure type. Detailed results are shown for κ in Fig. 5.12. The β curve is shown in Fig. 5.12(a)

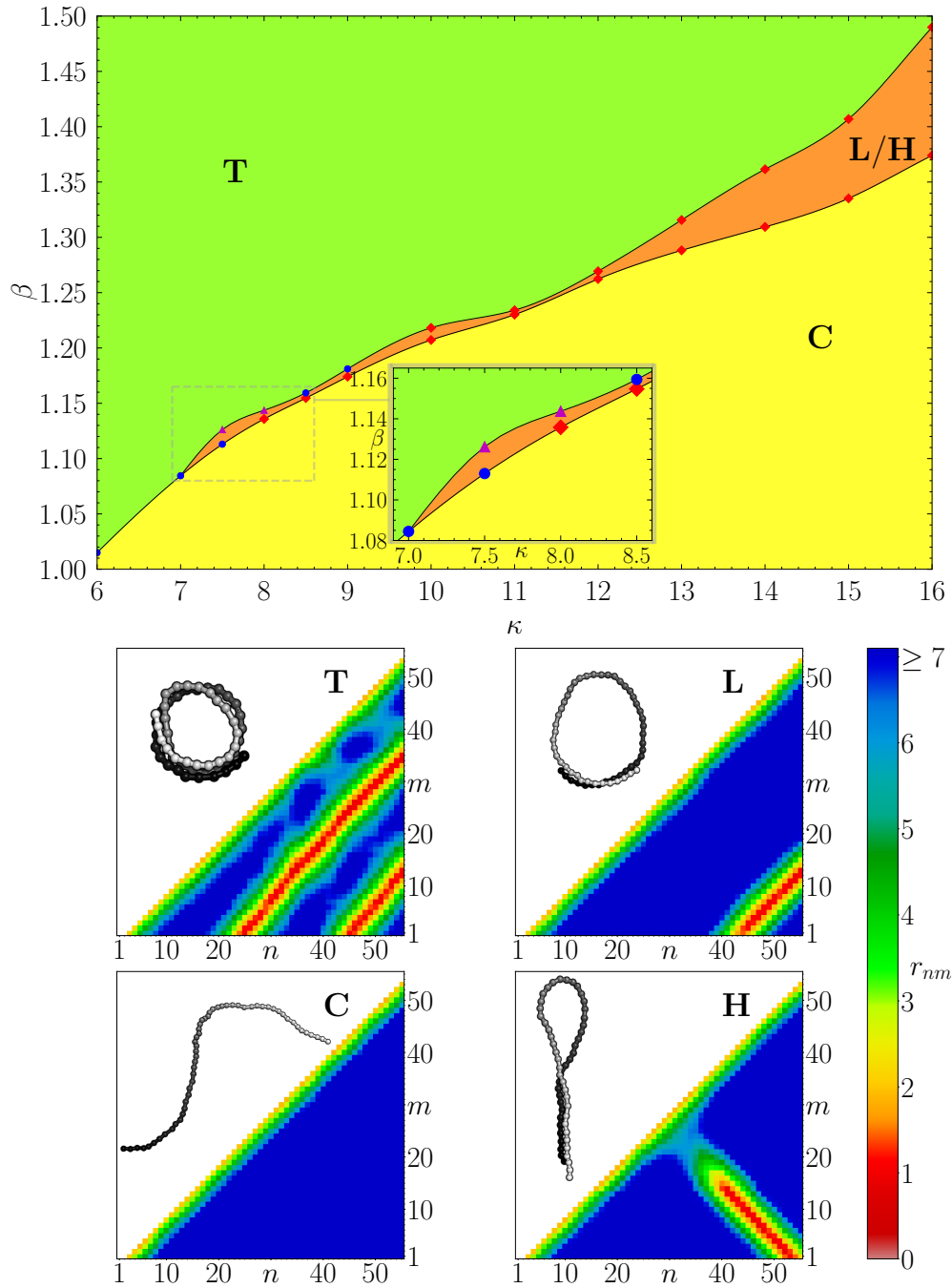


Figure 5.11: Hyperphase diagram for semiflexible polymers with 55 monomers, parametrized by bending stiffness κ and inverse microcanonical temperature β . Red diamonds mark first-order, blue dots second-order, and purple triangles third-order transitions. Solid transition lines are guides to the eye. Representative structures, characterizing the dominant types in the respective phases (C: wormlike random coils, H: hairpins, L: loops, T: toroids), and their distance maps (lower triangles in the insets) are also shown. Monomer labels are ordered from the black (first monomer) to the white end (last monomer).

as a black solid line, and the frequencies of different structures are shown in Fig. 5.12(b). The microcanonical Maxwell constructions on the backbending parts define the coexistence regions of first-order transitions. The two first-order transition regions are shaded gray. They have a clear energetic gap between them, confirming the hairpin-loop crossover phase is a stable intermediate phase. Not surprisingly, as shown in Fig. 5.12(c), the canonical energy probability distributions $P_{\text{can}}(E)$ for various canonical temperatures support our findings. The two noticeable suppressed regions are observed in the envelopes of these curves, which are typically caused by first-order transitions. They are located at the corresponding first-order transition regions that are indicated by the microcanonical inflection-point analysis. Interestingly, the curve of $\beta_{\text{can}} = 1.435$ spanned the whole energy range, and the effects of two first-order transitions are reflected by the two shoulders. This also helps explain the single peaks in canonical response quantities — the two transitions are too close to be distinguished by canonical analysis.

Moreover, not surprisingly, the comparison to the canonical average energy and the canonical heat-bath inverse temperature shows that the averaging process washes out the signals. As shown in Fig. 5.13, the fluctuations of the system energy in this region are relatively large to envelop the two first-order signals. Therefore, the canonical energetic quantities are not sensitive enough to differentiate the two signals.

At high energies, coil structures dominate the phase. Upon lowering the energy to the first transition point, there are mainly two options for the extended coils to fold and create tail contacts, parallel and antiparallel. In this transition, the presence of hairpins with antiparallel tail contacts rapidly increases. These conformations still provide sufficient entropic freedom for the dangling tail, which is already stabilized by van der Waals contacts, however. The loop part of the hairpin helps reduce the stiffness restraint. It is noteworthy that the pure loop structures with parallel tails also significantly contribute to the population, although at a lesser scale in this region. The actual crossover from hairpins to loops happens within the intermediate. For lower energies in this mixed phase, the population of hairpins decreases, whereas loops take over dominance.

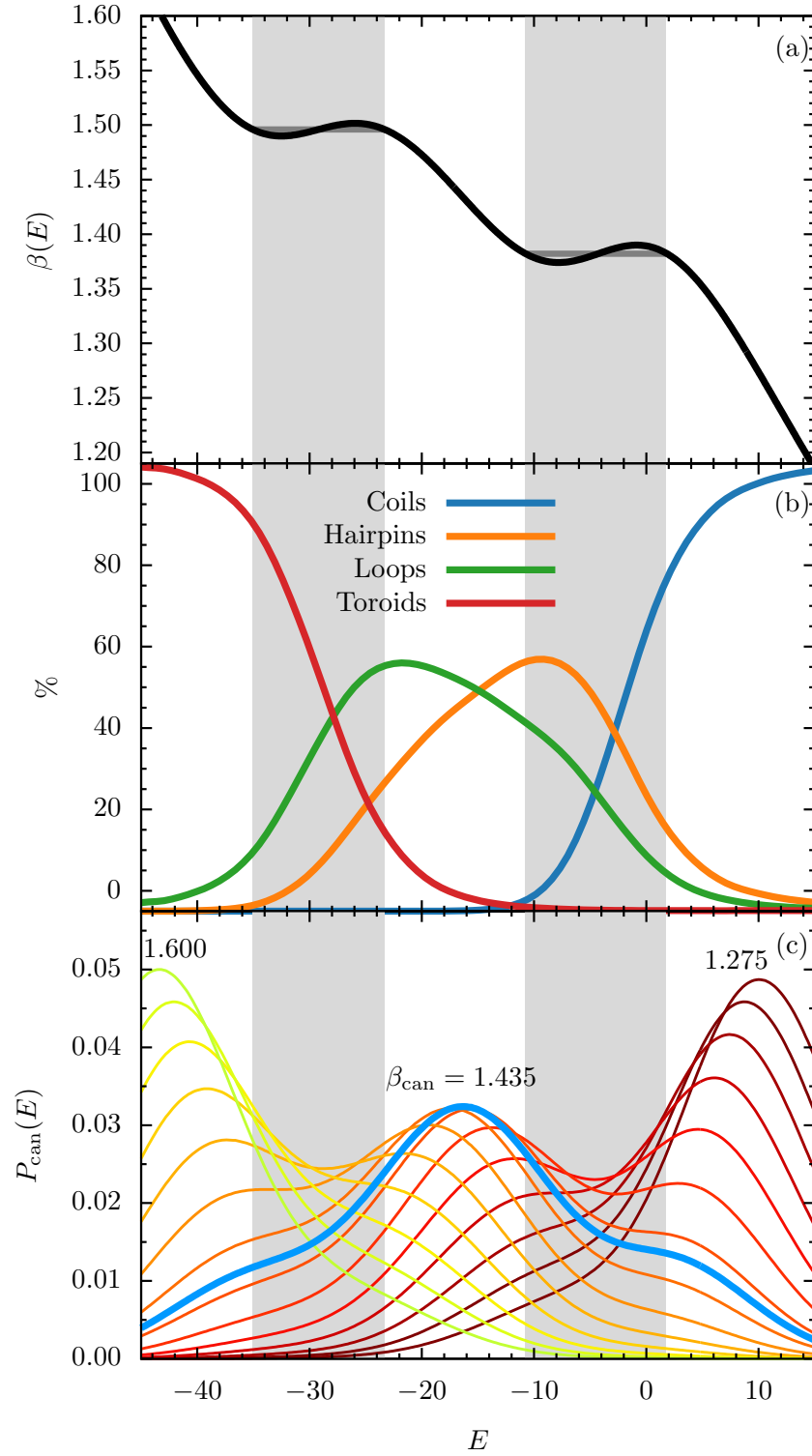


Figure 5.12: (a) Microcanonical temperature. (b) System energy dependence of frequencies for the different structure types at $\kappa = 16$. (c) Canonical energy probability distributions P_{can} at various inverse thermal energies $\beta_{\text{can}} = 1/k_B T_{\text{can}}$.

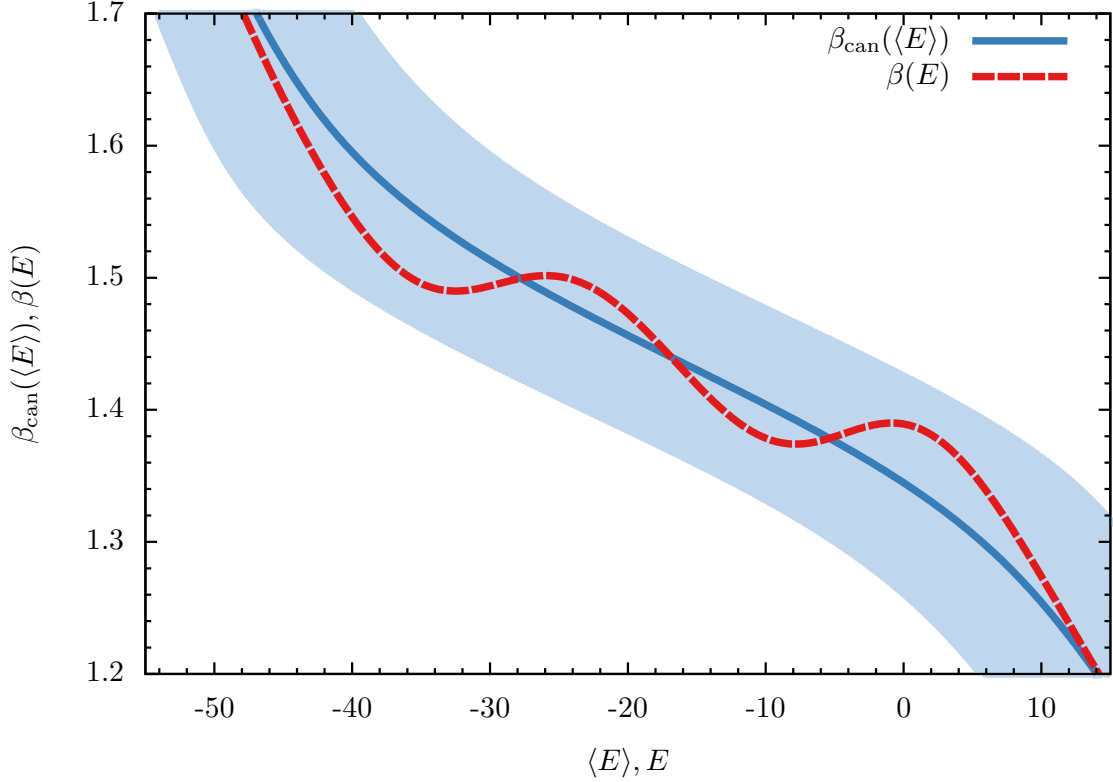


Figure 5.13: Comparison between canonical and microcanonical quantities for $N = 55, \kappa = 16$. The shaded area is the standard deviation of the system energy $\sigma(E)$, which represents the thermal fluctuations of the system energy E at the corresponding heat-bath temperature β_{can} .

Moreover, the energy difference between these two types of structures is zero or small enough so that the thermal fluctuations are still able to easily convert one to another by folding the tails back to or away from the loop part of the structures. This also explains why there is no phase transition between them. Importantly, even though hairpin and loop structures may be irrelevant at very low temperatures, they represent biologically significant secondary structure types at finite temperatures. The tail can be easily spliced, contact pair by contact pair, with little energetic effort, which supports essential micromolecular processes on the DNA and RNA level such as transcription and translation. Therefore, it is important to discern the phase dominated by these structures.

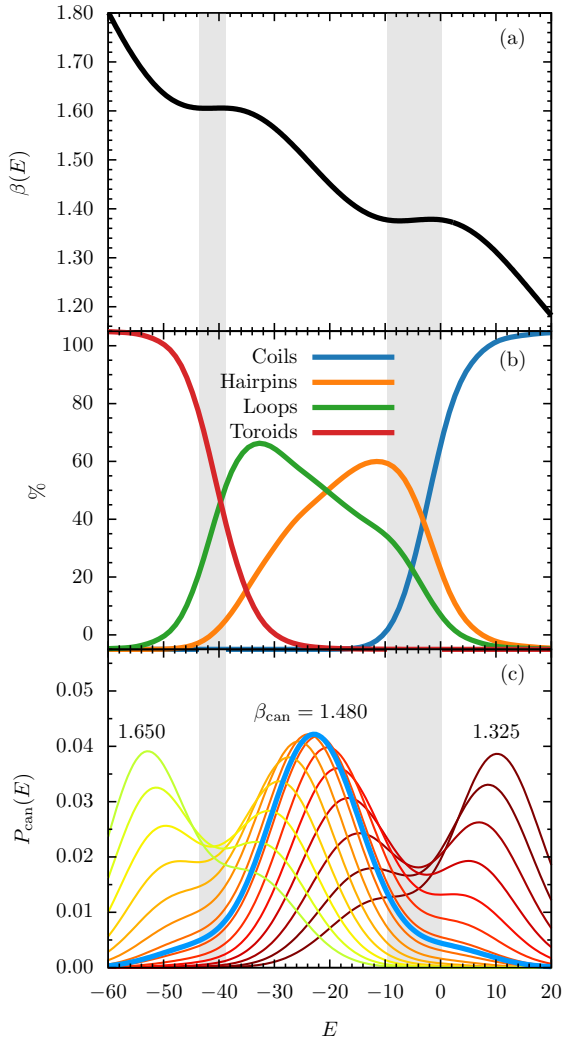
Upon further reducing the energy (and therefore also entropy), forming energetically favorable van der Waals contacts becomes the dominant structure formation strategy and loops coil in to

eventually form toroids. In contrast to loops, the structures are more ordered and they are stabilized further by additional energetically favorable attractions between monomers.

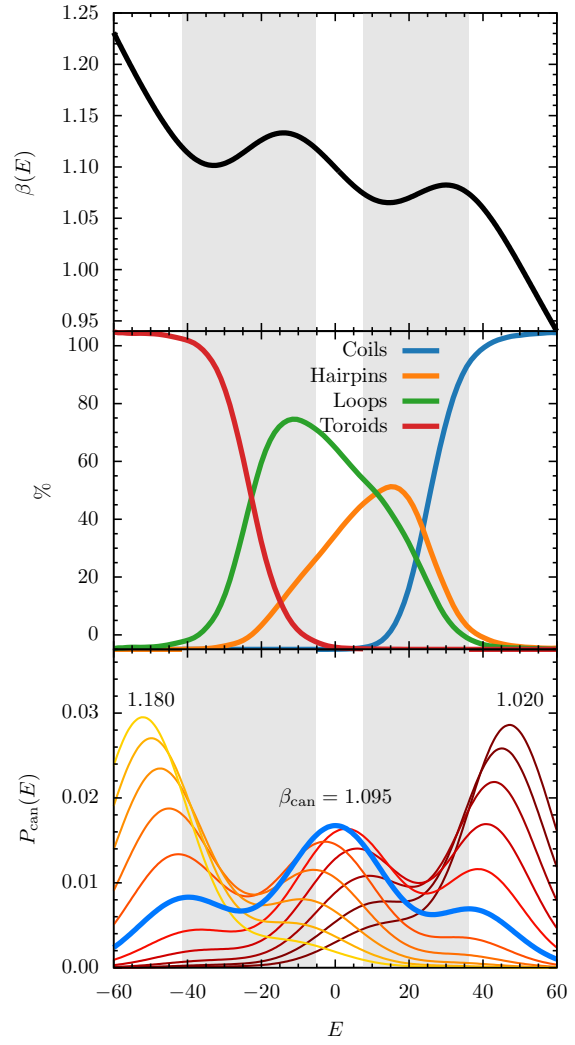
To test the robustness of the obtained results, we have also performed selected simulations of semiflexible chains of this generic model with 70 and 100 monomers. They essentially led to the same qualitative results, where the bifurcation of the collapse transition line is observed for these chain lengths. Quantitatively, we find a shift of the bifurcation point toward a higher bending stiffness. For $N = 70$, we found the bifurcation point to be close to $\kappa = 20$, whereas it is near $\kappa = 40$ for $N = 100$. This is expected, of course, as the number of possible energetic contacts scales with the number of monomers, which requires a larger energy penalty to break these contacts. It also helps understand why microbiological structures are not only finite but exist on a comparatively small, mesoscopic length scale. At the physiological scale, structure formation processes of large systems would be much more difficult to control and stabilize. This also means that studying such systems in the thermodynamic limit may not help in understanding physics at mesoscopic scales. Therefore, employing alternative statistical analysis methods as in this study is more beneficial than the application of conventional procedures, however successful they have been in studies of other problems. We also performed structure population analysis for the two first-order transitions in these two systems. The results for $(N = 70, \kappa = 30)$ and $(N = 100, \kappa = 45)$ are shown in Fig. 5.14. They both show the same crossover behavior of hairpins and loops in the intermediate phases as for $N = 55$. The two suppressed regions of canonical energy distribution probabilities are clearly visible as well. Hence, these results support the generality of our conclusions.

5.2 Analysis of Putative Ground-State Conformations

Biomolecules form distinct structures that allow them to perform specific functions in the physiological environment. Understanding the effects of the bending stiffness of these conformations is also crucial in many fields. In this section, we systematically study the competition between



$N = 70, \kappa = 30$



$N = 100, \kappa = 45$

Figure 5.14: Same as Fig. 5.12, but for $N = 70$ and $N = 100$.

attractive interactions, which usually are caused by hydrophobic van der Waals effects in solvent, and the impact of the bending stiffness on ground-state conformations with κ up to 19.

For the most part, the results are obtained from the parallel tempering and the extended two-dimensional replica-exchange methods that are described in previous chapters. In addition, global optimization methods such as Wang-Landau [114, 115], simulated annealing [116] and Energy Landscape Paving [117] were also used to verify and consolidate our results obtained from the replica exchange simulations. The exemplified simulations of these global optimization methods are illustrated in Fig. 5.15.

Energy Contributions

Putative ground-state conformations and their energies obtained from simulations for different choices of the bending stiffness κ are listed in Tab. 5.2. By increasing the bending stiffness κ , the semiflexible polymer folds into different classes of structures: compact globules ($\kappa < 5$), rod-like bundles ($5 \leq \kappa \leq 9$), as well as toroids ($\kappa > 9$). Here we first investigate the separate contributions from Lennard-Jones (LJ) and bending potentials to the total ground-state energies. Since bond lengths are at almost optimal distances ($\approx r_0$), the bonded potential V_{FENE} can be ignored in the following analysis. The main competition is between

$$E_{\text{LJ}} = \sum_{i>j} (V_{\text{LJ}}(r_{i,j}) - V_{\text{shift}}), \quad (5.1)$$

including contributions from bonded monomers, and the bending energy

$$E_{\text{bend}} = \sum_l V_{\text{bend}}(\theta_l). \quad (5.2)$$

We also introduce the renormalized contribution from the bending potential

$$\epsilon_{\text{bend}} = E_{\text{bend}}/\kappa \quad (5.3)$$

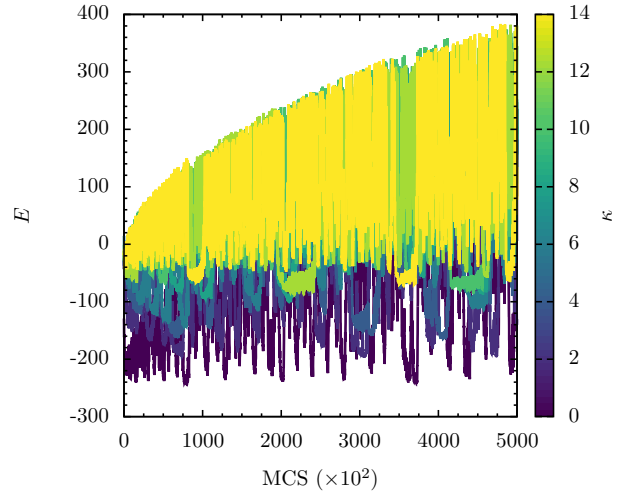
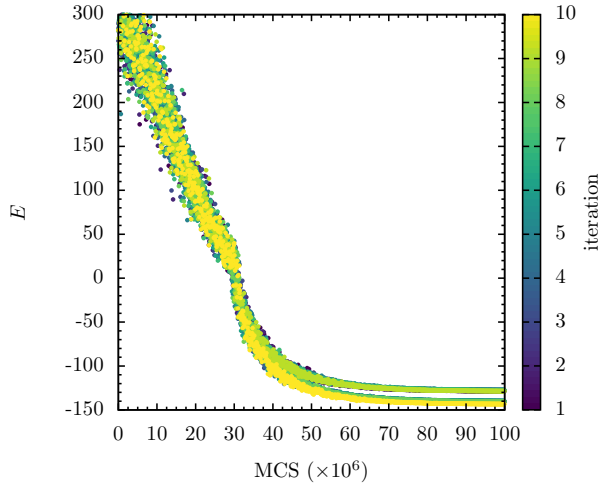
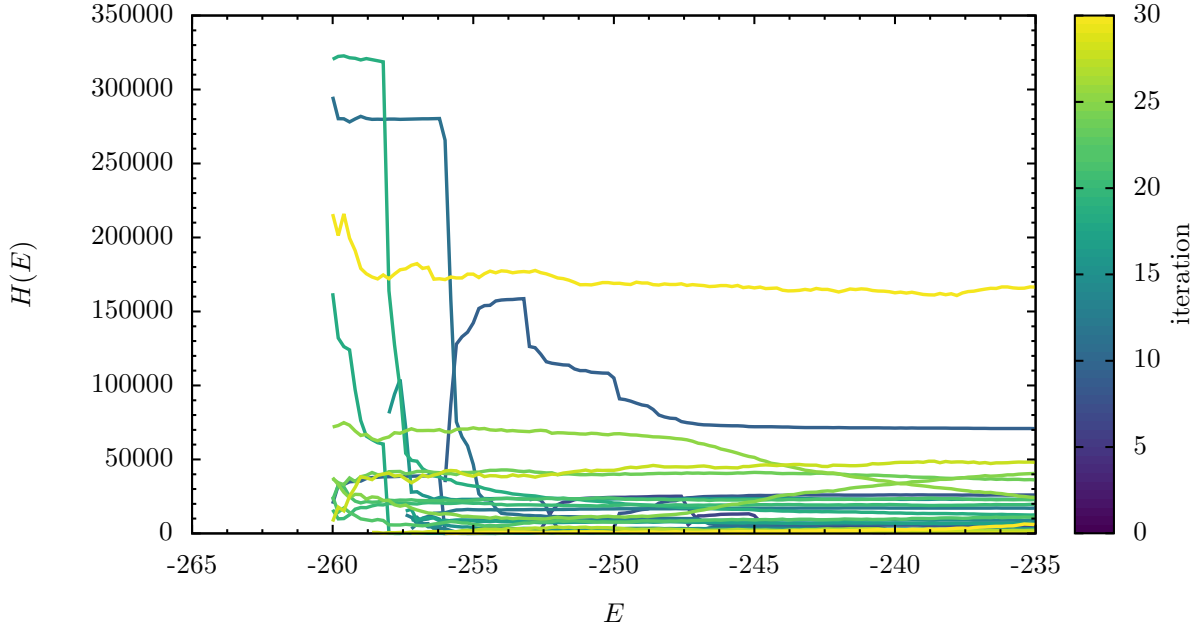
















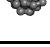

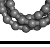



Figure 5.15: Exemplified global optimization simulations of selected κ values for a generic semi-flexible polymer model.

Table 5.2: Lowest-energy conformations and corresponding energy values obtained from simulations for the selected values of the bending stiffness ranging from $\kappa = 0$ (fully flexible) to $\kappa = 19$.

κ	Structure	E/ϵ_{LJ}	κ	Structure	E/ϵ_{LJ}	κ	Structure	E/ϵ_{LJ}	κ	Structure	E/ϵ_{LJ}
0		-261.72	5		-175.70	10		-132.42	15		-110.60
1		-230.93	6		-166.53	11		-128.23	16		-107.60
2		-222.80	7		-157.49	12		-124.24	17		-104.67
3		-204.82	8		-146.98	13		-120.51	18		-100.98
4		-187.33	9		-140.14	14		-116.71	19		-97.92

for studying the relative impact of bending on the ground-state conformations.

The energies E , E_{LJ} , bending energy E_{bend} , and renormalized bending quantity ϵ_{bend} are plotted for all ground-state conformations in Fig. 5.16. Not surprisingly, the total energy E increases as the bending stiffness κ increases. Similarly, E_{LJ} also increases with increased bending stiffness κ , but rather step-wise. Combining these trends with the corresponding structures, it can be concluded that each major global change in ground-state conformations with increased bending stiffness leads to the reduced attraction between monomers (increase in E_{LJ}). Whereas the bending energy E_{bend} does not exhibit specific trend, the renormalized bending energy ϵ_{bend} decreases step-wise as well for increased bending stiffness κ , as shown in Fig. 5.16(b). It is more interesting, though, to see there are clear alterations of E_{LJ} and ϵ_{bend} within the same structure type (compact globules, rod-like bundles, or toroids). Moreover, most of the locations of rapid changes are the same for both E_{LJ} and ϵ_{bend} , indicating that the structural changes affect both attraction and bending. For $\kappa = 0, 1$ and 2 , the overall attraction E_{LJ} does not change much, in contrast to ϵ_{bend} , suggesting that the polymer chain is able to accommodate the bending penalty without affecting energetically favorable monomer-monomer contacts.

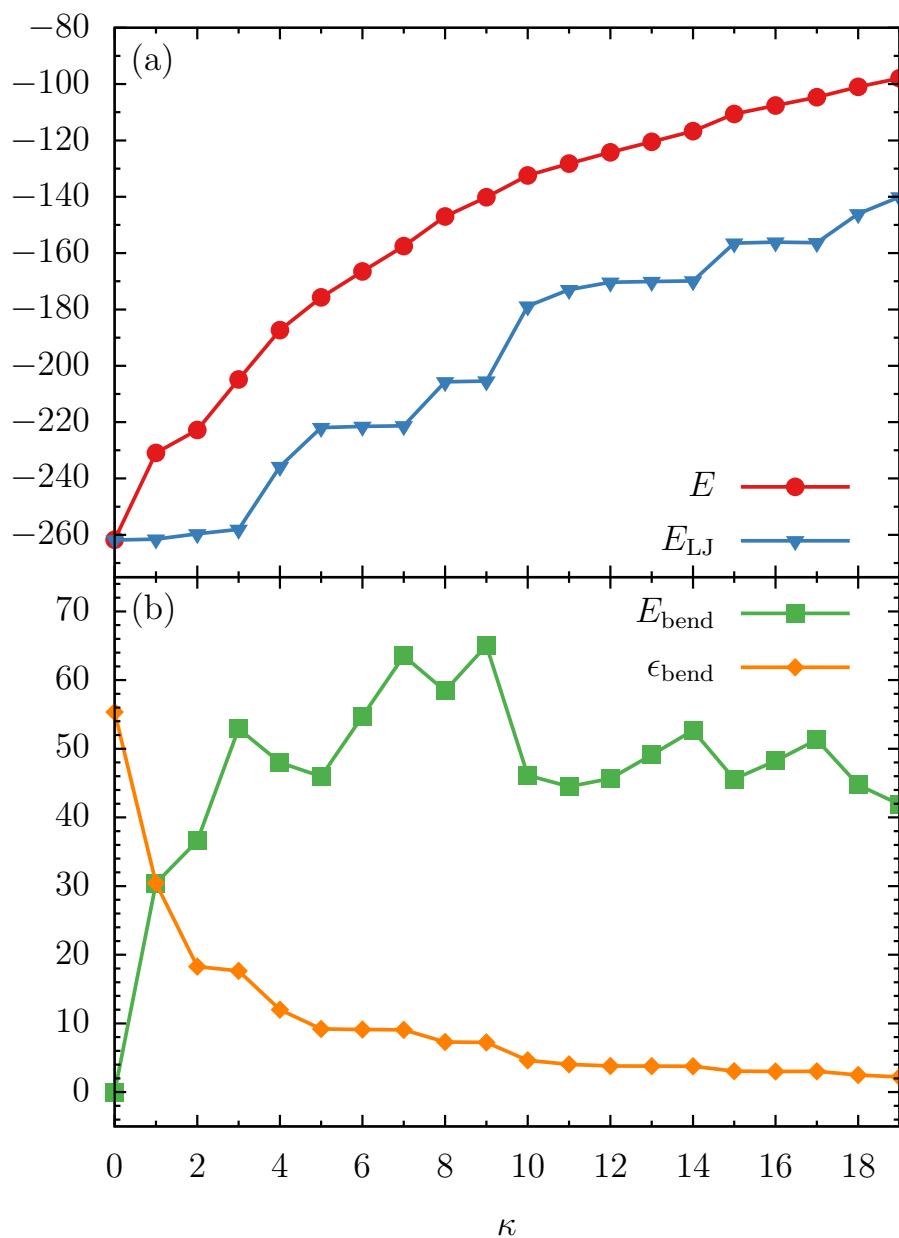


Figure 5.16: (a) Total energy E and Lennard-Jones contribution E_{LJ} of ground-state conformations. (b) Total bending energy E_{bend} and renormalized bending contributions $\epsilon_{\text{bend}} = E_{\text{bend}}/\kappa$ for the entire array of κ parameter values simulated.

Even though the energetic analysis provides more information about the competition between different energetic terms, conclusions about the structural behavior are still qualitative. Therefore, a more detailed structural analysis is performed in the following.

Gyration Tensor Analysis

In order to provide a quantitative description of the structural features, we calculated the gyration tensor S for the ground-state conformations with components

$$S_{\alpha,\beta} = \frac{1}{N} \sum_{i=1}^N (r_{\alpha}^{(i)} - r_{\alpha}^{\text{CM}}) (r_{\beta}^{(i)} - r_{\beta}^{\text{CM}}), \quad (5.4)$$

where $\alpha, \beta \in \{x, y, z\}$ and $\mathbf{r}^{\text{CM}} = \frac{1}{N} \sum_{j=1}^N \mathbf{r}_j$ is the center of mass of the polymer. After diagonalization, S can be written as

$$S_D = \begin{pmatrix} \lambda_x^2 & 0 & 0 \\ 0 & \lambda_y^2 & 0 \\ 0 & 0 & \lambda_z^2 \end{pmatrix}, \quad (5.5)$$

where the eigenvalues are principal moments and ordered as $\lambda_x^2 \leq \lambda_y^2 \leq \lambda_z^2$. These moments describe the effective extension of the polymer chain in the principal axial directions. Thus, different invariant shape parameters can be derived from combinations of these moments. Most commonly used for polymers, the square radius of gyration R_{gyr}^2 is obtained from the summation of the eigenvalues:

$$R_{\text{gyr}}^2 = \lambda_x^2 + \lambda_y^2 + \lambda_z^2. \quad (5.6)$$

The radius of gyration describes the overall effective size of a polymer conformation. In addition, another invariant shape parameter we employed is the relative shape anisotropy A , which is defined

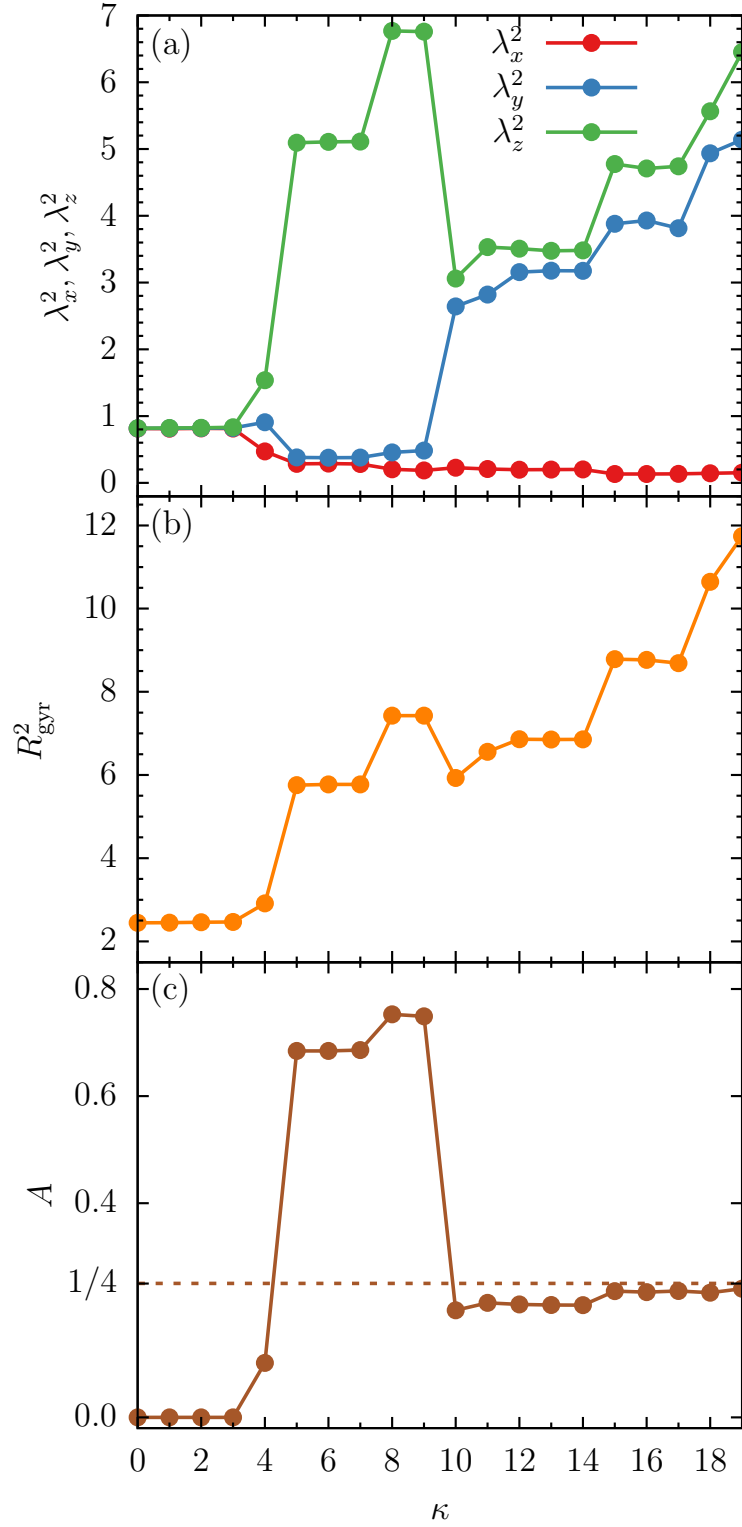


Figure 5.17: **(a)** Square principal moments $\lambda_x^2, \lambda_y^2, \lambda_z^2$ from the diagonalized gyration tensor S , **(b)** square radius of gyration R_{gyr}^2 , **(c)** and relative shape anisotropy A for ground-state conformations on a large array of κ values.

as

$$A = \frac{3}{2} \frac{\lambda_x^4 + \lambda_y^4 + \lambda_z^4}{(\lambda_x^2 + \lambda_y^2 + \lambda_z^2)^2} - \frac{1}{2}. \quad (5.7)$$

It is a normalized parameter, the value of which is limited to between 0 and 1, where $A = 0$ is associated with spherically symmetric polymer chains ($\lambda_x = \lambda_y = \lambda_z$), and $A = 1$ is the limit for the perfectly linear straight chain ($\lambda_x = \lambda_y = 0, \lambda_z > 0$). Other than these two limits, $A = 1/4$ refers to perfectly planar conformations ($\lambda_x = 0, 0 < \lambda_y = \lambda_z$). The calculated values of square principal components $\lambda_x^2, \lambda_y^2, \lambda_z^2$, square radius of gyration R_{gyr}^2 , and the relative shape anisotropy A of ground-state conformations are plotted in Fig. 5.17 as functions of κ .

Starting with $\kappa = 0, 1, 2$ and 3, the three principal moments of the corresponding lowest-energy conformations are small and nearly equal. These are the most compact conformations we found. For these structures, $A < 10^{-3}$. This is obvious from the dense globular structures shown in Tab. 5.2. Furthermore, it means that for relatively small κ values, semiflexible polymer conformations maintain compact spherical symmetry at low temperatures, similar to purely flexible polymers. The ground-state structures have icosahedral-like symmetry. For this we take a look at the pair distribution functions. Using the distance $r_{i,j}$ of monomers i and j , we introduce the pair distribution function as

$$P(r) = \sum_{i < j} \Delta(r - r_{i,j}), \quad (5.8)$$

where

$$\Delta(r - r_{i,j}) = \begin{cases} 1, & |r - r_{i,j}| < r_t, \\ 0, & \text{otherwise.} \end{cases} \quad (5.9)$$

As a robust threshold for the necessary binning of the r space, we chose $r_t = 0.01$. The histograms for the lowest-energy conformations for $\kappa = 0, 1, 2, 3$ are plotted in Fig. 5.18. The perfect icosahedral structure is only found for $\kappa = 0$, whereas its decay is already visible for the weaker semiflexible polymer ($\kappa = 1$). The maximum number of nearest-neighbor contacts ($r_{i,j} \approx 1$) found for $\kappa = 0$ is not reached in the semiflexible cases. The broadening of the peaks

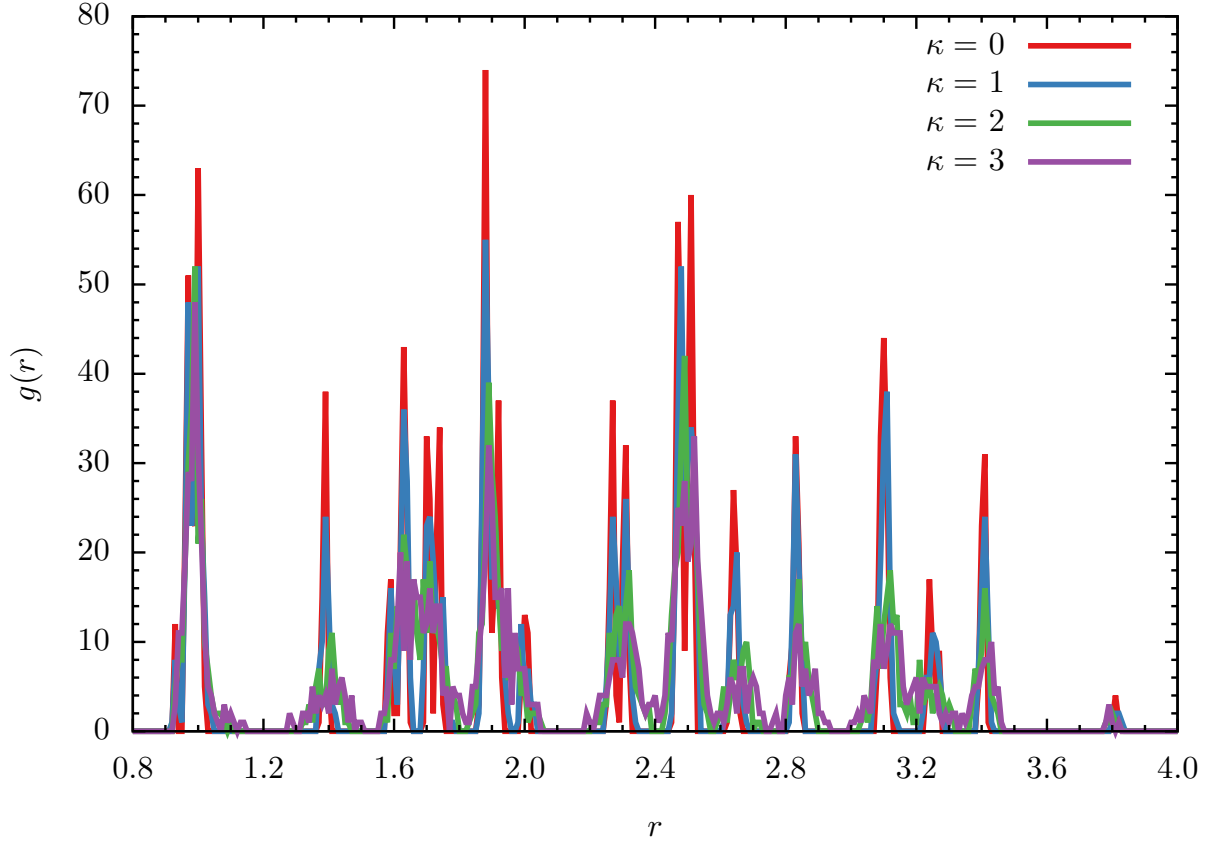


Figure 5.18: Pair distribution functions of the lowest-energy states for $\kappa = 0, 1, 2, 3$.

are clear indicators that the ground-state structures for the semiflexible polymer with $\kappa = 1, 2, 3$ are not perfect icosahedral. Bending restraints prevent the formation of perfect symmetries. It rather resembles tertiary folds of protein conformations, where effective bending restraints and the local stable secondary segments purposefully prevent symmetric arrangements of monomers. This enables different heteropolymers of similar size to form distinct and functional individual conformations.

Going back to the gyration tensor analysis, the increased bending stiffness for $\kappa = 4$ breaks the symmetry of the compact structures and ground-state conformations stretch out. This is reflected by the imbalance of the principal moments. Consequently, A is nonzero. Besides, the overall size of the conformations becomes larger as R_{gyr}^2 suggests.

If the bending stiffness is increased to $\kappa = 5, 6$ and 7 , rod-like structures are formed with 7 bundles to minimize the total energy. One principal moment increases dramatically while the other two moments decrease. As a result, R_{gyr}^2 reaches a higher level, but remains almost constant. The relative shape anisotropy climbs to $A \approx 0.69$, indicating that the shape straightens out further.

The number of bundles reduces to 6 for $\kappa = 8$ and 9 , resulting in longer rod-like structures. Both R_{gyr}^2 and A increase further, the change of which is not visually obvious in Tab. 5.2, though.

With the bending energy being even more dominant for $10 \leq \kappa \leq 14$, the appearance of conformations changes significantly. The condensed toroidal structures with up to 4 windings are energetically more favored than rod-like bundles. Instead of having a few sharp turns like rod-like bundles to accommodate the bending penalty, the semiflexible polymer chain forms a dense toroidal structure. Successive bending angles are comparatively small. In this case, the two largest principal moments converge to an intermediate value. As a consequence of the more compact structures, R_{gyr}^2 decreases with increased bending stiffness. The asphericity A also drops below the characteristic limit $1/4$, reflecting the planar symmetry of the toroidal structures.

It becomes more difficult for the polymer in the ground state to maintain the same small bending angles for increased bending stiffness values $\kappa = 15, 16$ and 17 . As a result, the smaller bending angles form similar toroidal structures as in the previously discussed case, but with a larger radius and fewer windings. Therefore, two main principal moments increase, as well as R_{gyr}^2 . Meanwhile, the relative shape anisotropy A approaches $1/4$. Fewer windings reduce the overall thickness in the normal direction of the toroidal conformations. As can be seen from the conformations in Tab. 5.2, these structures are stabilized by the attraction of close end monomers.

However, for $\kappa > 17$, the attraction of two end monomers is not sufficient to sustain the structure. Thus, expanding the toroid becomes an advantageous option to offset strong bending penalties. The toroidal structure is stretched out, which is clearly seen in Tab. 5.2 for $\kappa = 18$ and 19 . The radius of the toroid keeps getting larger, so does R_{gyr}^2 . It is expected that for much stronger bending stiffness,

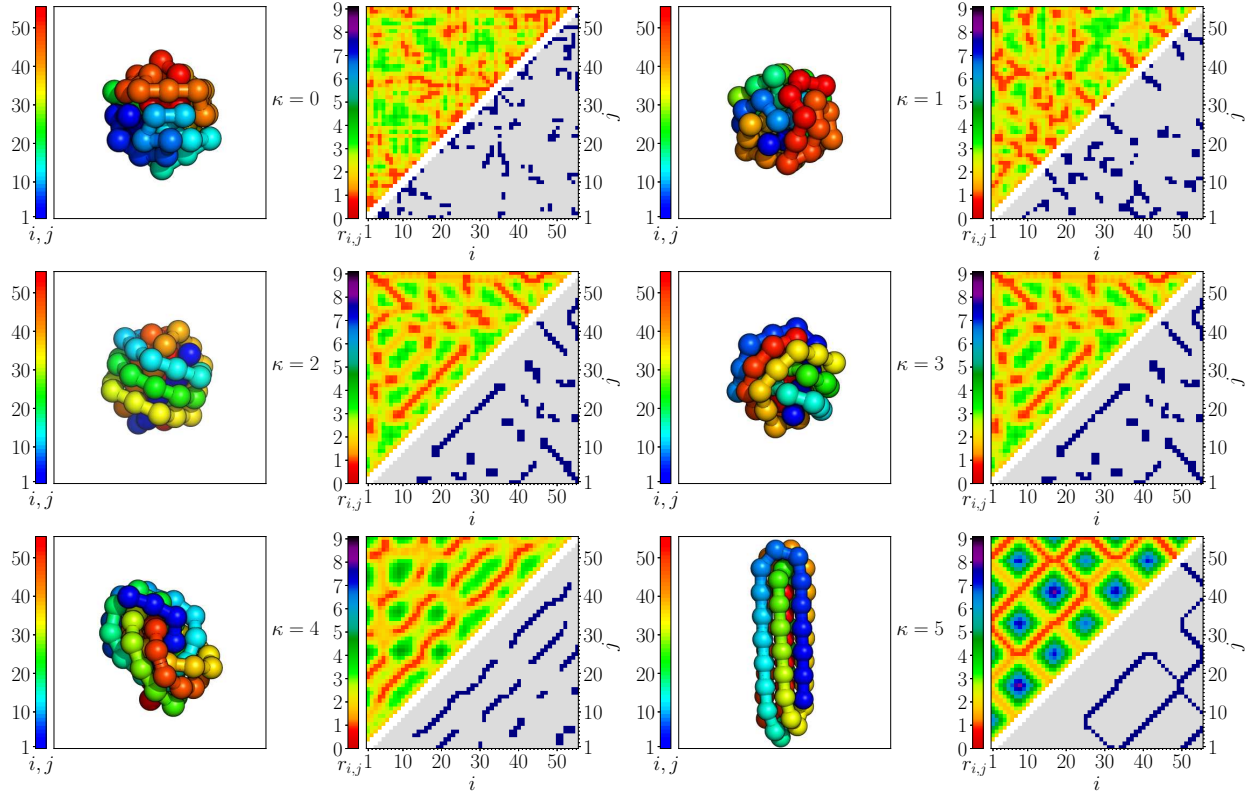


Figure 5.19: Representations of ground-state conformations (left panel) and their contact maps (right) for $\kappa \leq 5$. The upper triangle contains the monomer distance map, where the distance $r_{i,j}$ of monomers i and j is colored. The contact map is shown in the lower triangle. Monomers i and j are in contact if $r_{i,j} < 1.2$.

the polymer chain would form a large circular loop with fewer windings. We find that A keeps converging to the planar symmetry limit of $1/4$.

Contact Map Analysis

Even though the previous gyration tensor analysis yields a reasonable quantitative description of the overall structural properties of the ground-state conformations, it does not provide insight into internal ordering of structures, neither the pair distributions. Therefore, we now perform a more detailed analysis by means of monomer distance maps and contact maps.

To find the relative monomer positions, we measured the monomer distance $r_{i,j}$ between monomers i and j for all monomer pairs. Furthermore, we consider nonbonded monomer pairs

with distances $r_{i,j} < 1.2$ to be in contact. The limit is close to the minimum distance r_0 of the Lennard-Jones potential, allows distinguishing unique contact features of conformations while avoiding counting nonnearest-neighbor contacts. In the figures, we colored the monomers from one end to the other to make the polymer chain orientation more easily visible.

The combined results for $\kappa \leq 5$ are shown in Fig. 5.19. For $\kappa = 0$ (flexible polymer), the structure is icosahedral, and the maps do not exhibit particularly remarkable structural features. Without the energetic penalty from bending, maximizing the number of nearest neighbors is the optimal way to gain energetic benefit. For $\kappa = 1$, the introduced small bond angle restraint already starts affecting the monomer positions. In the contact map, short anti-diagonal streaks start appearing, which indicate the existence of short hairpins, i.e., a U-turn like structure with two strands in contact. Interestingly, we find similar conformations for $\kappa = 2$ and $\kappa = 3$, as confirmed by similar distance and contact maps. There are fewer, but longer anti-diagonal strands, located in the interior of the compact structure. The formation of new streaks parallel to the diagonal is associated with the helical wrapping of monomers, which is visible in the colored representations. As for $\kappa = 4$, the ground-state conformation is the compromise of two tendencies. The bending stiffness neither is weak, as for $\kappa = 3$ the semiflexible polymer is still able to maintain a spherical compact structure with more turns, nor is it particularly strong as for $\kappa = 5$, where the polymer forms a rod-like bundle structure. Therefore, the lowest-energy conformations shown in Fig. 5.19 contain only helical turns trying to minimize the size, as indicated by several diagonal streaks in the contact map. For $\kappa = 5$, the polymer mediates the bending penalty by allowing only a few sharp turns between the rods. For the 7-bundle structure, the randomness completely disappears in both distance and contact maps. The blue square areas in the distance map mark the separation of monomer groups belonging to the two ends of the bundle structure. Furthermore, the diagonal streaks indicate the contact of two parallel bundles while the turns of the chain form anti-diagonal streaks. It is also worth mentioning that in this case the two end-monomers are located on opposite sides.

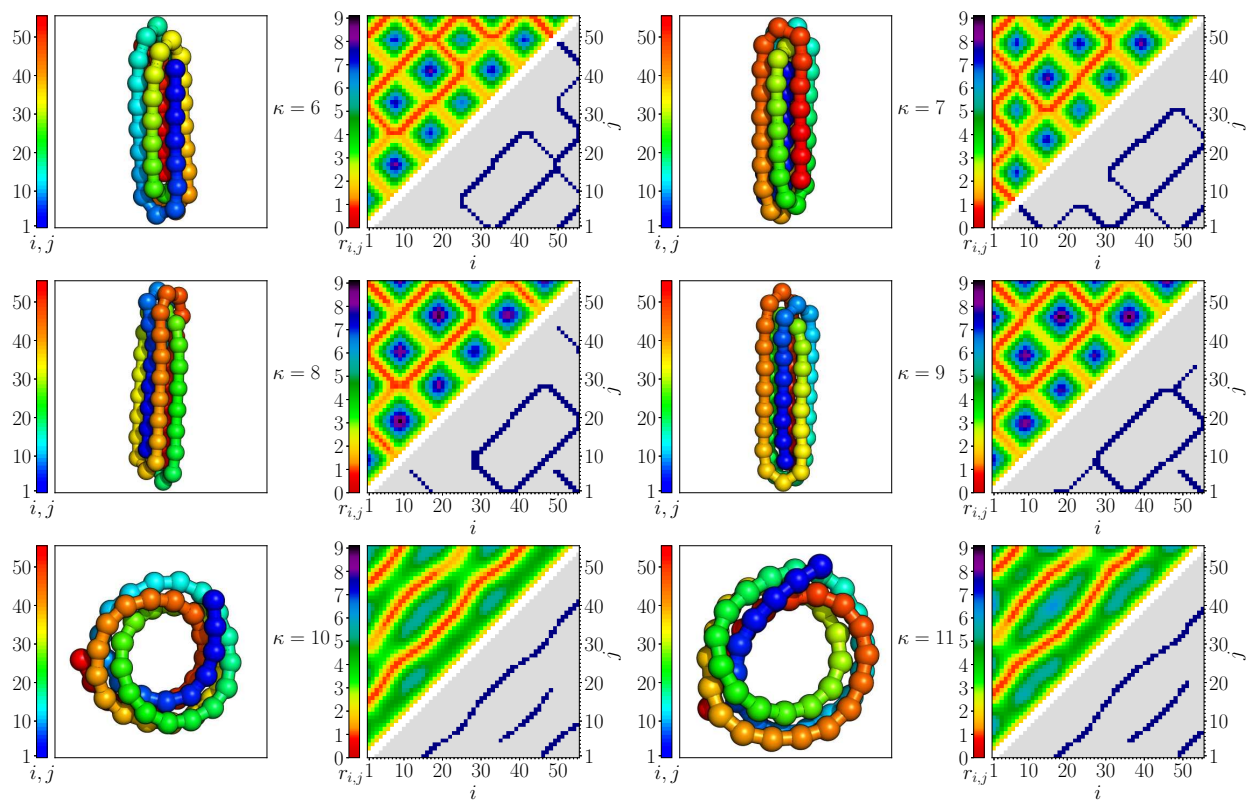


Figure 5.20: Same as Fig. 5.19, but for $6 \leq \kappa \leq 11$.

The results for $6 \leq \kappa \leq 11$ are shown in Fig. 5.20. Similar to $\kappa = 5$, the polymer still forms a 7-bundle rod-like structure for $\kappa = 6$ and $\kappa = 7$. The anti-diagonal symmetry in maps for $\kappa = 6$ and $\kappa = 7$ is only a consequence of opposite indexing of monomers. For $\kappa = 8$ and $\kappa = 9$, the increased bending stiffness leads to a decrease in the number of sharp turns from 7 to 6, where the two end monomers are now located on the same side. The relative positions of monomers are almost identical for $\kappa = 8$ and $\kappa = 9$ as seen in their distance maps. However, the difference in contact maps is caused by the way the straight rods are aligned after the sharp turns. For $\kappa = 8$, four monomers (the orange turn in the colored presentation in Fig. 5.20 for $\kappa = 8$) form the sharp turn. This allows the rods to align closer compared to the $\kappa = 9$ case, where only 3 monomers are located in the turn that holds two parallel rods (blue color). For $\kappa = 10, 11$, the optimal way to pack monomers is by toroidal wrapping. Thus, the contact maps exhibit only 3 diagonal streaks.

Results for $\kappa \geq 11$ are shown in Fig. 5.21. Contact maps for $\kappa = 12, 13$ and 14 still feature three diagonal streaks. However, for $\kappa = 15, 16$, and 17 , the increased bending stiffness causes a larger radius of the toroidal structure and the two end monomers are stabilized by Lennard-Jones attraction. Thus, the number of parallel diagonals reduces to two and the attraction of two end monomers is marked in the corners of the maps. Finally, for polymers with even larger bending stiffness, i.e., $\kappa = 18$ and $\kappa = 19$, the attraction of the two monomers breaks and the whole structure stretches out even more. As a result, the distance map for $\kappa = 19$ contains extended sections of increased monomer distances. At the same time, the contact map still shows two streaks slightly shifted to the right, indicating a reduction in the number of contacts.

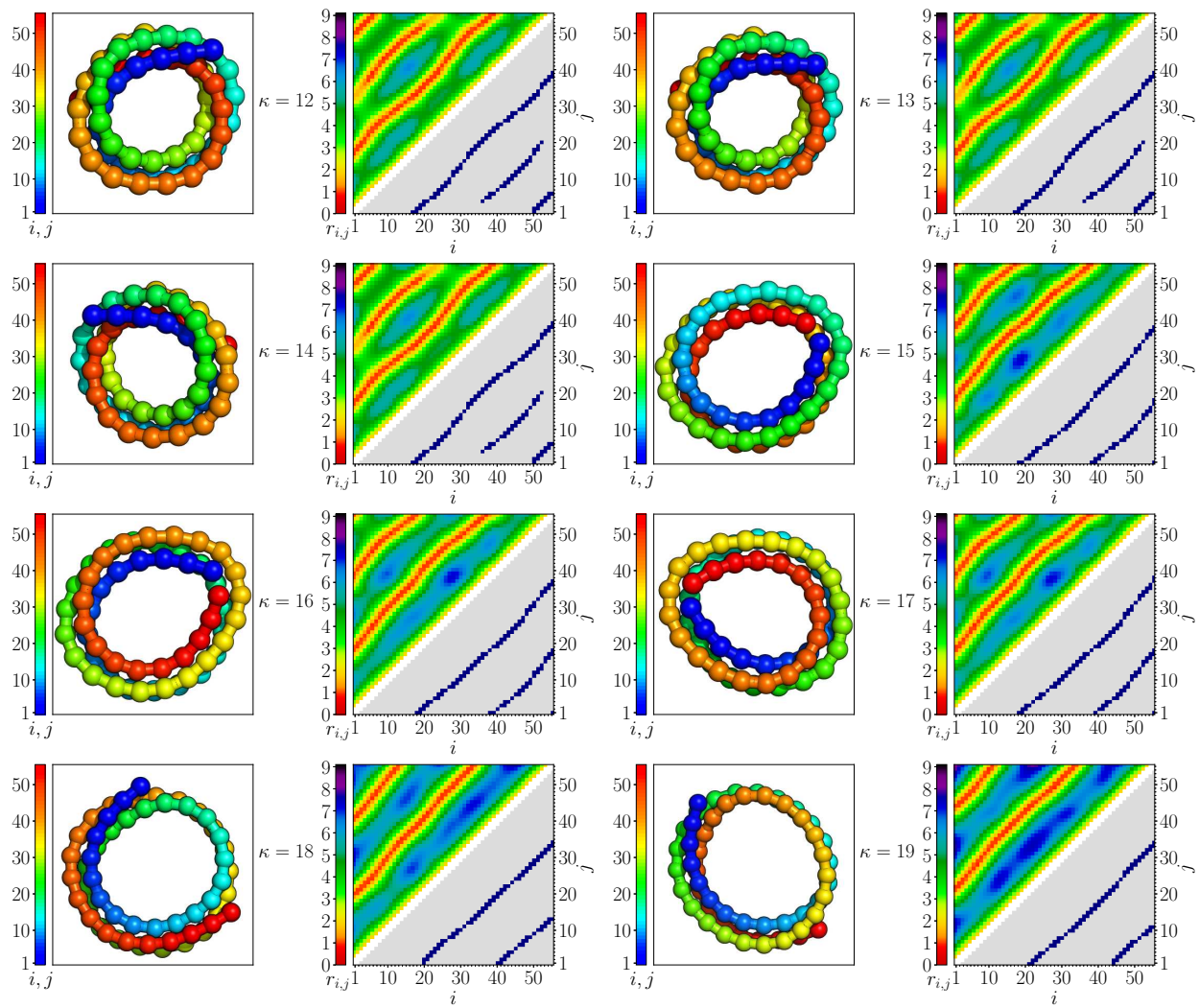


Figure 5.21: Same as Fig. 5.19, but for $\kappa \geq 11$.

CHAPTER 6

SUMMARY

The statistical analysis of structural transitions by the recently developed generalized microcanonical inflection-point method had already yielded promising results in studies of flexible polymers. For this study, we extended the coarse-grained model by incorporating bending restraints of different strengths to investigate the impact of bending stiffness on the microcanonical entropy and its derivatives, which are used as indicator functions for the systematic identification and classification of phase transitions in systems of any size. In this coarse-grained model for semiflexible polymers, the bending restraint is controlled by the bending stiffness parameter κ .

Despite its simplicity, the model required careful numerical treatment. For this purpose, we successfully employed parallelized replica-exchange Monte Carlo methods and especially extended the simulation parameter space from heat-bath temperature to the combined space of temperature and bending stiffness. Besides, the combination of geometric and energy methods worked well to obtain optimal temperature sets, which has been an obstacle to general parallel tempering simulations. In addition, we have also successfully implemented advanced Monte Carlo moves in these simulations to improve the simulation efficiency. Microcanonical entropies and their derivatives were obtained by applying the Bézeier method on the density of states, which are the main output of the multiple-histogram reweighting method applied to the raw simulation data.

Based on the microcanonical results obtained in the simulations, we compared the phase behavior of the model under different bending stiffness values. Our simulations reproduced previous results for the flexible ($\kappa = 0$) reference system very well, creating sufficient confidence for the subsequent studies of the semiflexible polymers. Because of the additional restraints, it was significantly more challenging to achieve in simulations of semiflexible polymers the data quality necessary to enable an accurate microcanonical analysis.

For the flexible polymer, we identified the known structural transitions, i.e., the characteristic second-order transition associated with the θ collapse from extended random coils to liquid globules and the first-order liquid-solid transition, which is accompanied by an independent third-order transition. For nonzero bending stiffness values ($\kappa > 0$), we mainly focused on the collapse transition in these systems. The behavior does not change qualitatively for the Θ collapse transition for bending stiffness up to $\kappa \approx 7$, where both canonical and microcanonical canonical quantities confirmed a single second-order transition. However, we have found the bifurcation of the second-order collapse transition line, which surprisingly developed into two first-order transition lines. The bifurcation is not visible in canonical analysis, though. Neither canonical energetic nor structural fluctuation quantities hint at the existence of two clearly separated transitions for semiflexible polymers, which we could identify by microcanonical inflection-point analysis. Conventional canonical analysis is too rugged – the intermediate phase is simply washed out in the averaging process. This should be considered a problem, particularly when standard canonical analysis methods are employed in studies of finite systems. In the generic model for semiflexible polymers used in our study, the intermediate phase accommodates loop and hairpin structures, which are found in biomacromolecular systems including types of DNA and RNA.

In this study, we have also examined the effect of bending stiffness on the ground-state conformations of our model. The bending stiffness significantly influences the formation of low-energy structures for semiflexible polymers. Varying the bending stiffness parameter in our model results in shapes like compact globules, rod-like bundles, and toroids with abundant internal arrangements.

The estimates of the ground-state energies are from the extended replica exchange Monte Carlo simulations and the results are verified utilizing global optimization algorithms, e.g., Wang-Landau sampling. We find that the semiflexible polymer folds into compact globules for relatively small bending stiffness, rod-like bundles for intermediate bending strengths, as well as toroids for sufficiently large bending restraints. Eventually, we performed energetic and structural analyses to study the impact of the bending stiffness on the formation of ground-state structures. We decomposed the energy contributions to gain more insight into the competition between attractive van der Waals forces and the bending restraint. The total energy of ground-state conformations increases smoothly with increased bending stiffness, but not the attraction and bending potentials. Interestingly, renormalizing the bending energy reveals that local bending effects of ground-state conformations actually reduce for increased bending stiffness. The structural analysis by means of gyration tensor and invariant shape parameters provided a general picture regarding the size and shape changes of conformations under different bending restraints. In a further step, studying distance maps and contact maps exposed details of internal structure ordering and helped distinguish conformations, especially for small values of the bending stiffness, where the gyration tensor analysis has been inconclusive. Contact map analysis also caught slight differences, where different structure types are almost degenerate.

To conclude, bending stiffness is not only a necessary property of polymers in the formation of distinct and biologically relevant structures at finite temperatures; it also stabilizes the phase dominated by these structure types in a thermal environment, where entropy and energy effectively compete with each other. Regarding the low energy states, semiflexible polymer structures remain stable within a certain range of bending strengths, which makes them obvious candidates for functional macromolecules. Monomer-monomer attraction provides stability and bending stiffness adaptability to allow semiflexible polymers to form distinct structures. Neither flexible polymers nor crystalline structures would be equally adaptable and stable like semiflexible polymers are under diverse physiological conditions. This is fully compliant with Nature's governing principle,

in which sufficient order is provided to enable the formation of stable mesostructures, but at the same time, enough disorder allows these structures to explore variability. This makes them functional in a stochastic, thermal environment, with sufficient efficiency enabling lifeforms to exist and survive under these conditions.

BIBLIOGRAPHY

- [1] P. Ehrenfest, *Phasenumwandlungen im ueblichen und erweiterten Sinn, classifiziert nach den entsprechenden Singularitaeten des thermodynamischen Potentials* (NV Noord-Hollandsche Uitgevers Maatschappij, 1933).
- [2] L. P. Kadanoff, W. Götze, D. Hamblen, R. Hecht, E. Lewis, V. V. Palciauskas, M. Rayl, J. Swift, D. Aspnes, and J. Kane, *Rev. Mod. Phys.* **39**, 395 (1967).
- [3] H. E. Stanley, *Phase transitions and critical phenomena*, Vol. 7 (Clarendon Press, Oxford, 1971).
- [4] M. E. Fisher, S.-k. Ma, and B. Nickel, *Phys. Rev. Lett.* **29**, 917 (1972).
- [5] M. E. Fisher and M. N. Barber, *Phys. Rev. Lett.* **28**, 1516 (1972).
- [6] M. E. Fisher, *Rev. Mod. Phys.* **46**, 597 (1974).
- [7] K. Binder and D. Landau, *Phys. Rev. B* **30**, 1477 (1984).
- [8] D. P. Landau and K. Binder, *A Guide to Monte Carlo Simulations in Statistical Physics* (Cambridge University Press, July 29, 2021), 583 pp.
- [9] E. Ising, “Beitrag zur theorie des ferro-und paramagnetismus”, PhD thesis (Grefe & Tiedemann Hamburg, 1924).
- [10] D. H. E. Gross, *Microcanonical Thermodynamics: Phase Transitions in "Small" Systems* (World Scientific, 2001), 287 pp.
- [11] P. M. Stevenson, *Phys. Lett. B* **100**, 61 (1981).

- [12] P. M. Stevenson, Phys. Rev. D **23**, 2916 (1981).
- [13] K. Qi and M. Bachmann, Phys. Rev. Lett. **120**, 180601 (2018).
- [14] O. Kratky and G. Porod, Recl. Trav. Chim. Pays-Bas **68**, 1106 (1949).
- [15] D. T. Seaton, S. Schnabel, D. P. Landau, and M. Bachmann, Phys. Rev. Lett. **110**, 028103 (2013).
- [16] M. Marenz and W. Janke, Phys. Rev. Lett. **116**, 128301 (2016).
- [17] T. Skrbic, T. X. Hoang, and A. Giacometti, J. Chem. Phys. **145**, 084904 (2016).
- [18] J. Wu, C. Cheng, G. Liu, P. Zhang, and T. Chen, J. Chem. Phys. **148**, 184901 (2018).
- [19] J. Wu, Y. Huang, H. Yin, and T. Chen, J. Chem. Phys. **149**, 234903 (2018).
- [20] S. Majumder, M. Marenz, S. Paul, and W. Janke, Macromolecules **54**, 5321 (2021).
- [21] C. C. Walker, T. L. Fobe, and M. R. Shirts, Macromolecules **55**, 8419 (2022).
- [22] C. N. Yang, Phys. Rev. **85**, 808 (1952).
- [23] L. Onsager, Il Nuovo Cimento (1943-1954) **6**, 279 (1949).
- [24] J. D. Van der Waals, *Over de Continuïteit van den Gas-en Vloeistooftoestand*, Vol. 1 (Sijthoff, 1873).
- [25] L. Onsager, Phys. Rev. **65**, 117 (1944).
- [26] K. Sitarachu and M. Bachmann, J. Phys.: Conf. Ser. **1483**, 012009 (2020).
- [27] K. Sitarachu, R. K. P. Zia, and M. Bachmann, J. Stat. Mech. **2020**, 073204 (2020).
- [28] K. Sitarachu and M. Bachmann, Phys. Rev. E **106**, 014134 (2022).
- [29] L. F. Trugilho and L. G. Rizzi, J. Stat. Phys. **186**, 40 (2022).
- [30] L. F. Trugilho and L. G. Rizzi, Europhys. Lett. **137**, 57001 (2022).
- [31] G. Bel-Hadj-Aissa, M. Gori, V. Penna, G. Pettini, and R. Franzosi, Entropy **22**, 380 (2020).
- [32] M. Gori, R. Franzosi, G. Pettini, and M. Pettini, J. Phys. A: Math. Theor. **55**, 375002 (2022).

- [33] G. Pettini, M. Gori, R. Franzosi, C. Clementi, and M. Pettini, *Physica A* **516**, 376 (2019).
- [34] L. Di Cairano, R. Capelli, G. Bel-Hadj-Aissa, and M. Pettini, *Phys. Rev. E* **106**, 054134 (2022).
- [35] G. Bel-Hadj-Aissa, *Phys. Lett. A* **384**, 126449 (2020).
- [36] A. Chaudhuri, C. Sadek, D. Kakde, H. Wang, W. Hu, H. Jiang, S. Kong, Y. Liao, and S. Peredriy, *Pattern Recognit.* **111**, 107662 (2021).
- [37] L. G. Ferreira, R. N. Dos Santos, G. Oliva, and A. D. Andricopulo, *Molecules* **20**, 13384 (2015).
- [38] P. Gao, J. Nicolas, and T. Ha-Duong, *J. Am. Chem. Soc.* **143**, 17412 (2021).
- [39] T. Schmidt, A. Bergner, and T. Schwede, *Drug Discov. Today* **19**, 890 (2014).
- [40] J. Smiatek, A. Jung, and E. Bluhmki, *Trends Biotechnol.* **38**, 1141 (2020).
- [41] S. Kmiecik, D. Gront, M. Kolinski, L. Wieteska, A. E. Dawid, and A. Kolinski, *Chem. Rev.* **116**, 7898 (2016).
- [42] N. Singh and W. Li, *Int. J. Mol. Sci.* **20**, 3774 (2019).
- [43] M. Bachmann, *Thermodynamics and Statistical Mechanics of Macromolecular Systems* (Cambridge University Press, Apr. 24, 2014), 359 pp.
- [44] S. K. Burley, C. Bhikadiya, C. Bi, S. Bittrich, L. Chen, G. V. Crichlow, C. H. Christie, K. Dalenberg, L. Di Costanzo, J. M. Duarte, S. Dutta, Z. Feng, S. Ganesan, D. S. Goodsell, S. Ghosh, R. K. Green, V. Guranović, D. Guzenko, B. P. Hudson, C. L. Lawson, Y. Liang, R. Lowe, H. Namkoong, E. Peisach, I. Persikova, C. Randle, A. Rose, Y. Rose, A. Sali, J. Segura, M. Sekharan, C. Shao, Y.-P. Tao, M. Voigt, J. D. Westbrook, J. Y. Young, C. Zardecki, and M. Zhuravleva, *Nucleic Acids Res.* **49**, D437–D451 (2021).
- [45] J. P. Abrahams, A. G. W. Leslie, R. Lutter, and J. E. Walker, *Nature* **370**, 621 (1994).
- [46] *The Nobel Prize in Chemistry 1997*, NobelPrize.org.

- [47] C. Yuan, H. Chen, X. W. Lou, and L. A. Archer, *Phys. Rev. Lett.* **100**, 018102 (2008).
- [48] S. Li, G. Erdemci-Tandogan, P. van der Schoot, and R. Zandi, *J. Phys. Condens.* **30**, 044002 (2017).
- [49] U. Bastolla and P. Grassberger, *J. Stat. Phys.* **89**, 1061 (1997).
- [50] A. C. Farris, G. Shi, T. Wüst, and D. P. Landau, *J. Chem. Phys.* **149**, 125101 (2018).
- [51] J.-Z. Zhang, X.-Y. Peng, S. Liu, B.-P. Jiang, S.-C. Ji, and X.-C. Shen, *Polymers* **11**, 295 (2019).
- [52] J. Zierenberg and W. Janke, *Europhys. Lett.* **109**, 28002 (2015).
- [53] J. Midya, S. A. Egorov, K. Binder, and A. Nikoubashman, *J. Chem. Phys.* **151**, 034902 (2019).
- [54] S. Ranganathan, S. K. Maji, and R. Padinhateeri, *J. Am. Chem. Soc.* **138**, 13911 (2016).
- [55] J. Zierenberg, M. Marenz, and W. Janke, *Polymers* **8**, 333 (2016).
- [56] K. S. Austin, J. Zierenberg, and W. Janke, *Macromolecules* **50**, 4054 (2017).
- [57] A. Milchev and K. Binder, *Phys. Rev. Lett.* **123**, 128003 (2019).
- [58] M. Möddel, W. Janke, and M. Bachmann, *Phys. Rev. Lett.* **112**, 148303 (2014).
- [59] T. Sintes, K. Sumithra, and E. Straube, *Macromolecules* **34**, 1352 (2001).
- [60] J. E. Lennard-Jones, *Proc. Phys. Soc.* **43**, 461 (1931).
- [61] R. B. Bird, R. C. Armstrong, and O. Hassager, (1987).
- [62] K. Kremer and G. S. Grest, *J. Chem. Phys.* **92**, 5057 (1990).
- [63] A. Milchev, A. Bhattacharya, and K. Binder, *Macromolecules* **34**, 1881 (2001).
- [64] K. Qi and M. Bachmann, *J. Chem. Phys.* **141**, 074101 (2014).
- [65] M. J. Williams and M. Bachmann, *Phys. Rev. Lett.* **115**, 048301 (2015).
- [66] M. J. Williams and M. Bachmann, *Phys. Rev. E* **93**, 062501 (2016).

- [67] M. Williams and M. Bachmann, *Polymers* **8**, 245 (2016).
- [68] M. J. Williams and M. Bachmann, *J. Chem. Phys.* **147**, 024902 (2017).
- [69] K. Qi, B. Liewehr, T. Koci, B. Pattanasiri, M. J. Williams, and M. Bachmann, *J. Chem. Phys.* **150**, 054904 (2019).
- [70] S. Schnabel, M. Bachmann, and W. Janke, *J. Chem. Phys.* **131**, 124904 (2009).
- [71] S. Schnabel, T. Vogel, M. Bachmann, and W. Janke, *Chem. Phys. Lett.* **476**, 201 (2009).
- [72] S. Schnabel, D. T. Seaton, D. P. Landau, and M. Bachmann, *Phys. Rev. E* **84**, 011127 (2011).
- [73] J. Gross, T. Neuhaus, T. Vogel, and M. Bachmann, *J. Chem. Phys.* **138**, 074905 (2013).
- [74] T. Koci and M. Bachmann, *Phys. Rev. E* **92**, 042142 (2015).
- [75] J. C. S. Rocha, S. Schnabel, D. P. Landau, and M. Bachmann, *Phys. Rev. E* **90**, 022601 (2014).
- [76] R. Schiemann, M. Bachmann, and W. Janke, *Comput. Phys. Commun.* **166**, 8 (2005).
- [77] R. Schiemann, M. Bachmann, and W. Janke, *J. Chem. Phys.* **122**, 114705 (2005).
- [78] J. H. Lee, S.-Y. Kim, and J. Lee, *AIP Adv.* **5**, 127211 (2015).
- [79] Y.-H. Hsieh, C.-N. Chen, and C.-K. Hu, *Comput. Phys. Commun.* **209**, 27 (2016).
- [80] I. Jensen, *J. Phys. A: Math. Gen.* **37**, 5503 (2004).
- [81] M. E. Newman and G. T. Barkema, *Monte carlo methods in statistical physics* (Clarendon Press, 1999).
- [82] K. S. Austin, M. Marenz, and W. Janke, *Comput. Phys. Commun.* **224**, 222 (2018).
- [83] S. Schnabel, W. Janke, and M. Bachmann, *J. Comput. Phys.* **230**, 4454 (2011).
- [84] M. Bachmann, H. Arkin, and W. Janke, *Phys. Rev. E* **71**, 031906 (2005).
- [85] V. G. Mavrantzas, T. D. Boone, E. Zervopoulou, and D. N. Theodorou, *Macromolecules* **32**, 5072 (1999).

- [86] L. D. Peristeras, I. G. Economou, and D. N. Theodorou, *Macromolecules* **38**, 386 (2005).
- [87] J. Ramos, L. D. Peristeras, and D. N. Theodorou, *Macromolecules* **40**, 9640 (2007).
- [88] V. G. Mavrantzas, *Front. Phys.* **9** (2021).
- [89] N. Metropolis, A. W. Rosenbluth, M. N. Rosenbluth, A. H. Teller, and E. Teller, *J. Chem. Phys.* **21**, 1087 (1953).
- [90] F. James, *Comput. Phys. Commun.* **60**, 329 (1990).
- [91] A. Compagner, *J. Stat. Phys.* **63**, 883 (1991).
- [92] F. Schmid and N. B. Wilding, *Int. J. Mod. Phys. E* **6**, 781 (1996).
- [93] A. Heuer, B. Dünweg, and A. M. Ferrenberg, *Comput. Phys. Commun.* **103**, 1 (1997).
- [94] G. Marsaglia, A. Zaman, and W. W. Tsang, *JStat. Probab. Lett* **9**, 35 (1990).
- [95] G. Marsaglia and W. W. Tsang, *JStat. Probab. Lett* **66**, 183 (2004).
- [96] R. H. Swendsen and J.-S. Wang, *Phys. Rev. Lett.* **57**, 2607 (1986).
- [97] A. M. Ferrenberg and R. H. Swendsen, *Phys. Rev. Lett.* **61**, 2635 (1988).
- [98] C. J. Geyer, *American Statistical Association, New York* **156** (1991).
- [99] K. Hukushima and K. Nemoto, *J. Phys. Soc. Jpn.* **65**, 1604 (1996).
- [100] K. Hukushima, H. Takayama, and. NEMOTO, *coherent*, 133 (1996).
- [101] D. J. Earl and M. W. Deem, *Phys. Chem. Chem. Phys.* **7**, 3910 (2005).
- [102] C. E. Fiore, *Phys. Rev. E* **78**, 041109 (2008).
- [103] D. A. Kofke, *J. Chem. Phys.* **121**, 1167 (2004).
- [104] J. Machta, *Phys. Rev. E* **80**, 056706 (2009).
- [105] J. Machta and R. S. Ellis, *J Stat Phys* **144**, 541 (2011).
- [106] C. Predescu, M. Predescu, and C. V. Ciobanu, *J. Phys. Chem. B* **109**, 4189 (2005).

- [107] E. Bittner, A. Nußbaumer, and W. Janke, Phys. Rev. Lett. **101**, 130603 (2008).
- [108] F. Hamze, N. Dickson, and K. Karimi, Int. J. Mod. Phys. C **21**, 603 (2010).
- [109] K. Hukushima, Phys. Rev. E **60**, 3606 (1999).
- [110] H. G. Katzgraber, S. Trebst, D. A. Huse, and M. Troyer, J. Stat. Mech. **2006**, P03018–P03018 (2006).
- [111] C. Predescu, M. Predescu, and C. V. Ciobanu, J. Chem. Phys. **120**, 4119 (2004).
- [112] N. Rathore, M. Chopra, and J. J. de Pablo, J. Chem. Phys. **122**, 024111 (2005).
- [113] I. Rozada, M. Aramon, J. Machta, and H. G. Katzgraber, Phys. Rev. E **100**, 043311 (2019).
- [114] F. Wang and D. P. Landau, Phys. Rev. Lett. **86**, 2050 (2001).
- [115] S. Schnabel and W. Janke, Comput. Phys. Commun. **267**, 108071 (2021).
- [116] S. Kirkpatrick, C. D. Gelatt, and M. P. Vecchi, Science **220**, 671 (1983).
- [117] U. H. E. Hansmann and L. T. Wille, Phys. Rev. Lett. **88**, 068105 (2002).
- [118] S. Kumar, J. M. Rosenberg, D. Bouzida, R. H. Swendsen, and P. A. Kollman, J. Comput. Chem. **13**, 1011 (1992).
- [119] P. Bézier, Automatisme **13**, 189 (1968).
- [120] W. J. Gordon and R. F. Riesenfeld, J. ACM **21**, 293 (1974).
- [121] B. Song, G. Tian, and F. Zhou, **7**, 2943 (2010).
- [122] G. M. Phillips, BIT Numerical Mathematics **37**, 232 (1997).
- [123] P. G. Todorov, Pacific Journal of Mathematics **92**, 217 (1981).

- [124] P. Virtanen, R. Gommers, T. E. Oliphant, M. Haberland, T. Reddy, D. Cournapeau, E. Burovski, P. Peterson, W. Weckesser, J. Bright, S. J. van der Walt, M. Brett, J. Wilson, K. J. Millman, N. Mayorov, A. R. J. Nelson, E. Jones, R. Kern, E. Larson, C. J. Carey, Í. Polat, Y. Feng, E. W. Moore, J. VanderPlas, D. Laxalde, J. Perktold, R. Cimrman, I. Henriksen, E. A. Quintero, C. R. Harris, A. M. Archibald, A. H. Ribeiro, F. Pedregosa, P. van Mulbregt, and SciPy 1.0 Contributors, *SciPy 1.0: Fundamental Algorithms for Scientific Computing in Python*, (2020)
- [125] A. Savitzky and M. J. Golay, *Anal. Chem.* **36**, 1627 (1964).
- [126] D. Aierken and M. Bachmann, *Polymers* **12**, 3013 (2020).
- [127] D. Aierken and M. Bachmann, *Phys. Rev. E* **107**, L032501 (2023).
- [128] D. Aierken and M. Bachmann, “Impact of bending stiffness on ground-state conformations for semiexible polymers (submitted)”.